A STUDY OF
THE METAL - INSULATOR - N - P SEMICONDUCTOR
GRATING SOLAR CELLS

WONG Yuen-Fai, Dick (黃源輝)

A thesis submitted in partial fulfilment of
the requirements for the degree of

MASTER OF PHILOSOPHY

in the Department of Electronics,
The Chinese University of Hong Kong,
May, 1985.

ACKNOWLEDGEMENTS

I would like to express my sincere thanks to the following persons:

1. Prof. Y.W. Lam for providing this opportunity of research, his supervision and valuable suggestions in the course of the work;

2. Mr.C.K. Pun, Mr. W.C. Chu, Mrs. L.Y.P. Yum, Mr. K.C. Fong, Mr. M.C. Poon and Mr. F.K. So, staff of the Department of Electronics, for their technical support;

3. Mr. C.S. Hoi and Mr. Y.C. Leung for helpful discussions; and

4. Ms. Y.L. Li for continuous encouragement.

I am indebted to the Department of Physics for providing the stroboscope and radiometer used in this study and the Solarex Corp. for calibrating the reference solar cell.

I am also grateful to the Croucher Foundation for its financial support.

TABLE OF CONTENTS

ABSTRACT

Experimental studies of the MINP structure by both ion implantation and diffusion are conducted systematically. Cells are fabricated by a simple, alignment free process with single layer SiO antireflection coating but without back surface field.

The performance of the MINP cells depends on both the surface doping effect and the temperature treatment effect. Isochronal and isothermal pre-processing heat treatment on MIS solar cells are performed to study the performance dependence of the temperature effect only isolated from the doping effect for the first time. The performance degradation is related to the lifetime degradation and the increases in the saturation current and the ideality factor. The temperature dependent increases in the saturation current and the ideality factor are attributed to effects such as recombination in the space charge region and surface states.

In the case of ion implanted MINP cells, implant parameters (dose and energy) and annealing conditions are investigated. The performance dependence of the ion implanted MINP cells on such parameters has not been found in the literature. The optimum annealing temperature and implant dose are found to be 800^{o}C and 10^{13} cm^{-2} respectively. The dose is two order of magnitude lower than the conventional ion implanted cells which implies that ion implantation may be cost competitive to diffusion if the MINP structure is used.

Decrease in the carrier lifetime and increase in the saturation current and the ideality factor are dominated by the doping level even though there is also temperature dependence. The increase in the ideality factor with the doping level is in agreement with the calculation. Excess current is shown to result from the recombination current through traps in the depletion region at low dose level. While at high dose, a field emission component is suggested.

In the case of diffused MINP cells, two independent parameters - temperature and time are studied. 800°C 10 min single step diffusion is found to be the optimum diffusion condition.

Effects of the grid spacing on the MINP cells are demonstrated for the first time. It is found that the margin of the efficiency advantage of the MINP cells over the MIS cells increases with the grid spacing.

Cell performance of two substrate resistivities are studied. The efficiency advantage of the MINP cells over the MIS cells of the 0.5 ohm-cm substrate is larger than the 1.5 ohm-cm substrate.

The performance of the MINP cells is substantially higher than the MIS cells. The total area efficiency of the highest ion implanted and diffused MINP cells are 15 % and 15.88 % respectively measured at AM1.5.

Diffusion is found to out perform ion implantation in the fabrication of MINP cells.

LIST OF SYMBOLS

a	thickness of surface doped layer
A^*	modified Richardson constant
D_n, D_p	diffusion coefficients of electrons, holes
$E_g, \Delta E_g$	energy band gap, energy band gap narrowing
E_i	intrinsic energy level
E_c, E_v	energy of conduction, valence band edges
E_a	activation energy
E_{fn}, E_{fp}	quasi-Fermi level for electron, hole
F_o	incident photon flux
FF	fill factor
I_{sc}	short circuit current
j_c, j_v	electron, hole current into interface states
j_t	electron tunneling current from interface states into metal
J_{so}	recombination current density due to surface states
J_n, J_p	electron, hole current density
J_{mp}	current density under maximum power condition
k	Boltzmann's constant
L_n, L_p	minority carrier (electron, hole) diffusion length
m^*_{te}, m^*_{th}	effective mass of electrons, holes in semiconductor with monentum transverse to the barrier
n	ideality factor
n_i	intrinsic carrier concentration
n_s	electron concentration at the surface
N_D, N_A	donor, acceptor concentrations
N_c, N_v	effective density of states in conduction , valence

	bands
N_s	interface state density
N_{df}	defect density
n,p	free carrier concentration
q	electron charge
Q_n	inversion layer charge density
Q_{ox}	oxide charge density
Q_D	total doped dosage
Q_M	charge density reside on metal
Q_{SC}, Q_{SS}	charge density in space charge region, due to surface states
R_s	sheet resistivity
T	temperature
T_f	prevalent temperature of defect formation
U	recombination rate
v_{th}	thermal velocity
v_{TP}	transmission velocity
v_D	effective diffusion velocity
V	applied voltage
V_D	diffusion potential
V_{bi}	built in potential
V_s, V_i	change in potential across the semiconductor, interfacial layer
V_{oc}	open circuit voltage
V_{mp}	voltage under maximum power condition
W	depletion width
W_c	width of contact lines

σ_T	capture cross section of surface states
σ_n, σ_p	capture cross section of electrons, holes
ϵ_s, ϵ_i	permittivity of semiconductor, insulator
δ, d	interfacial layer thickness
λ	wavelength of the incident light
ϕ_n, ϕ_p	barrier height for n, p type devices
$\Delta\phi_h$	barrier height enhancement
ϕ_s	surface potential
ϕ_m	metal work function
η	solar cell efficiency
τ_n, τ_p	minority carrier (electron, hole) lifetime
μ_n, μ_p	mobility for electrons, holes
χ_e, χ_h	potential barrier of oxide to electrons, holes tunneling into metal

1. INTRODUCTION

A solar cell consists of a potential barrier within a semiconductor material that is capable of separating the electron hole pairs generated by the incident light. This potential barrier can be formed by a p-n junction, a Schottky barrier, a metal-insulator-semiconductor (MIS) barrier, etc..

For a p-n junction solar cell, a heavily doped (by diffusion or ion implantation) surface layer is required to keep the series resistance low. Unfortunately, this heavily doped surface layer causes poor minority carrier lifetime and bandgap shrinkage. The effects are exacerbated owing to maximum generation at the surface region. Much work is devoted to this area [1-3].

By depositing a metal of proper work function on the surface of the semiconductor, a Schottky barrier is formed. This is a simple, high yield, and fast throughput process. In addition, only low temperature treatment is required. Low temperature process is advantageous because

1. it is cost saving because of low energy consumption,
2. the minority carrier lifetime of the starting material is preserved which is essential for high efficiency, and
3. it prevents interdiffusion of impurities on the grain boundary resulting in shorting or enhanced leakage current in case of polycrystalline substrate.

Since there is no heavily doped surface layer, the short

wavelength response is also enhanced.

However, the efficiency of the metal-semicondutor (MS) solar cell is low due to a large thermionic emission majority dark current.

Introducing a thin interfacial layer between the metal and the semiconductor results in a MIS structure which preserves the advantages but eliminates the disadvantage of the MS solar cell.

The thermionic emission majority current is suppressed by the interfacial layer due to

1. incresed effective barrier height,
2. decreased probability of majority carrier tunneling,
3. encouraged interface states with a large capture cross-section for majority carriers, and
4. reduced number of majority carriers at the semiconductor surface [4,5].

Depending on the dominant component of the dark current, the MIS solar cell is classified as majority device or minority device [6,7]. Both majority and minority MIS devices have been intensively studied. Reviews in this topic can be found in many publications such as [4,8].

In principle, the MIS structure is covered by a thin continuous metal over the cell surface. Metal thickness of less than 100 A is required to insure light transmission. But a thin metal film results in a high sheet resistance. Compromise between good conductivity and good light transmisssion is needed.

An alternative to continuous thin metal method is to employ

a grating structure. An inversion layer is induced by charges inside the anti-reflection (AR) coating between gratings. High efficiency minority MIS grating cells have been reported [9,10].

However, the MIS solar cell degrades rapidly under stress conditions such as thermal stress, optical stress, electrical stress, and also under radiation damage [11]. The thin SiO_2 interfacial layer is reduced to Al_2O_3 in the Al-SiO_2-Si system [12]. Electrostatic effects such as opposite charges (as in SiO-Si interface) on the SiO AR coating surface weaken the inversion layer and force one to use a fine grating structure [13].

Green et al. combined the advantages of the MIS solar cell and the p-n junction solar cell and reported open circuit voltage as high as 694 mV at AM0 on a MINP structure [14,15].

Early workers [16,17] have also found, by the use of low dose ion implantation, an increase in efficiency of the Schottky barrier (MIS) solar cell.

A major reduction in effective recombination velocity under the top contact and reduced recombination in the emitter region make the MINP structure superior to the p-n junction cells. On the other hand, improved passivation of surface states by optimized electron concentration along the surface results in a voltage advantage over minority MIS solar cells.

The MINP solar cell possesses a reduced temperature sensitivity [18] and superior tolerance to electron radiation [19].

In the work to be reported in this thesis, the effects of different fabrication techniques and different fabrication conditions on the MINP solar cells are systematically studied. Comparison between the MINP and the MIS solar cells are made. The theoretical bases of the MINP solar cells are developed in chapter 2. Process temperature plays an important role in high efficiency solar cells. But a high temperature step (either in the diffusion of the n layer or in the annealing of the ion implanted cells) is unavoidable. Results of pre-processing high temperature heat treatment on the MIS solar cells are presented in chapter 3 to anticipate the high temperature process effects in the MINP process. Results on the ion implanted and diffused MINP solar cells are presented in chapter 4 and chapter 5. Conclusions are given in chapter 6.

References

[1] M.A.Shibib, F.A. Lindholm and F. Therez, " Heavily doped transparent emitter regions in junction solar cells, diodes, and transistors," IEEE Trans. Electron Dev., Vol. 26, p.959, 1979.

[2] F.A. Lindholm et al., "A methodology for experimentally based determination of gap shrinkage and effective lifetimes in the emitter and base of p-n junction solar cells and other p-n junction devices," IEEE Trans. Electron Dev., Vol. 24, p.402, 1977.

[3] J.G. Fossum, F.A. Lindholm and M.A. Shibib, "The importance of surface recombination and energy bandgap narrowing in p-n junction silicon solar cells," IEEE Trans. Electron Dev., Vol. 26, p.1294, 1979.

[4] D.L. Pulfrey, "MIS solar cells : a review," IEEE Trans. Electron Dev., Vol. 25, p.1308, 1978.

[5] S.J. Fonash, "Outline and comparison of the possible effects present in a metal-thin-film-insulator-semiconductor solar cell," J. Appl. Phys., Vol. 47, p.3597, 1976.

[6] M.A. Green, F.D. King and J. Shewchun, "Minority carrier MIS tunnel diodes and their application to electron- and photo-voltaic energy conversion - 1. theory," Solid State Ele., Vol. 17, p.551, 1974.

M.A. Green, F.D. King and J. Shewchun, "Minority carrier MIS tunnel diodes and their application to electro- and photo-voltaic energy conversion - 2. experiment," Solid State Ele., Vol. 17, p.563, 1974.

[7] K.K. Ng and H.C. Card, " A comparison of majority and

minority silicon MIS solar cells," IEEE Trans. Electron Dev., Vol. 27, p.716, 1980.

[8] W.G. Townsend, "Schottky barrier solar cells," Photovoltaic and Photoelectro-chemical Solar Energy Conversion, p.67.

[9] R.B. Godgrey and M.A. Green, "High efficiency silicon minMIS solar cells - design and experimental results," IEEE Trans. Electron Dev., Vol. 27, p.737, 1980.

[10] M.A. Green, R.B. Godfrey, M.R. Willison and A.W. Blakers, "High efficiency (>18%, active area, AM1) silicon minMIS solar cells," 14th IEEE Photov. Spec. Conf., p.684, 1980.

[11] G. Cheek and R. Mertens, "MIS silicon solar cells : potential advantages," 15th IEEE Photov. Spec. Conf., p.660, 1981.

[12] J.K. Kleta and D.L. Pulfrey, "On the stability of MIS solar cells," IEEE Ele. Dev. Lett., Vol. 1, p.107, 1980.

[13] Y.W. Lam, M.A. Green and L.W. Davis, "Electrostatic effects in inversion layer MIS solar cells," Appl. Phys. Lett., p.1087, 1980.

[14] M.A. Green et al., "The MINP solar cell - a new high voltage, high efficiency silicon solar cell," 15th IEEE Photov. Spec. Conf., p.1405, 1981.

[15] M.A. Green et al., "Towards a 700 mV silicon solar cell," 16th IEEE Photov. Spec. Conf., p.1219, 1982.

[16] J.P. Ponpon and P. Siffert, "Silicon solar cells made by ion implantation and glow discharge," 11th IEEE Photov. Spec. Conf., p.342, 1975.

[17] Y.P. Pai, H.C. Lin and M.C. Peckerar, "Current transport in

ion implanted solar cells," IEDM Tech. Digest, p.51, 1977.

[18] M.A. Green and K. Emery, " Silicon solar cells with reduced temperature sensitivity," Ele. Lett., Vol. 18, p.97, 1982.

[19] M. Thayer, W.A. Anderson and B.B. Rao, "Reliability of MINP compared to MIS, SIS, and N/P silicon solar cells under 1.0 MeV electron and environmental effects," IEEE Trans. Electron Dev., Vol. 31, p.619, 1984.

2. THEORY

The structures employed in this study are shown in Fig. 2.1. The MINP grating structure (Fig. 2.1b) is similar to the MIS grating structure (Fig. 2.1a) except there is a surface doped layer.

Region 1 (metal-insulator-n-p semiconductor) and region 2 (antireflection coating-insulator-n-p semiconductor) are considered separately.

In region 1, the potential barrier enhancement and the ideality factor are examined in section 2.1.1 - 2.1.3 while the dark current-voltage characteristic is considered in section 2.1.4.

Surface recombination loss and series resistance loss in region 2 are discussed in section 2.2.

A simple distributed diodes circuit is employed to model the cell (section 2.3).

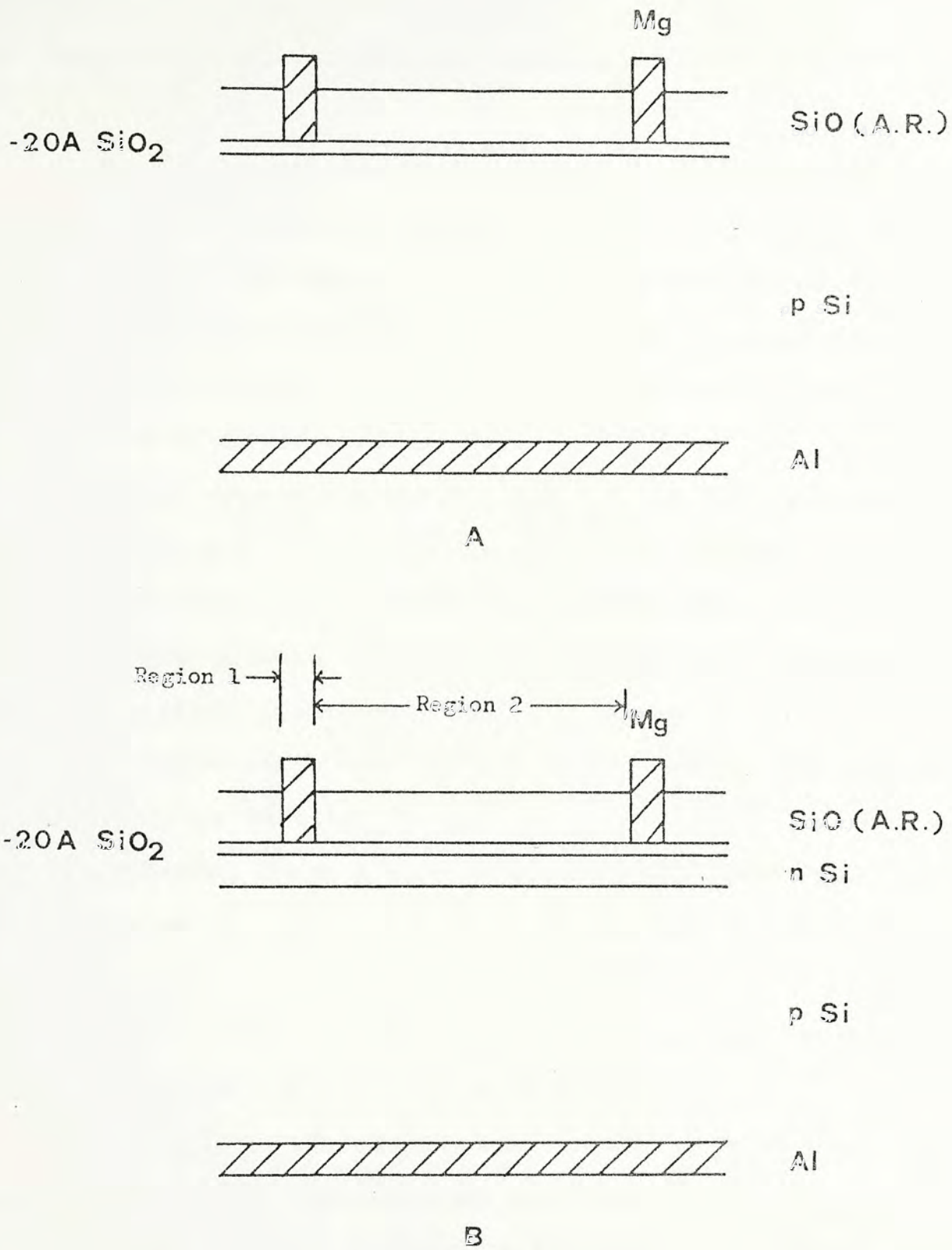

Fig. 2.1 A - schematic of a MIS grating solar cell
B - schematic of a MINP grating solar cell

2.1 Metal-Insulator-n-p (MINP) Region

The Schottky barrier height can be controlled by a thin heavily doped surface layer between the metal and the semiconductor. A layer of like doping and opposite doping decreases and increases the barrier height respectively [1-3]. The thin heavily doped layer can be formed by either ion implantation [1-3] or alloying [4,5].

Depletion approximation was employed in the calculation for uniformly [1,4,6-8] and nonuniformly [9,10] doping profiles. Wu [11-13] included also the interfacial insulator and the image force lowering effects in the barrier height calculation. If the enhanced barrier height becomes comparable to the bandgap, an inversion layer is formed [14]. In that case, the depletion approximation is invalid.

Accordingly, there are four cases to be considered.

1. Depletion approximation holds in both the surface layer and the substrate.
2. Depletion approximation holds only in the heavily doped surface layer but not in the substrate.
3. Free carrier concentration is significant in both regions such that depletion approximation does not apply.
4. The surface layer is so thick that a neutral region occurs. It may then be treated as a MIS barrier in cascade with a p-n junction.

Case 1,2 and 4 with respect to a p substrate are considered in this chapter. While full analytical expressions for case 3

are not feasible, numerical analysis is being carried out by Hoi [14].

2.1.1 Case 1 - n^+ and p regions depleted

Card [4] has analyzed the situation of a p^+ layer on n substrate with the assumption that both regions are depleted. Hoi [16] has followed Card's approach and derived the barrier height enhancement for a n^+ layer on p substrate.

Fig. 2.2 illustrates the corresponding charge and electric field distribution.

The barrier height enhancement [16] is given by

$$\Delta\Phi_h = \frac{qN_A a^2}{2\epsilon_s} - \frac{qN_A a}{\epsilon_s} W_o' \qquad (2.1)$$

where N_D = the donor concentration of the n^+ layer,

a = the thickness of the n^+ layer,

N_A = the acceptor concentration of the substrate,

ϵ_s = the permittivity of the semiconductor,

q = the charge and

W_o' = the depletion width under zero bias

$$W_o' = W_o\left(1 + N_D a^2/N_A W_o^2\right)^{1/2} \qquad (2.2)$$

where W_o = the depletion width without the n^+ surface layer.

The ideality factor is given by

$$n = \left(1 - \left(qN_A a^2/2\epsilon_s(V_D+V)\right)^{1/2}\right)^{-1} \qquad (2.3)$$

where V_D = the diffusion potential, and

V = the applied voltage which is negative in case of

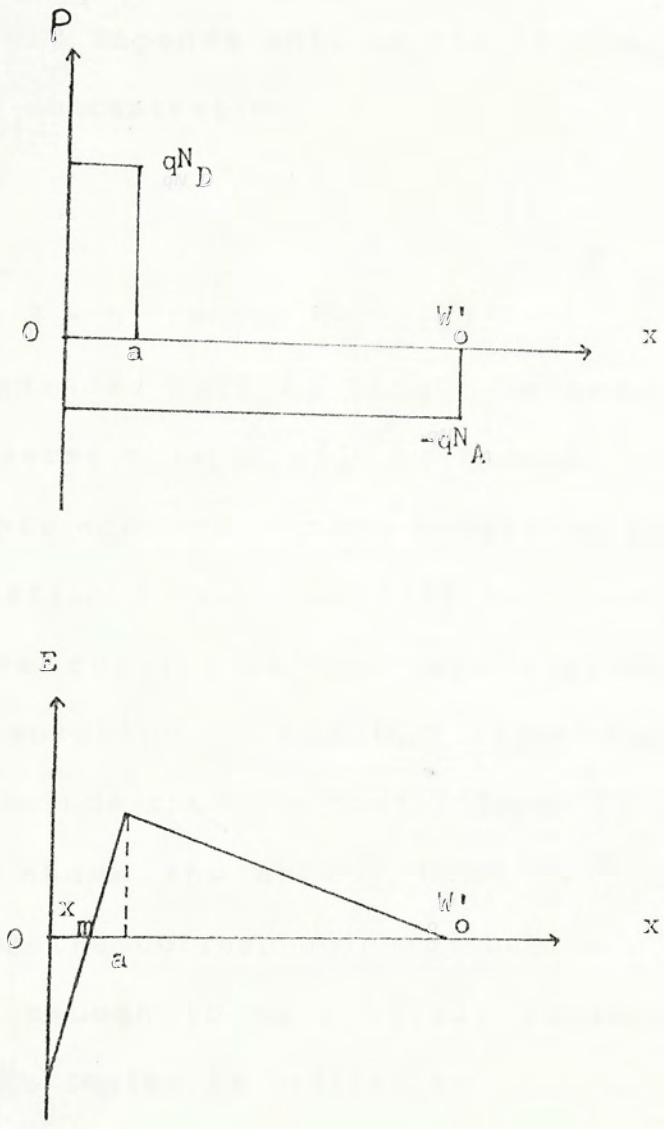

Fig. 2.2 Charge density and electric field distribution when both n^+ and p layers are depleted.

forward bias.

From the above expressions, we see that the barrier height enhancement increases with the surface doping concentration while there is always an increase in the depletion width. The ideality factor, however, depends only on the thickness of the n^+ layer but not on its concentration.

2.1.2 Case 2 - n^+ region depleted

If the enhanced barrier height becomes comparable to the bandgap, an inversion layer will be formed. An accurate analysis should take into account this inversion layer in addition to the usual depletion layer. Roy [14] has treated a MPN structure with the above consideration. His approach is followed in deriving the solution to the MNP structure in this section. Extension to include the interfacial layer is also given.

Fig. 2.3 shows the energy band diagram and the charge distribution of the corresponding situation. Assume that the n^+ layer is thin enough to be entirely depleted. The Poisson's equation in this region is written as

$$\frac{d^2\Phi}{dx^2} = -\frac{q}{\epsilon_s}(N_D - N_A) \qquad \text{for } -t \leq x \leq 0 \qquad (2.4)$$

Integrating (2.4) with boundary condition that the electric field is zero at $x = -x_m$ where the potential energy minimum is located, the electric field is given by

$$E = (q/\epsilon_s)(N_D - N_A)(x + x_m) \qquad (2.5)$$

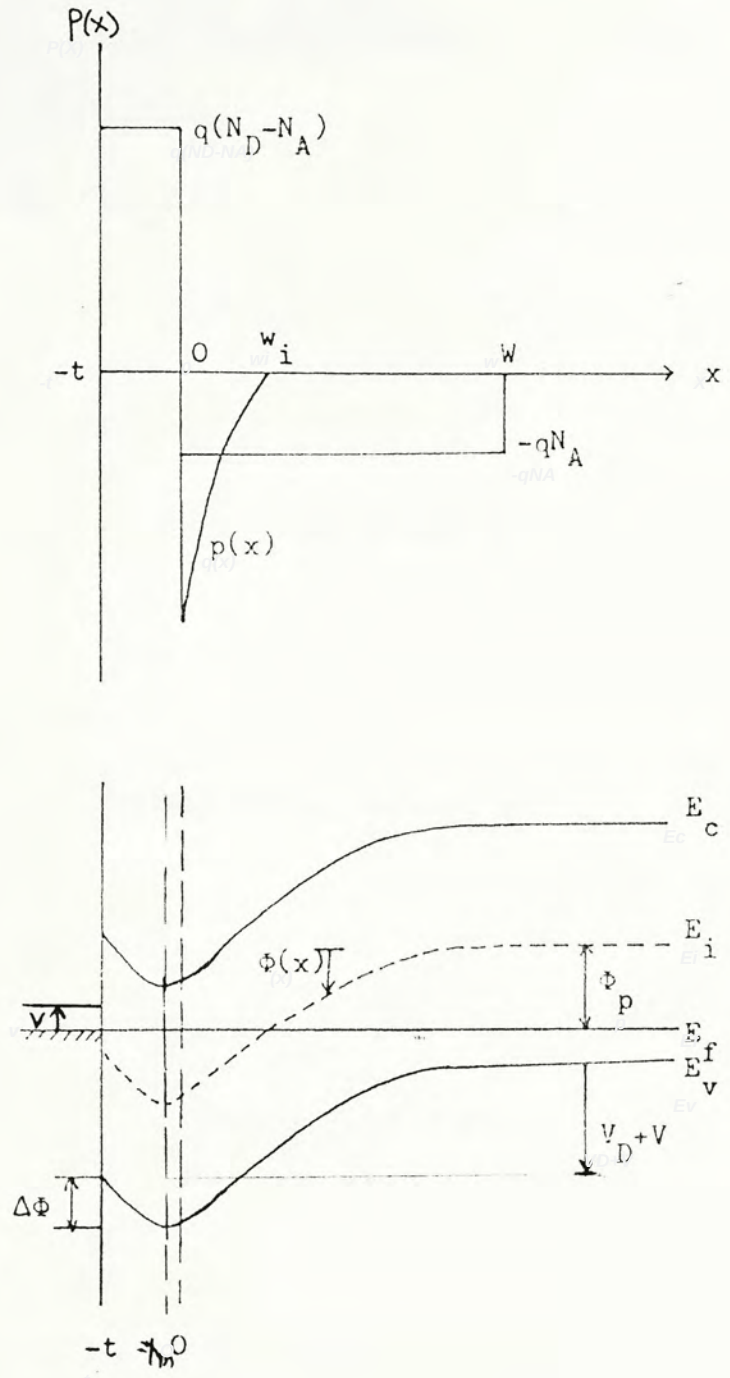

Fig. 2.3 Schematic of charge distribution and energy band diagram considering inversion model.

Integrating (2.5) with boundary condition $\phi = V_D + V$ at $x = -t$, the potential is given by

$$\Phi = (V_D+V) - (q / 2\epsilon_s)(N_D - N_A)(x^2-t^2+2x_m(x+t)) \qquad (2.6)$$

The potential at the p-n junction ($x = 0$) readily follows as

$$\Phi(0) = (V_D+V) + \frac{q}{2\epsilon_s}(N_D-N_A)(t^2-2x_m t) \qquad (2.7)$$

Consider the space charge density in the p region which is given by

$$\begin{aligned} \rho &= q\,(p - N_A - n) \\ &\doteq -q\,(N_A + n) \end{aligned} \qquad (2.8)$$

since p is small compared to N_A and n, and

$$n(x) = \frac{n_i^2}{N_A} \exp(q\Phi/kT) \qquad (2.9)$$

The Poisson's equation in the p region is written as

$$\frac{d^2\Phi}{dx^2} = \frac{-\rho}{\epsilon_s} = \frac{q}{\epsilon_s}\left(N_A + \frac{n_i^2}{N_A} \exp(q\Phi/kT) \right) \qquad (2.10)$$

or $$\frac{d}{dx}\left(\frac{d\Phi}{dx}\right)^2 = - \frac{2\rho}{\epsilon_s}\left(\frac{d\Phi}{dx}\right) \qquad (2.11)$$

Noting that the electric field is zero in the bulk semiconductor, (2.11) can be integrated to give

$$E^2 = \frac{2q}{\epsilon_s}\left(N_A\Phi + \frac{n_i^2}{N_A}\frac{kT}{q}\left(\exp(q\Phi/kT) - 1 \right) \right) \qquad (2.12)$$

Now, $E = E(0)$, $\phi = \phi(0)$ at $x = 0$

$$E^2 = E^2(0) + \frac{2q}{\epsilon_s}\left(N_A(\Phi-\Phi(0)) + \frac{n_i^2}{N_A}\frac{kT}{q}\left(\exp(q\Phi/kT)-\exp(q\Phi(0)/kT) \right) \right) \qquad (2.13)$$

Since the electric field is continuous across $x = 0$, from (2.5) and (2.12)

$$E(0) = \frac{q}{\epsilon_s} (N_D - N_A) x_m$$

$$= \frac{2q}{\epsilon_s} (\frac{n_i^2}{N_A} \frac{kT}{q} (\exp(q\Phi(0)/kT)-1) + N_A\Phi(0))^{1/2} \qquad (2.14)$$

From (2.7) and (2.14), x_m may be found for various values of N_D and t. Hence E and Ø in the n region can readily be determined.

The space charge density on the p region required to produce the field E(0) is given by Guass' law as

$$Q_{SC} = - \epsilon_s E(0)$$

$$= - (2q\epsilon_s (\frac{n_i^2}{N_A} \frac{kT}{q} (\exp(q\Phi(0)/kT)-1) + N_A\Phi(0)))^{1/2} \qquad (2.15)$$

Note that the first term is due to mobile carriers while the second term is due to ionized acceptors.

In order to obtain analytical expression of the potential profile, (2.13) is integrated piecewise, first in the iversion layer, then in the depletion region. The solutions are matched at $x = w_i$, the boundary of the inversion layer.

Consider in the inversion region, rearrange (2.13) gives

$$E^2 = A \exp(B\Phi) + C\Phi + D \qquad (2.16)$$

where $A = \frac{2q}{\epsilon_s} \frac{n_i^2}{N_A} \frac{kT}{q}$

$B = kT/q$

$C = 2qN_A/\epsilon_s$

$D = E^2(0) - \frac{2q}{\epsilon_s} (N_A\Phi(0) + \frac{n_i^2}{N_A} \frac{kT}{q} \exp(q\Phi(0)/kT))$

Taking the positive root of (2.16) and writing $Z = (B/C)(D+C\Phi)$, we have

$$\frac{dZ}{dx} = - (BC)^{1/2}(Z)^{1/2}(1 + \exp(Z)/\beta Z)^{1/2} \qquad (2.17)$$

where $\beta = C\exp(BD/C) / AB$

It can be shown that $(1/\beta Z)\exp(Z) << 1$. Thus, (2.17) reduces to

$$\frac{dZ}{dx} = - (BC)^{1/2}(Z)^{1/2} \qquad (2.18)$$

Integrating (2.18) with boundary condition $Z = Z(0)$ at $x = 0$, we obtain the expression for potential in the inversion layer

$$Z = \tfrac{1}{4} \left(2Z(0)^{1/2} - x(BC)^{1/2} \right)^2$$

or
$$\Phi = \left(\tfrac{1}{4} \left(2Z(0)^{1/2} - x(BC)^{1/2} \right)^2 - BD/C \right) / B \qquad (2.19)$$

The width of the inversion layer, w_i is defined as where

$$\Phi(w_i) = \Phi_p \quad \text{and} \quad \Phi_p = (kT/q) \ln(N_A/n_i)$$

$$w_i = \frac{-2}{(BC)^{1/2}} \left(Z(w_i)^{1/2} - Z(0)^{1/2} \right) \qquad (2.20)$$

where $Z(w_i)$ is the Z value at $x = w_i$. It can be shown from (2.20) that w_i increases with increse of both N_D and t.

Beyond the inversion region, depletion approximation is employed so that the second term in the bracket of the right hand side of (2.12) is neglected. Then,

$$E^2 = \frac{2q}{\epsilon_s} N_A \Phi \qquad (2.21)$$

Integrating (2.21) with boundary condition $\Phi = 0$ at $x = W$, the potential distribution in the region $w_i \leq x \leq W$ is obtained as

$$\Phi = \frac{qN_A}{2\epsilon_s} (W - x)^2 \qquad (2.22)$$

At $x = w_i$, $\Phi = \Phi_p$, so that

$$(W - w_i)^2 = \frac{2\epsilon_s \Phi_p}{qN_A} \qquad (2.23)$$

(2.23) gives the depletion width in the p region.

The amount of increase in barrier height $\Delta\phi_h$ is given by the difference of potential at $x = -x_m$ and $x = -t$

$$\Delta\Phi_h = \Phi(-x_m) - \Phi(-t)$$

$$= \frac{q}{2\epsilon_s} (N_D - N_A) (t - x_m)^2 \qquad (2.24)$$

The ideality factor is given by

$$n = (1 + \frac{d\Delta\Phi_h}{d V})^{-1}$$

$$= (1 - \frac{X(t-x_m)}{(N_D-N_A)x_m + Xt}) \qquad (2.25)$$

$$\text{where } X = \frac{n_i^2}{N_A} \exp(q\Phi(0)/kT) + N_A$$

Extension to include intefacial insulator layer

If an interfacial insulator layer of thickness d exists between the metal and the semiconductor, the applied voltage V will be distributed as

$$V = V_i + V_s \qquad (2.26)$$

where V_i = the voltage drop in the insulator layer due to the applied voltage V,

V_s = the voltage drop in the semiconductor due to the applied voltage V.

All expressions darived above except for the ideality factor (2.25) are valid by simply replacing V by V_s.

The voltage drop in the insulator layer due to the applied voltage V is given by

$$V_i = \frac{-d\Delta Q_M}{\epsilon_i}$$

and $$\Delta Q_M = -(\Delta Q_{SC} + \Delta Q_{SS}) \qquad (2.27)$$

where ΔQ_M = the change in charge density residing on the metal,

ΔQ_{SC} = the change in space charge density in the semiconductor,

ΔQ_{SS} = the change in charge density due to interface states.

With the help of (2.26) and (2.27), $\phi(0)$ and x_m can be obtained from (2.9) and (2.14). Subsequently, other expressions can be calculated.

The expression for the ideality factor is more complicated in this case, as the second term in the bracket of (2.25) now differs from the previous expression by a factor of (dV_S/dV). (2.25) will apply only under the assumption that the minority Fermi level is pinned due to good communication with metal, i.e. $V_S = V$.

Fig. 2.4 shows the barrier height enhancement against surface layer doping concentration with different surface layer thickness for the metal work function and the substrate resistivity used in the experimental study. There is a critical doping concentration such that barrier height enhancement exists only when this critical value is exceeded. For any barrier height enhancement a thinner surface layer requires a higher concentration.

Fig. 2.5 shows the ideality factor against surface layer concentration with different surface layer thickness. The ideality factor rises slowly and then sharply as the

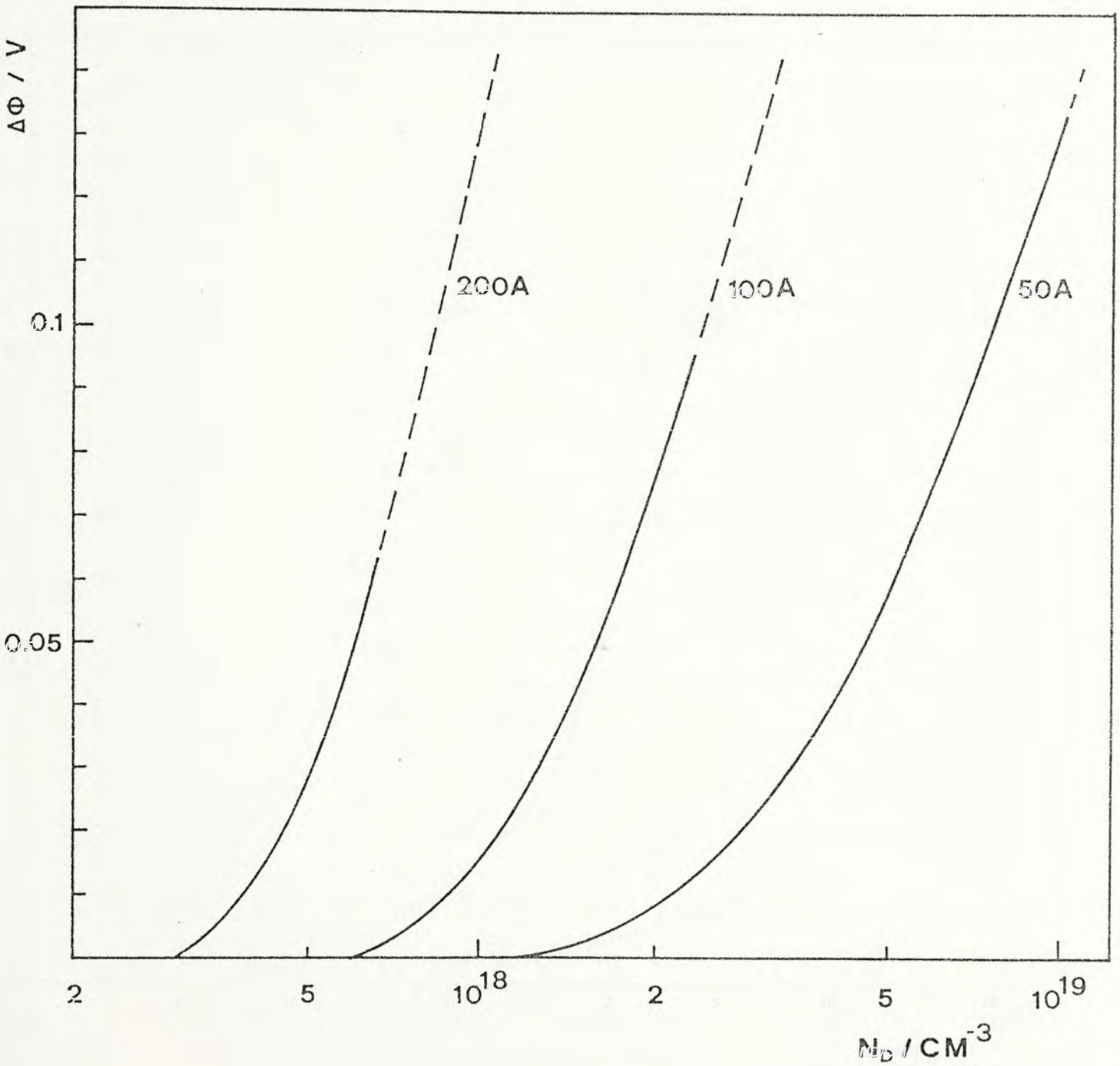

Fig. 2.4 Barrier height enhancement versus surface doping concentration with surface layer thickness as a parameter. $N_A = 3 \times 10^{16}\ cm^{-3}$, $\Delta\Phi_h = 0.9$ V and V = 0 V.

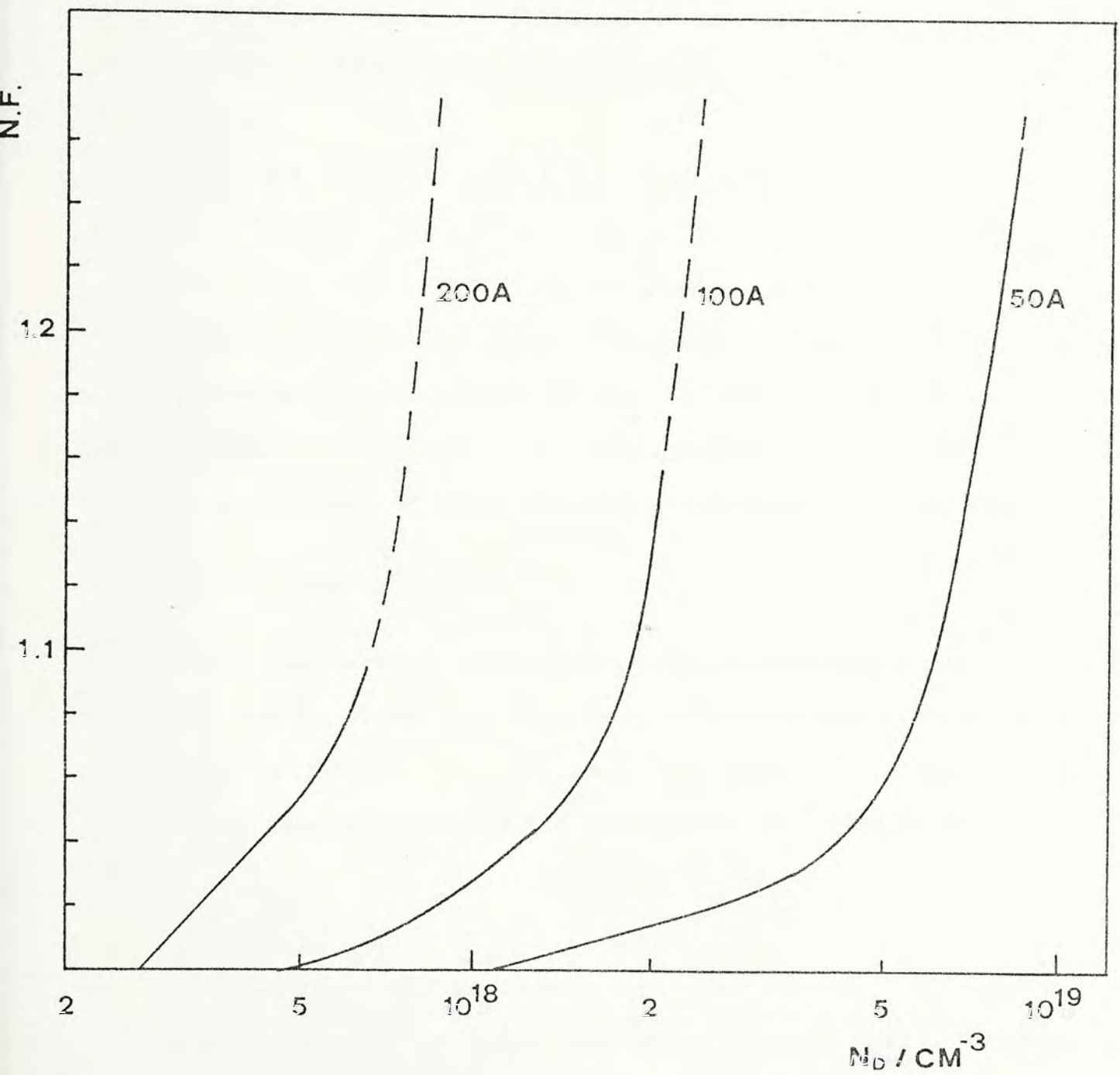

Fig. 2.5 Ideality factor versus surface doping concentration with surface layer thickness as a parameter. $N_A = 3 \times 10^{16}\ cm^{-3}$, $\Delta\Phi_h = 0.9$ V and V = 0 V.

concentration increases.

When the inversion layer is included, the ideality factor depends on both the surface doping concentration and the surface layer thickness which is different from (2.3) which depends only on the surface layer thickness (where both n^+ and p layers are depleted).

Fig. 2.4 and 2.5 will be referred in the experimental section (chapter 4 and chapter 5).

The free carrier concentration in the surface layer increases as the barrier height increases. When the free carrier concentration is comparable to the surface doping concentration, the depletion approximation in the surface layer becomes invalid. A rough estimation of this critical magnitude is given by

$$\frac{N_D}{10} = N_c \exp\left(- \frac{E_c(x_m) - E_{fp}}{kT} \right) \qquad (2.28)$$

where N_C = the density of states in the conduction band.

The region where the depletion approximation becomes invalid is shown in broken line in Fig. 2.4 and 2.5. However, full analytical expressions in this regime are not feasible.

2.1.3 Case 4 - MIS barrier + p-n junction

When the surface layer is thick enough that a neutral n region is formed, the structure can be treated as a MIS barrier in cascade with a p-n junction (Fig. 2.6). The sign and magnitude of the surface potential ϕ_S depends on the metal work function used.

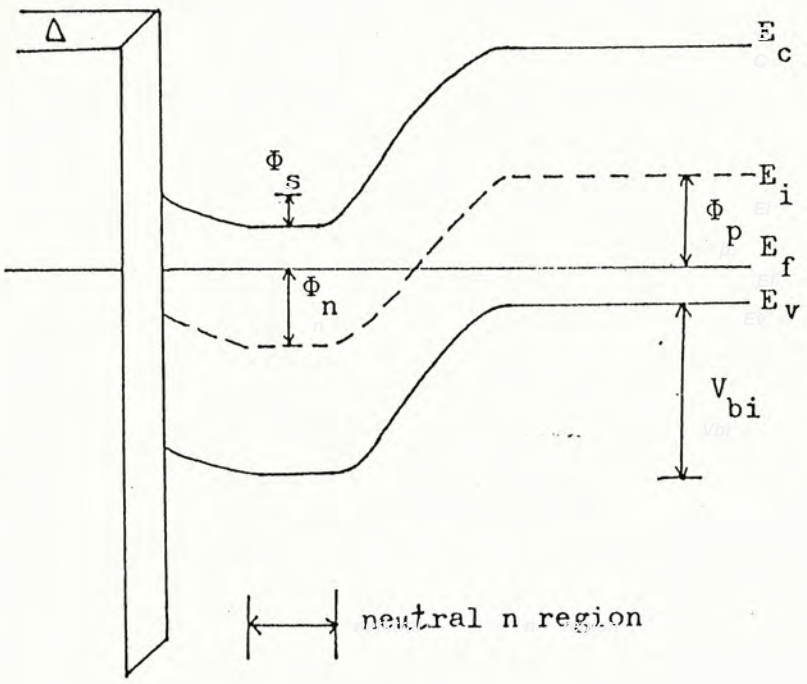

(a)

Fig. 2.6 Energy band diagram of MINP structure when the surface layer is thick.

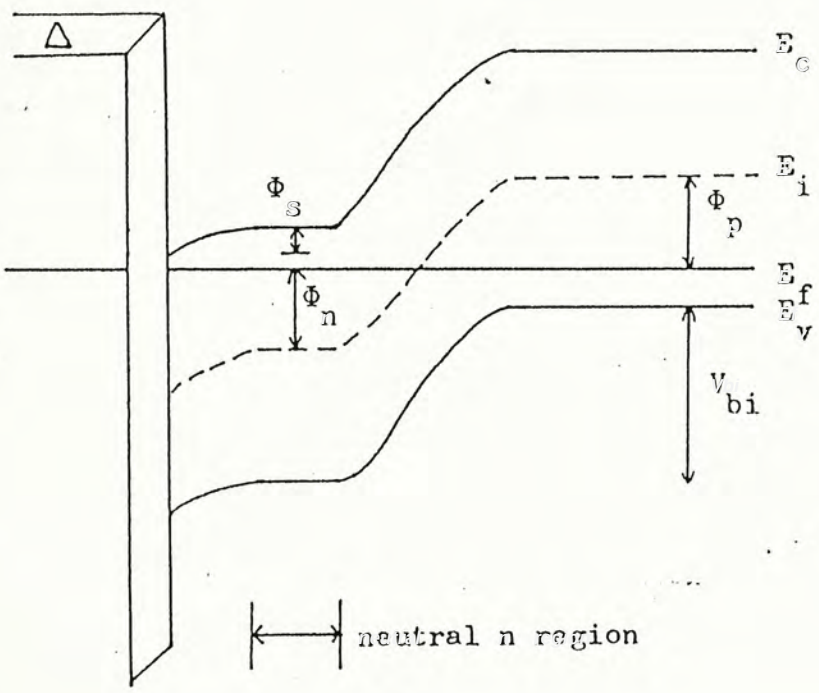

Fig. 2.6 Energy band diagram of MINP structure when the surface layer is thick.

If the energy bands bend upwards on the surface (Fig. 2.6a), holes in the metal will see a potential barrier which is equal to the built in potential plus the difference between the Fermi level and the valence band edge in the bulk [17].

$$\Phi_{h1} = V_{bi} + \left(\frac{V_g}{2} - \frac{kT}{q} \ln \frac{N_A}{n_i} \right) \qquad (2.29)$$

$$\text{where } V_{bi} = \frac{kT}{q} \ln \frac{N_D N_A}{n_i^2}$$

If the energy bands bend downwards (Fig. 2.6b), the potential barrier seen by holes in the metal is then given by

$$\Phi_{h2} = \Phi_{h1} + \Phi_s \qquad (2.30)$$

Fig. 2.7 shows the surface potential against differnt surface layer concentration for two different metals (Mg and Al). Magnesium tends to accumulate the n layer while Alumimum tends to deplete the n layer.

2.1.4 Dark current-voltage characteristic

In forward bias, the hole current density at the metal-semiconductor contact is given by [18]

$$J_p(0) = - q \, v_{TP} \left(p(0) - p_o(0) \right) \qquad (2.31)$$

where $p_o(0)$ = the equilibrium hole concentration at zero bias,

v_{TP} = the transmission velocity at x = 0

= $(A^* T^2)/(qN_v)$ if thermionic emission model applies.

The hole current density $J_p(x)$ on the semiconductor side is given by

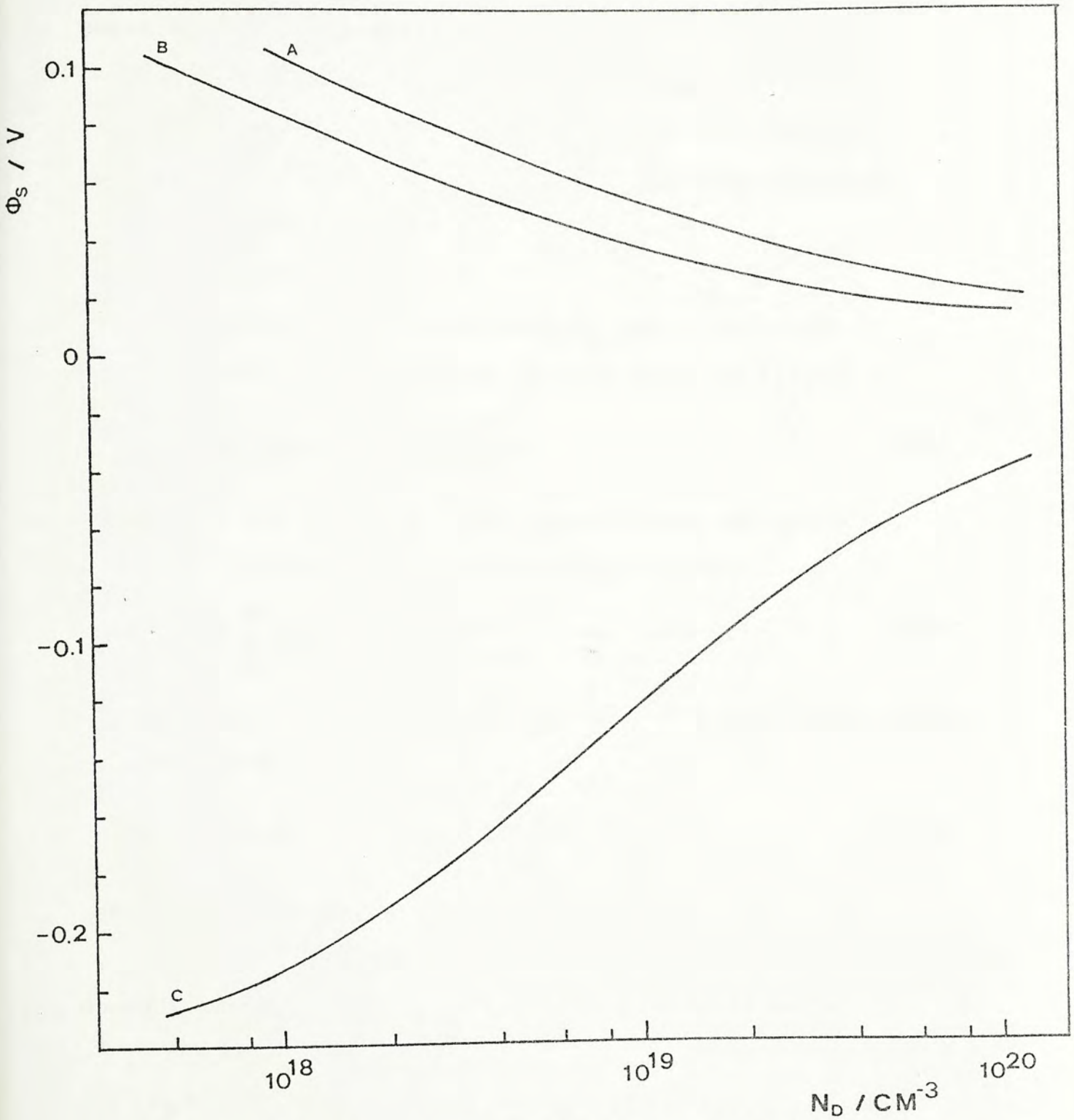

Fig. 2.7 Surface potential versus surface layer concentration.
A - Mg Φ_m = 3.5 V, D_{sn} = 0 cm^{-2};
B - Mg Φ_m = 3.5 V, D_{sn} = $2x10^{12}cm^{-2}$, V_{on} = 0.27 V;
C - Al Φ_m = 4.3 V, D_{sn} = $2x10^{12}cm^{-2}$, V_{on} = 0.27 V.

$$J_p(x) = - q \mu_p p \frac{d\Phi_p}{dx} \qquad (2.32)$$

where u_p = the hole mobility,

ϕ_p = the quasi Fermi level for holes.

Assuming $J_p(x)$ is constant across the depletion region ($0 \leq x \leq W$), (2.32) can be integrated with boundary conditions that

$$\phi_p(W) = \phi_n(W) + V$$

and $$\phi_n(W) = \phi_n(0) = 0$$

where V is the difference between ϕ_p and ϕ_n at $x = W$.

The hole current density is then given by [19,20]

$$J_p = \frac{- q n_i^2 \left(\exp(qV/kT) - 1 \right)}{n(0) \left(1/v_D + 1/v_{TP} \right)} \qquad (2.33)$$

where v_D = the effective diffusion velocity for holes transporting in the barrier region,

$$v_D = \left(\int_0^W \frac{1}{D_p(x)} \frac{n(x)}{n(0)} dx \right)^{-1} \qquad (2.34)$$

If the ratio $n(x)/n(0)$ is small, (2.33) reduces to the case of a Schottky diode with

$$J_p = - A^* T^2 \exp(-q\Phi_{ho}/kT) \left(\exp(qV/kT) - 1 \right) \qquad (2.35)$$

where ϕ_{h0} = the Schottky barrier height.

When the electron concentration is increased by a surface doped layer such that $v_D << v_{TP}$, (2.34) simplifies to

$$v_D = \frac{\overline{D}_p N_D(0)}{Q_D} \qquad (2.36)$$

where $\overline{D}_p$ = the average diffusion constant,

Q_D = the total doped dosage.

Hence (2.33) simplifies to

$$J_p = \frac{-qn_i^2 \overline{D}_p}{Q_D} \left(\exp(qV/kT) - 1 \right) \qquad (2.37)$$

By increasing the surface doping dosage, the hole current density can be reduced to a low value. The total saturation current will finally be limited by the electron diffusion current in the bulk which is given by

$$J_n = \frac{qD_n}{L_n} \frac{n_i^2}{N_A} \left(\exp(qV/kT) - 1 \right) \qquad (2.38)$$

2.2 Antireflection Coating - Insulator - n - p Region

2.2.1 Surface recombination loss

The advantage of the MINP structure [21,22] has been attributed to the improved passivation of surface states by optimizing the electron concentration along the cell surface.

The contribution to the dark current density from recombination along the surface between grid lines in a p type base cell is given by

$$J_{so} = q \sigma_T v_T N_T n_i^2 / n_s \qquad (2.39)$$

where σ_T = the capture cross-section of the surface states,

v_T = the electron thermal velocity,

n_i = the intrinsic carrier concentration,

n_s = the electron concentration at the surface,

N_T = the density of surface states with an energy of ($KT \ln(n_s/n_i)$) of midgap.

Since N_T is relatively independent of n_s at the doping level of interest [23],

$$J_{so} \propto n_i^2 / n_s \qquad (2.40)$$

Taking into account the bandgap narrowing effect, there will be an optimum value of n_s for minimum J_{so}. From Lanyon [24], the bandgap narrowing is given as

$$\Delta E_g = 22.5 \times 10^{-3} (n/10^{18})^{1/2} \text{ eV} \quad \text{for nondegenerate semiconductor, and}$$

$$\Delta E_g = 162 \times 10^{-3} (n/10^{20})^{1/6} \text{ eV} \quad \text{for degenerate semiconductor} \qquad (2.41)$$

The intrinsic concentration is given by

$$n_i^2 = n_{ie}^2 \exp(\Delta E_g / kT) \qquad (2.42)$$

where n_{ie} = the intrinsic concentration without bandgap narrowing.

Setting $dJ_{so}/dn_s = 0$, the optimum surface concentration n_s^{opt} is found to be given by

$$n_s^{opt} = (2kT/22.5x10^{-3})^2 \; x10^{18} \; cm^{-3} \quad \text{for nondegenerate case, and}$$

$$n_s^{opt} = (6kT/162x10^{-3})^6 \; x10^{20} \; cm^{-3} \quad \text{for degenerate case} \qquad (2.43)$$

At room temperature,

$$n_s^{opt} = 5.3x10^{18} \; cm^{-3} \quad \text{for nondegenerate case, and}$$

$$n_s^{opt} = 7.8x10^{19} \; cm^{-3} \quad \text{for degenerate case.}$$

We have included also the degenerate case in the above expressions as it is not uncommon that such concentration is reached in practice. The optimum doping concentration is higher in the degenerate case than the non-degenerate case. However, these values are substantially lower than the heavily doped emitter in conventional p-n junction.

2.2.2 Series resistance loss

The series resistance of the induced inversion layer of MIS grating cell (Fig. 2.1a) is usually high. A simple calculation shows that for a minimum power loss, the grating spacing should be [25]

$$S = \left(\frac{6 W_c V_{mp}}{R_s J_{mp}} \right)^{1/3} \qquad (2.44)$$

where W_c = the width of the contact lines,

R_s = the sheet resistivity of the inversion layer,

V_{mp}, J_{mp} = the voltage and current density under maximum power condition.

Addition of a surface layer will not only passivate the surface and reduce the recombination current (section 2.2.1), but also lower the series resistance.

The sheet resistivity of the surface layer is given by [26]

$$R_s = \left(\mu_n |Q_n| \right)^{-1} \qquad (2.45)$$

where u_n = the lateral electron mobility,

$$Q_n = - Q_{ox} - Q_D - Q_{SC} \qquad (2.46)$$

where Q_{ox} = the AR (oxide) charge density,

Q_D = the dose of surface doped layer,

Q_{SC} = the space charge density.

$$Q_{SC} = - q N_A x_{dmax} \qquad (2.47)$$

where x_{dmax} = the maximum depletion width,

$$x_{dmax} = \left(\frac{4 \epsilon_s kT \ln(N_A/n_i)}{q^2 N_A} \right)^{1/2} \qquad (2.48)$$

Fig. 2.8 shows the sheet resistivity against dose with oxide charge density as a parameter. The lower sheet resistivity suggests that a wider grating spacing can be used to lower the shadow loss.

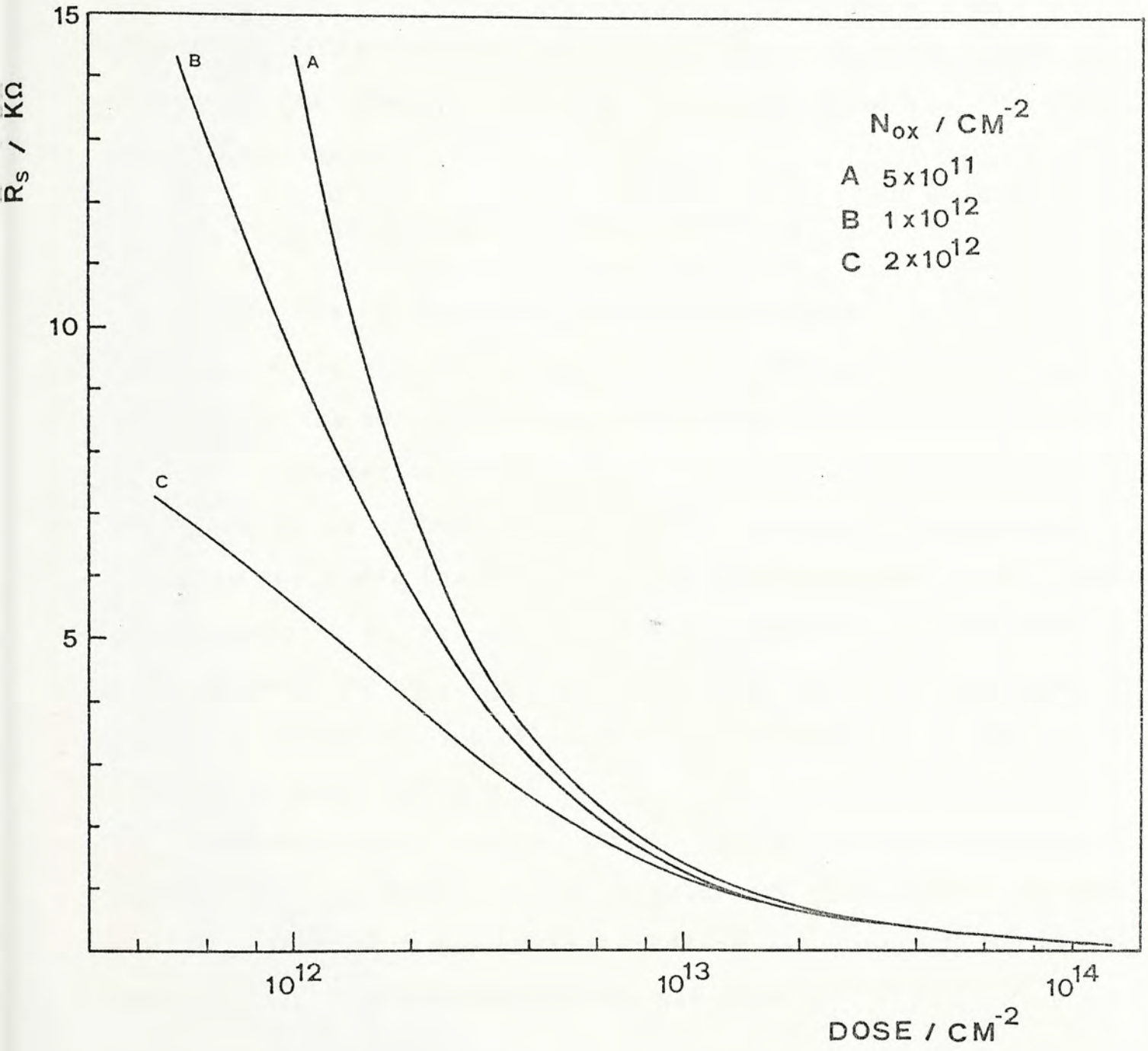

Fig. 2.8 Sheet resistivity versus dose with oxide charge density as a parameter.

2.3 Illuminated Current - Voltage Characteristic

A simple distributed diodes model [27] is used to relate the metal-insulator-n-p region and the AR-insulator-n-p region. The schematic of the model is illustrated in Fig. 2.9 . The generation andrecombination in the thin surface layer are neglected for simplicity. The dark current of the ith diode element is given by

$$I_{di} = I_{o1} \exp(qV_{di}/kT) + I_{o2} \exp(qV_{di}/2kT) \qquad (2.49)$$

where V_{di} = the diode voltage of the ith element,

I_{o1} = the saturation current due to diffusion in the bulk,

I_{o2} = the saturation current due to recombination in the depletion region.

Each diode element is connected through a resistance R_i which is the sheet resistance of the induced/doped layer. The AR-insulator-n-p region is connected directly to the metal-insulator-n-p region. The dark current of the metal-insulator-n-p region is given by (2.33). A series resistance of the metal grid R_m is also included.

The cell output characteristic can be found by assuming a voltage value at node n, slightly below the open circuit voltage and stepping along the string, addding new current I_i at each node. V_n is then decremented to generate the whole current - voltage characteristic.

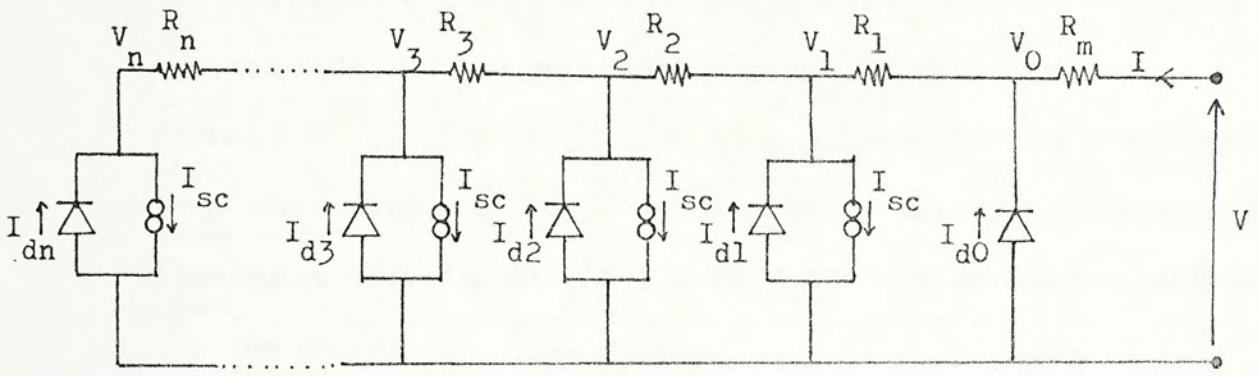

Fig. 2.9 Schematic of a distributed diode model.

2.4 Summary

We have considered the theoretical background of the metal-insulator-n-p grating solar cell.

In the metal-insulator-n-p region, expressions for the potential barrier enhancement and the ideality factor have been obtained when 1. n^+ and p regions are depleted and 2. n^+ region is depleted only. When the surface layer is thick enough that a neutral n region is formed, the structure is treated as a MIS barrier in cascade with a p-n junction.

The hole current density has shown to be reduced by increasing the surface doping dosage. The total saturation current decreases until it is limited by the electron diffusion current in the bulk.

In the antireflection coating-insulator-n-p region, two major loss mechanisms - surface recombination loss and series resistance loss have been considered.

The optimum surface doping concentration is found for both degenerate and non-degenerate cases which are substantially lower than the heavily doped emitter in conventional p-n junction.

The sheet resistivity is lowered when a surface doping layer is incorporated which suggests that a wider grating spacing can be used to reduce the shadow loss.

Finally, a simple distributed diodes model is used to relate the metal-insulator-n-p region and the antirflection coating-insulator-n-p region.

References

[1] J.M. Shannon, "Control of Schottky barrier height using highly doped surface layers," Solid State Ele., Vol. 19, p.537, 1976.

[2] J.M. Shannon, "Increasing the effective height of a Schottky barrier using low energy ion implantation," Appl. Phys. Lett., Vol. 25, p.75, 1974.

[3] J.M. Shannon, "Reducing the effective height of a Schottky barrier using low energy ion implantation," Appl. Phys. Lett., Vol. 24, p.369, 1974.

[4] H.C. Card, "One dimensional analysis of heat treated Aluminium-silicon junctions," Inst. Phys. Conf., Ser. no. 22, p.129, 1974.

[5] J. Basterfield and J.M. Shannon, "The nature of barrier height variations in alloyed Al-Si Schottky barrier diodes," Solid State Ele., Vol. 18, p.290, 1975.

[6] A. Van der Ziel, "Metal-p-n Schottky barrier diodes," Solid State Ele., Vol. 20, p.269, 1977.

[7] P.S. Rao and S.K. Sharma, "Theoretical analysis of a metal p-n Schottky barrier solar cell," Solid State Ele., Vol. 25, p.959, 1982.

[8] S.S. Li, "Theoretical analysis of a novel MPN Gallium Arsenide Schottky barrier solar cell," Solid State Ele., Vol. 21, p435, 1978.

[9] S.B. Roy and A.N. Daw, "Effect of non-uniformly doped surface layer on the barrier height of a Schottky contact," Solid State Ele., Vol. 23, p.949, 1980.

[10] S.B. Roy, T.K. Sinha and A.N. Daw, "Analysis of a non-

uniformly doped MPN silicon Schottky barrier solar cell," Solid State Ele., Vol. 26, p.353, 1983.

[11] C.Y. Wu, "Barrier height enhancement of the Schottky barrier diode using a thin uniformly doped surface layer," Solid State Ele., Vol. 24, p.857, 1981.

[12] C.Y. Wu, "An analysis model for barrier height enhancement of the Schottky barrier diode using low energy ion implantation," J. Appl. Phys., Vol. 54, p.971, 1983.

[13] C.Y. Wu, M.C. Chang and A.J. Shey, "A computer-aided simulation model for the I-V characteristic of M-n-p silicon Schottky barrier diodes produced by use of low energy Arsenic ion implantation," Solid State Ele., Vol. 26, p.893, 1983.

[14] S.B. Roy and A.N. Daw, "Effect of the presence of an inversion layer in an MPN structure," Solid State Ele., Vol. 25, p.169, 1982.

[15] C.S. Hoi, Ph.D research topic.

[16] C.S. Hoi, "Studies of the electrical characteristic of MIS/MINP solar cells," M. Phil. thesis, CUHK, 1983.

[17] Y.P Pai, H.C. Lin, M. Peckerar and R.L. Kocher, "Ion implanted Schottky barrier solar cell," IEDM Tech. Dig., p.470, 1977.

[18] C.R. Crowell and S.M. Sze, "Current transport in metal semiconductor barriers," Solid State Ele., Vol. 9, p.1035, 1966.

[19] Y.P. Pai and H.C. Lin, "Current transport in an ion implanted diode," Solid State Ele., Vol. 24, p.929, 1981.

[20] Y.P. Pai and H.C. Lin, "Analysis of ion implanted solar cells," 13th IEEE Photov. Spec. Conf., p.661, 1978.

[21] M.A. Green et al., "The MINP solar cell - a new high voltage, high efficiency silicon solar cell," 15th IEEE Photov. Spec. Conf., p.1405, 1981.

[22] A.W. Blakers and M.A. Green, "678 mV open circuit voltage silicon solar cells," Appl. Phys. Lett., Vol. 39, p.483, 1981.

[23] J. Snel, "Doped Si/SiO_2 interface," Solid State Ele., Vol. 24, p.135, 1981.

[24] H.P.D. Lanyon and R.A. Tuft, "Bandgap narrowing in moderately to heavily doped silicon," IEEE Trans. Ele. Dev., Vol. 26, p.1014, 1979.

[25] Y.W. Lam, "minMIS Schottky barrier solar cells - a review," Radio & Electronic Engineer, Vol. 51, p.447, 1981.

[26] G.C. Salter and R.E. Thomas,"Silicon solar cells using natural inversion layers found in thermally oxidized p silicon," Solid State Ele., Vol. 20, p.95, 1977.

[27] C.E. Norman and R.E. Thomas, "Computer modeling of inversion layer solar cells," Photov. Solar Energy Conf., p.910, 1977.

3. PRE-PROCESSING HIGH TEMPERATURE HEAT TREATMENT ON MIS SOLAR CELLS

3.1 Introduction

High temperature step is known to be detrimental in solar cell processing. Fischer and Pschunder [1] observed that the carrier lifetimes of their completed n^+p cells reduced substantially with respect to as-grown crystal measured by the photo-current decay method. The initial lifetime in the as-grown crystal is changed by process dependent effects [2]. A reversible increase at low temperature annealing is followed by an irreversible degradation at higher temperature where normal diffusion process takes place. Graff [2] attributed the effect to the transformation of the oxygen donor-complexes into other electrically inactive configuration near 600°C.

Kalejs and Ladd [3] annealed their samples at 1200°C for 10 and 60 minutes prior to normal process. They found that the efficiency degraded to 88 % and 74 % of those without pre-processing anneals for FZ 5 ohm-cm p type samples and 95 % and 86 % for CZ 1 ohm-cm p type samples.

In the above studies, a p-n junction structure was employed, which inevitably required a "high temperature" "diffusion" step. The two effects - high temperature treatment and diffused impurities cannot be isolated. We investigate the effects due to high temperature treatment alone by employing a

MIS structure. A MIS cell without any high temperature heat treatment is used as control. The highest temperature encountered by the control MIS cell is 500°C at which the back contact is sintered. This allows studies on the effects of high temperature treatment at the range of diffusion process temperature or annealing temperature of ion implantation. It also enables one to anticipate the effects of doping alone, as in the case of the MINP structure (chapter 4 and chapter 5).

3.2 Theory

3.2.1 Illuminated current - voltage characteristic

The schematic of a metal insulator p-silicon solar cell under illumination is shown in Fig. 3.1. The current flow consists of three components -

1. tunneling current between the metal and the minority carrier band,
2. tunneling current between the metal and the majority carrier band, and
3. tunneling current between the metal and surface states.

Following Ng and Card [4] and Hoi [5], the current components are given as follows.

1. Minority current

The minority current under illumination is given by

$$J_n = \frac{qF_o - \frac{qD_n n_{po}}{L_n}(\exp(qV/kT) - 1)}{1 + \frac{qD_n n_{po}}{L_n Q}\exp(V_s/kT)} \qquad (3.1)$$

$$\text{where} \quad Q = \frac{4\pi m^*_{te} q(kT)^2}{h^3}\exp(q\Phi^o_n/kT)\exp(-\chi_e^{1/2}\delta) \qquad (3.2)$$

The symbols carry their usual meanings.

2. Majority current

The majority current is given by [6]

$$J_p = \frac{4\pi m^*_{th} q(kT)^2}{h^3}\exp(-q\Phi^o_h/kT)\exp(-\chi_h^{1/2}\delta)\exp(-V_i/kT)\,(\exp(qV/kT) - 1) \qquad (3.3)$$

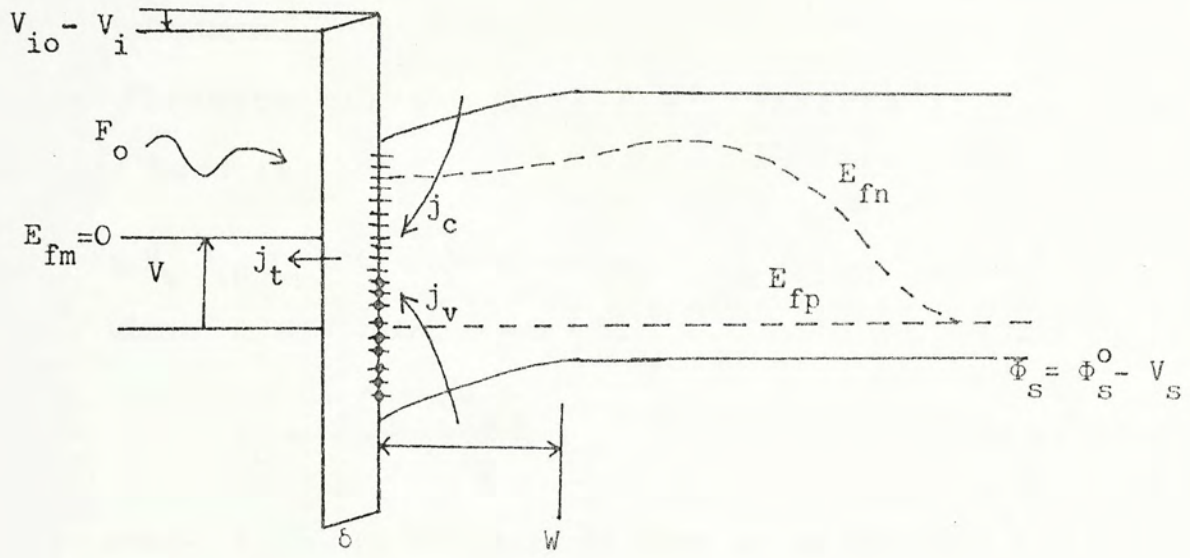

Fig. 3.1 Energy band diagram of MIS(pSi) solar cell under illumination.

3. Current through interface states [7]

The occupancy of the interface states is determined by a competition between the tunneling transi tions to the metal and the capture of carriers from the conduction and valence bands of the semiconductor.

The electron current into the interface states from the conduction band is

$$j_c = q N_s V_{th} \sigma_n \left((1-f_t) n(0) - f_t n_1 \right) \tag{3.4}$$

where $n_1 = N_c \exp(-(E_c - E_t)/kT)$ (3.5)

$$f_t = \frac{\tau_t f_{to} + \tau_s f_m}{\tau_t + \tau_s} \tag{3.6}$$

where f_{to} = the occupancy if there is no interface state tunnel current

$$= \frac{n(0)\sigma_n + p_1 \sigma_p}{(n(0)+n_1)\sigma_n + (p(0)+p_1)\sigma_p} \tag{3.7}$$

$$\tau_s = \left(V_{th} \left(\sigma_n (n(0)+n_1) + \sigma_p (p(0)+p_1) \right) \right)^{-1} \tag{3.8}$$

V_{th} = the thermal velocity of the carriers,

$\sigma_{n,p}$ = the capture crosssection of electrons, holes,

N_s = the interf$_a$ce states density,

f_m = the occupancy in metal.

The hole current into the interface states (electron current form the interface states to the valence band) is

$$j_v = q N_s V_{th} \sigma_p \left(f_{tp}(0) - (1-f_t) p_1 \right) \tag{3.9}$$

where $p_1 = N_v \exp\left(-(E_t - E_v)/kT\right)$ (3.10)

The electron tunnel current from the interface states into the metal is

$$j_t = \frac{qN_s}{\tau_t} (f_t - f_m) \qquad (3.11)$$

where τ_t = the interface state tunneling time constant

$$= \tau_o \exp (\lambda_h^{1/2} \delta)$$

For a moderate surface potential, the charge in the space charge region is given by [8]

$$Q_{SC} = (2 \epsilon_s kT N_A (q\Phi_s/kT + n(0)/N_A))^{1/2} \qquad (3.12)$$

The oxide voltage V_i is given by

$$V_i = - \frac{\delta}{\epsilon_i} (\Delta Q_{SC} + \Delta Q_{SS}) \qquad (3.13)$$

An iterative procedure using the above equations is described by Ng and Card [4] to calculate the current voltage characteristic of MIS solar cells.

3.2.2 Carrier lifetime

Fossum [9] developed a theoretical model that described the dependence of the "fundamental limit" of carrier lifetime on doping density, which was based on the equilibrium solubility of a particular defect in nondegenerate doped silicon.

The total defect density, N_d that is frozen in at $T=T_f$ is given by

$$N_d(N_A) = N_d^o (1 - \frac{N_A}{2n_i} + (1+(N_A/2n_i)^2)^{1/2}) \quad \text{for p type} \qquad (3.14)$$

$$N_d(N_D) = N_d^o \left(1 + \frac{N_D}{2n_i} + (1+(N_D/2n_i)^2)^{1/2} \right) \quad \text{for n type} \qquad (3.15)$$

N_d^o is the solubility of the neutral defect in silicon at the effective temperature of defect formation.

$$N_d^o(T_f) = N_{Si} \exp(-E_a/kT_f) \qquad (3.16)$$

where N_{Si} = the atomic density of silicon (5×10^{22} cm^{-3}),

E_a = the activation energy required to form the defect in silicon lattice,

T_f = the effective temperature of formation of defect,

n_i = the intrinsic carrier concentration evaluated at $T=T_f$.

Assuming Shockley-Read-Hall model [10] for recombination through a single level trap, the rate of recombination is given by

$$U = \frac{pn - n_i^2}{\frac{1}{C_p^- N_d}\left(n + \frac{1}{g_d} n_i \exp((E_d-E_i)/kT) \right) + \frac{1}{C_n^o N_d}\left(p + g_d n_i \exp((E_i-E_d)/kT) \right)} \qquad (3.17)$$

where $C_p^- = \sigma_p V_{th}$ = the hole capture rate per occupied trap,

$C_n^o = \sigma_n V_{th}$ = the electron capture rate per vacant trap,

E_i = the intrinsic Fermi level,

g_d = the non-unity degenerate factor.

For the low injection case, the minority electron lifetime in p silicon is given by

$$\tau_n = \frac{n - (n_i^2/N_A)}{U} \qquad (3.18)$$

while the minority hole lifetime in n silicon is given by

$$\tau_p = \frac{p - (n_i^2/N_D)}{U} \qquad (3.19)$$

For high injection case, $p \approx n >> N_D$, N_A , the carrier lifetime is given by

$$\tau_H = \frac{p}{U} = \frac{1}{N_d} \left(\frac{1}{C_p^-} + \frac{1}{C_n^o} \right) \qquad (3.20)$$

Fossum [9] suggested that the frozen-in temperature was around 330°C with an activation energy of 1.4 eV which approximated the activation energy of a silicon divacancy.

If the silicon is cooled too quickly during growth or processing, the defects may be frozen in at a temperature higher than T_f. The resulting higher defect density will lead to a lifetime lower than the "fundamental limit".

An empirical formula describing the dependence of lifetime on doping concentration is given by [11]

$$\tau_n^p = \frac{\tau_{no}^{po}}{1 + \frac{N_A^D}{N_{oA}^{oD}}} \qquad (3.21)$$

where $\tau_{po} = 3.52 \times 10^{-7}$ sec, $\tau_{no} = 1.70 \times 10^{-5}$, and $N_{oD}^{oA} = 7.10 \times 10^{15}$ cm^{-3}.

A higher doping concentration will result in a lower minority carrier lifetime.

3.3 Experimentals

3.3.1 Pre-processing heat treatment

The wafers used in this study were 0.5 ohm-cm (100) p type wafers supplied by Wacker (unless otherwise stated). Two sets of experiments on pre-processing high temperature heat treatment were performed. The conditions were

A - isochronal heat treatment for 15 min at temperature 700, 800, and 900 ^{o}C plus untreated control sample,

B - isothermal heat treatment at 800^{o}C for 0.5, 2 and 4 hours plus untreated control sample.

Wafers were chemically cleaned before heat treated in a double wall furnace flushed with nitrogen. Thin oxide grown during heat treatment was etched. Wafers were then subjected to normal MIS cell fabrication procedure.

3.3.2 Normal MIS cell fabrication procedure

2 inches wafer was sliced into quarters that were suitable for fabrication of 1 cm^{2} area cells. After the wafers were chemically cleaned, thin oxide layer of thickness 17 - 19 A, measured by ellipsometer at wavelength 6328 A, was thermally grown at 500^{o}C for 30 min under dry oxygen ambient (with flow rate of 2 l/min). The oxide thickness is critical in producing high efficiency MIS solar cell [5]. Various methods of preparing the thin oxide film has been reviewed in [12]. We found that low temperature thermal growth was highly reproducible in the thickness range of interest.

1 um thick Alumimum was evaporated at pressure < $2x10^{-5}$ τ on the backside. It was then sintered at 500°C for 30 min under nitrogen ambient (with flow rate of 2 l/min) [5,13].

2 um thick Magnesium was evaporated at pressure < $1x10^{-5}$ τ through a silicon shadow mask [14,15] on the front surface to form the MIS contact.

SiO of 800 A thick was evaporated as a quarter wavelength antireflection coating [16]. It also protected the reactive Magnesium grid from the environment. The refractive index of true SiO is 1.9. However, depending on the conditions of evaporation, the film obtained may range from SiO to SiO_2 with corresponding refractive index of 1.9 and 1.46 [17,18]. The refractive index in this study was tightly controlled to lie in 1.85 - 1.9 with a fast evaporation rate of 10 - 15 A/sec under pressure < $3x10^{-5}$ τ.

The completed cells were ready for measurement.

3.3.3 Measurements

1. Illuminated current - voltage characteristics at AM1.5

Solar light source was simulated by a halogen filled tungsten bulb with dichroic mirror at color temperature 3400 K (Philips, 6423). AM1.5 illumination was calibrated by a Solarex reference cell. A solar cell characteristic plotter [19] with platform by which the temperature of the device under test could be controlled was used to measure the illuminated current voltage characteristics. From which the total area efficiency

and fill factor were deduced. The open circuit voltage and short circuit current were measured directly with a digital meter to eliminate any possible loading effect.

2. V_{oc} / J_{sc} measurement under various illumination

V_{oc} / J_{sc} measurement [20] under various illumination were taken. The ideality factor and saturation current near the maximum power point were then deduced.

3. Minority carrier lifetime

Photo-induced voltage decay method [21-23] was employed to measure the minority carrier lifetime. General Radio 1531-AB Strobotac electronic stroboscope and Philips PM3234 storage scope were used.

4. Spectral response

Bausch and Lomb high intensity grating monochromator with tungsten halide source and visible (350-850 nm) and infra-red (0.7-1.6 um) grating assemblies were employed to meaure the spectral response. The raw data were adjusted with the output intensity of the monochromator measured by International Light IL1500 radiometer which possessed a flat spectral response from 400 nm upto 2.5 um.

3.4 Results and Discussion

3.4.1 Isochronal heat treatment

The results of isochronal heat treatment of 15 min at various temperature are shown in Fig. 3.2 - Fig. 3.9.

Fig. 3.2 shows that the minority carrier lifetime of the heat treated samples are lower than that of the control sample. This is consistent with that observed by Graff [2]. An irreversible lifetime degradation occurs for T > 600°C. Although the "fundamental limit" of lifetime is independent of temperature history from the model developed by Fossum [9], the practical lifetime is process dependent and depends on other effects such as impurities in the semiconductor and defect density may be frozen in at $T > T_f$ resulting in a lower lifetime. Partial recovery of lifetime during the 500°C, 30 min sintering step is suggested since there is no difference among the heat treated samples.

The open circuit voltage shown in Fig. 3.3 decreases as the heat treatment temperature increases with larger drops occurs near 900°C. The short circuit current (Fig. 3.4) decreases steadily upto 800°C at which it reaches the minimum.

There is no apparent change in the fill factor under various heat treatment temperature as shown in Fig. 3.5.

Due to the combined decreases in open circuit voltage and short circuit current, the total area efficiency (Fig. 3.6) decreases as the heat treatment temperature increases.

The decrease in open circuit voltage can be partly explained by the lifetime degradation. Inspecting (3.1) and writing D_n/L_n

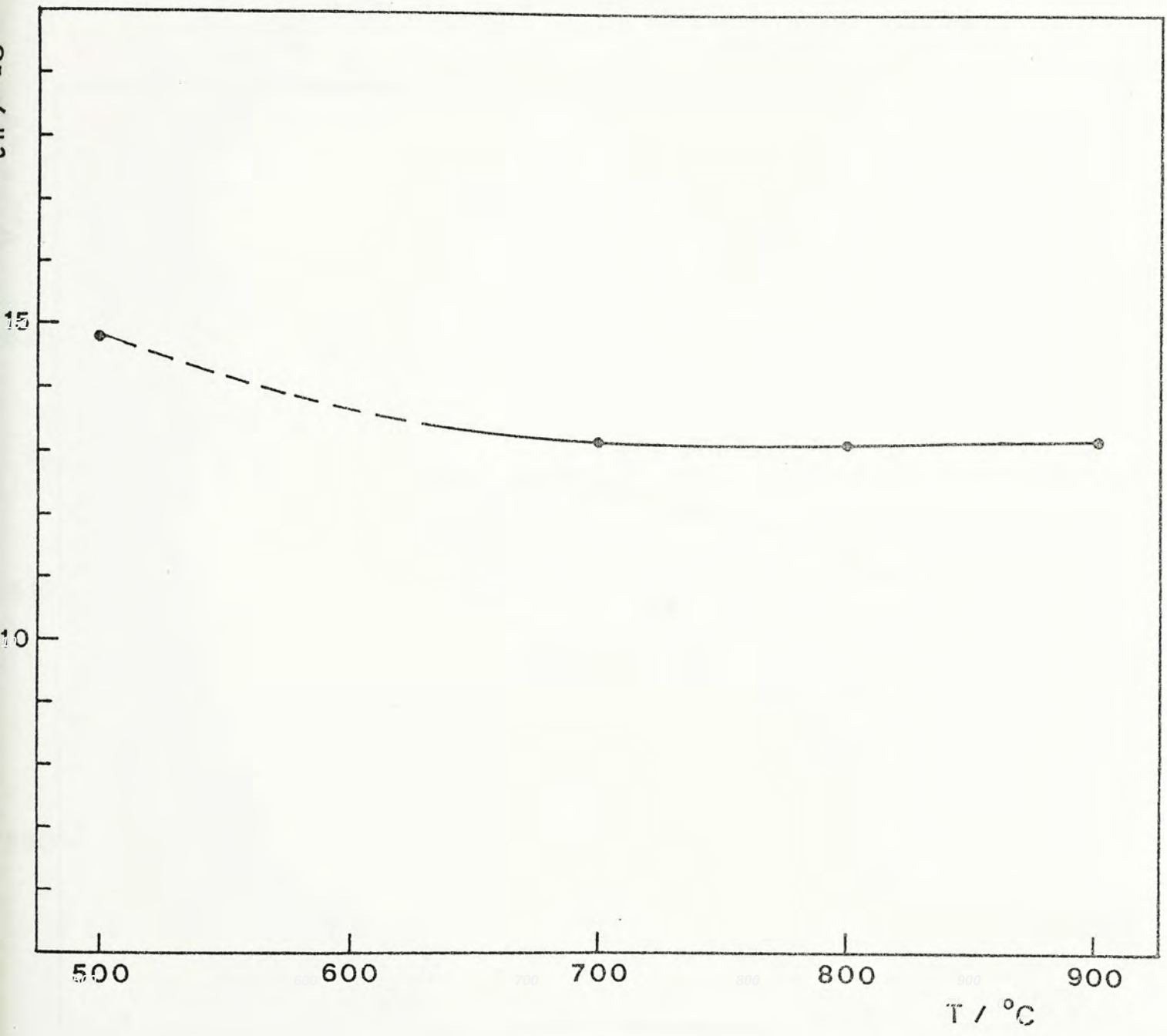

Fig. 3.2 Minority carrier lifetime versus heat treatment temperature. MIS cell without pre-process heat treatment is indicated for reference at the highest temperature encountered.

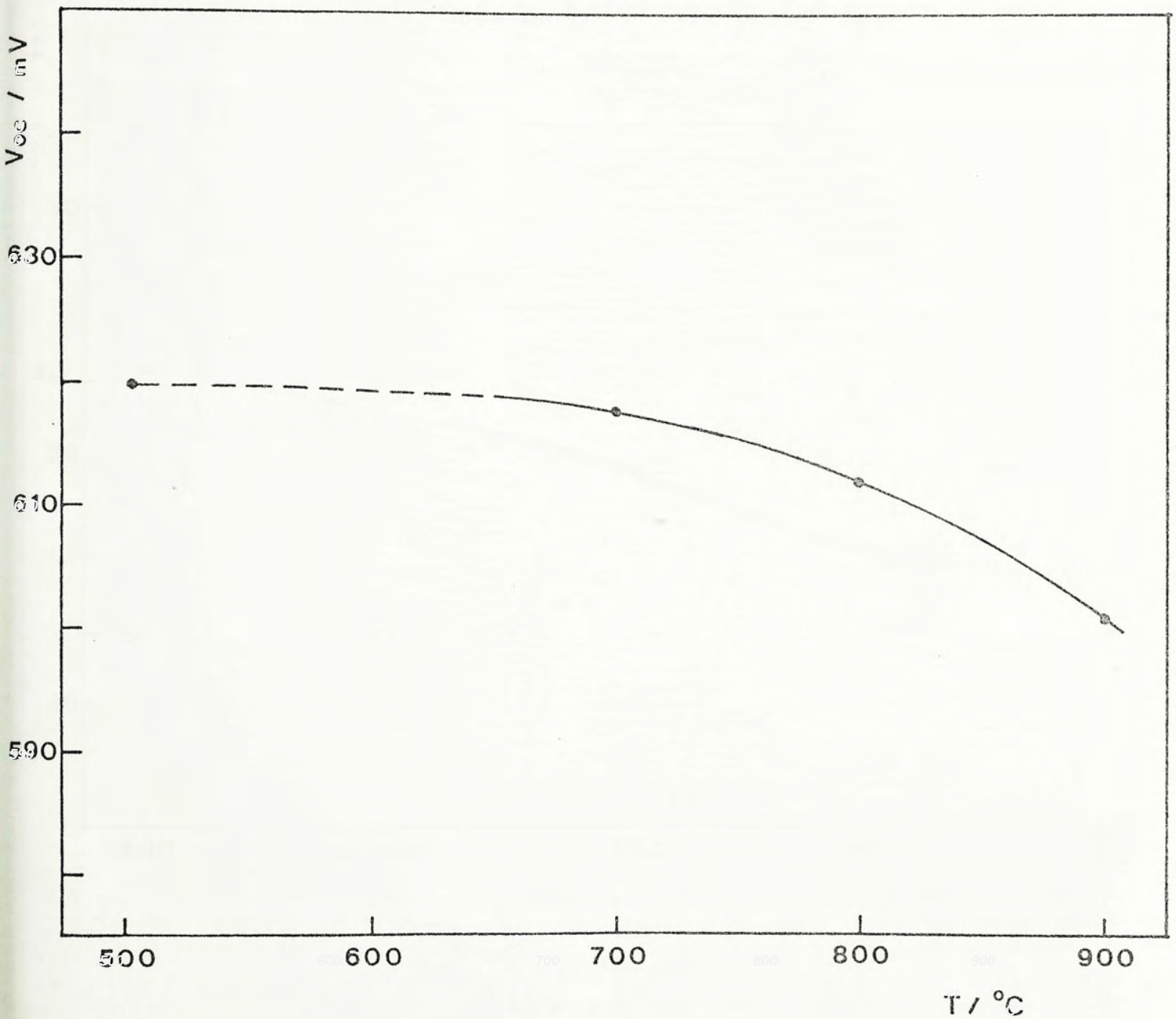

Fig. 3.3 Open circuit voltage versus heat treatment temperature.

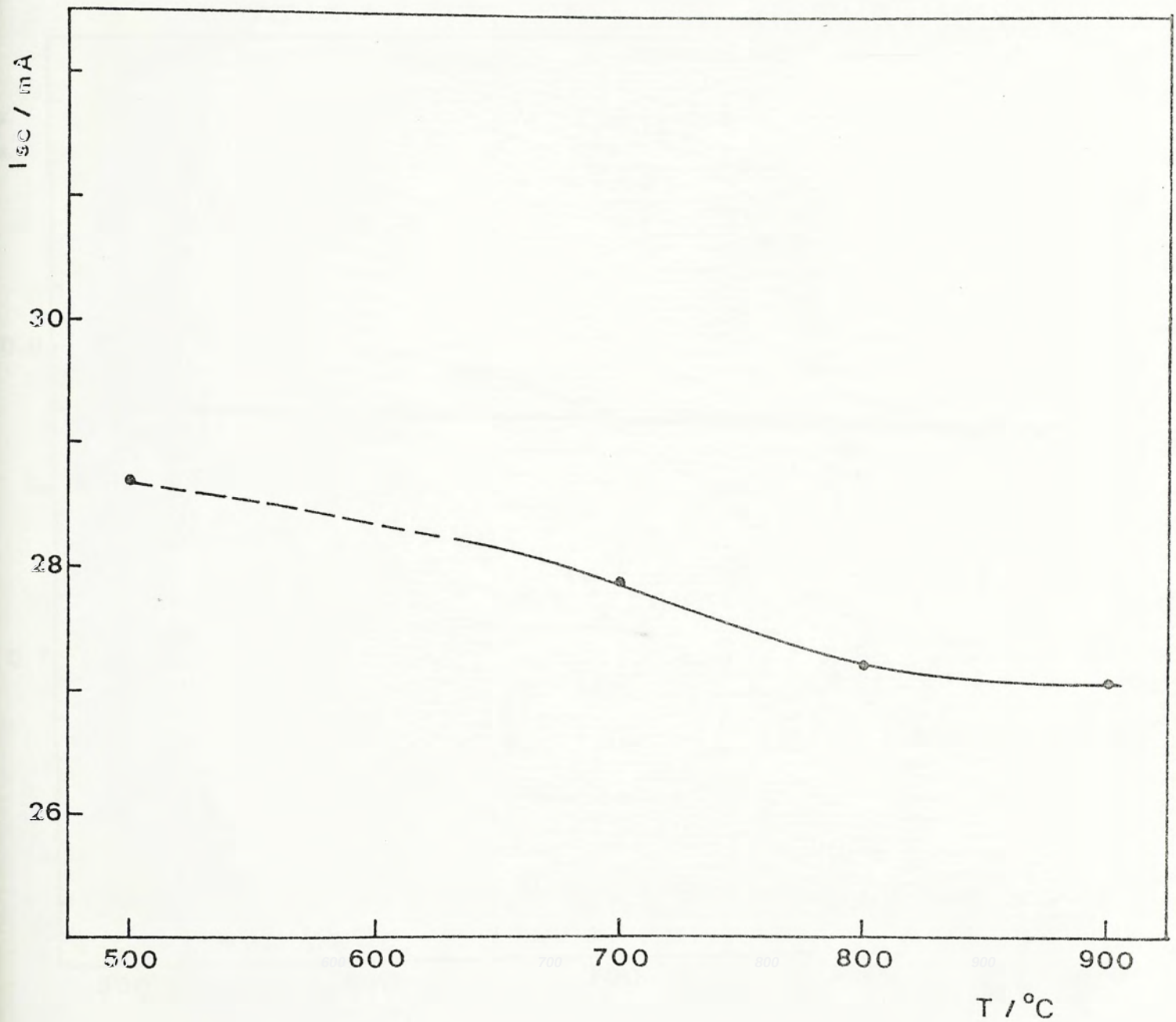

Fig. 3.4 Short circuit current versus heat treatment temperature.

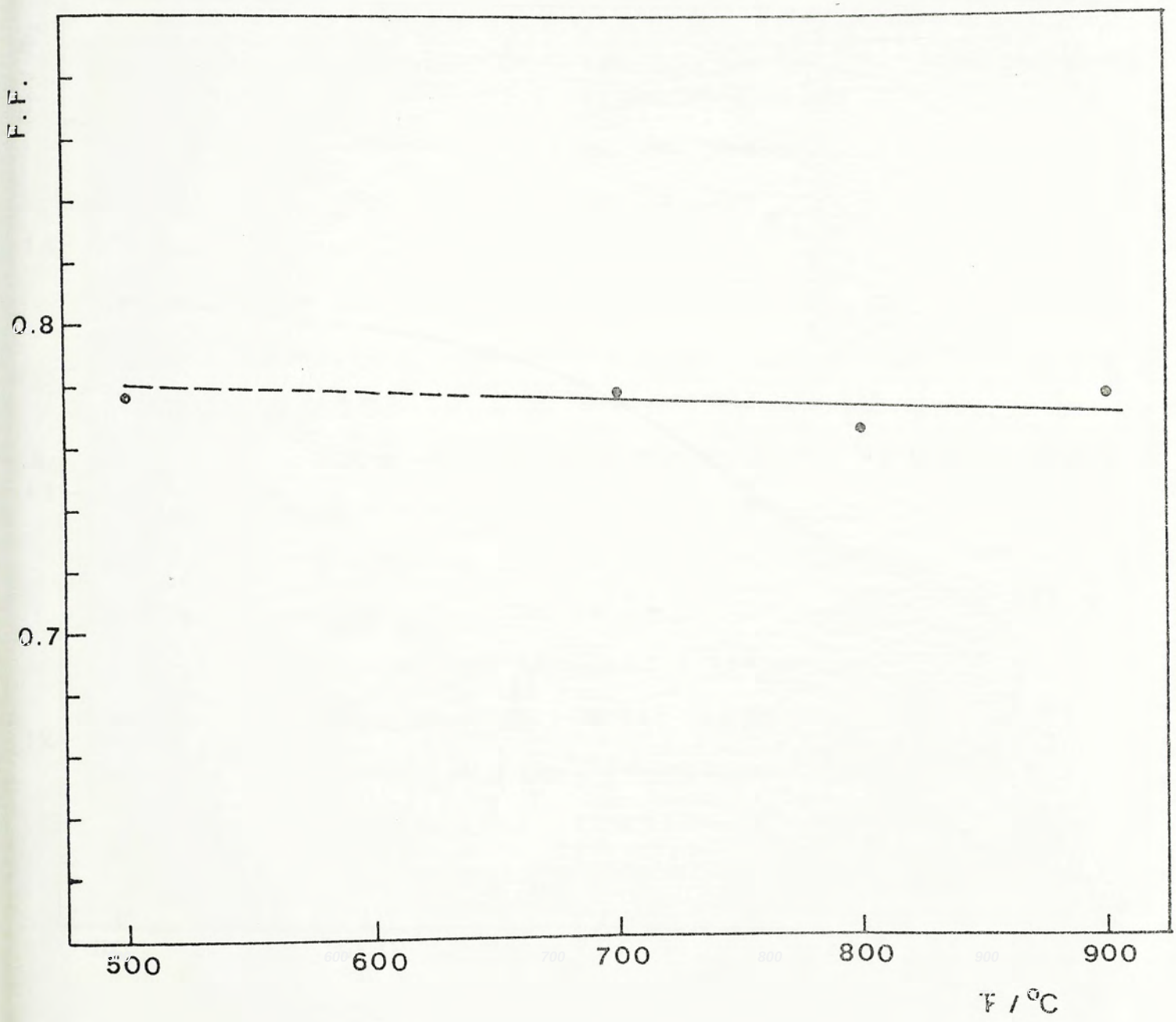

Fig. 3.5 Fill factor versus heat treatment temperature.

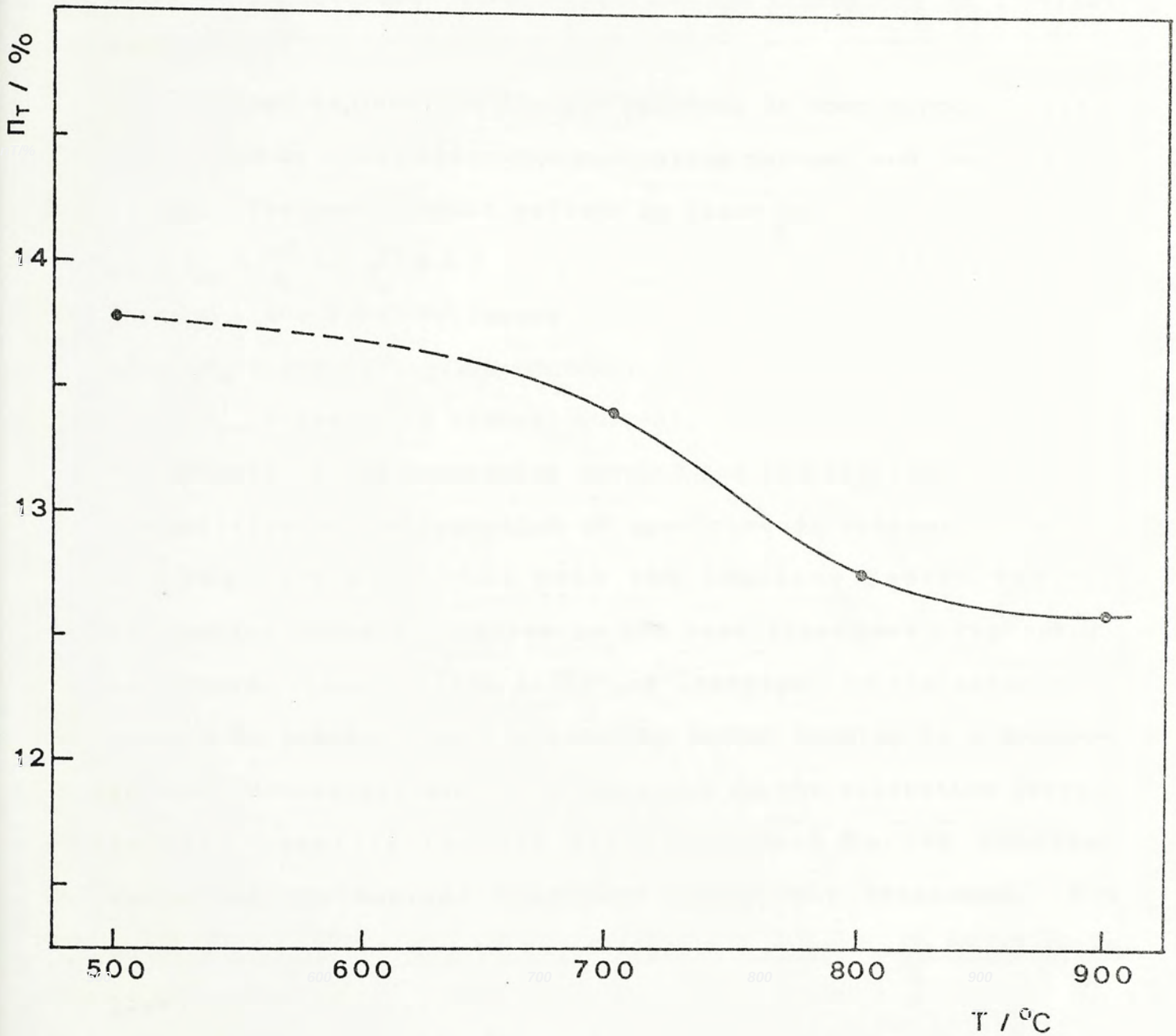

Fig. 3.6 Total area efficiency versus heat treatment temperature.

by $(D_n/\tau_n)^{1/2}$, the open circuit voltage can be seen to decrease as τ_n decreases. Hoi [5] has calculated the illuminated current voltage characteristics and observed that a decrease in both open circuit voltage and efficiency as lifetime decreased.

Another explanation for the decrease in open circuit voltage is reached by considering the saturation current and the ideality factor. The open circuit voltage is given by

$$V_{oc} = \frac{nkT}{q} \ln(\frac{I_{sc}}{I_o} + 1) \qquad (3.22)$$

where n = the ideality factor,

I_o = the saturation current,

I_{sc} = the short circuit current.

The effects of the saturation current and the ideality factor are competitive in the reduction of open circuit voltage. Fig. 3.7 and Fig. 3.8 show that both the ideality factor and the saturation current increase as the heat treatment temperature increases. However, the effect of increase in the saturation current is greater than the ideality factor leading to a decrease in open circuit voltage. The increases in the saturation current and the ideality factore are attributed to the enhanced recombination current component after heat treatment. The saturation current due to the diffusion component in the base is given by

$$I_{od} = q \frac{D_n}{L_n} \frac{n_i}{N_A} = q (\frac{D_n}{\tau_n})^{1/2} \frac{n_i^2}{N_A} \qquad (3.33)$$

For $N_A = 3 \times 10^{16}$ cm^{-3}, $D_n = 20$ cm^2/s, $\tau_n = 15$ us (measured), $I_{od} = 1.3 \times 10^{-12}$ A/cm^2 which is in good agreement with the control MIS cell. However, from Fig. 3.2, the lifetime degrades to 13 us

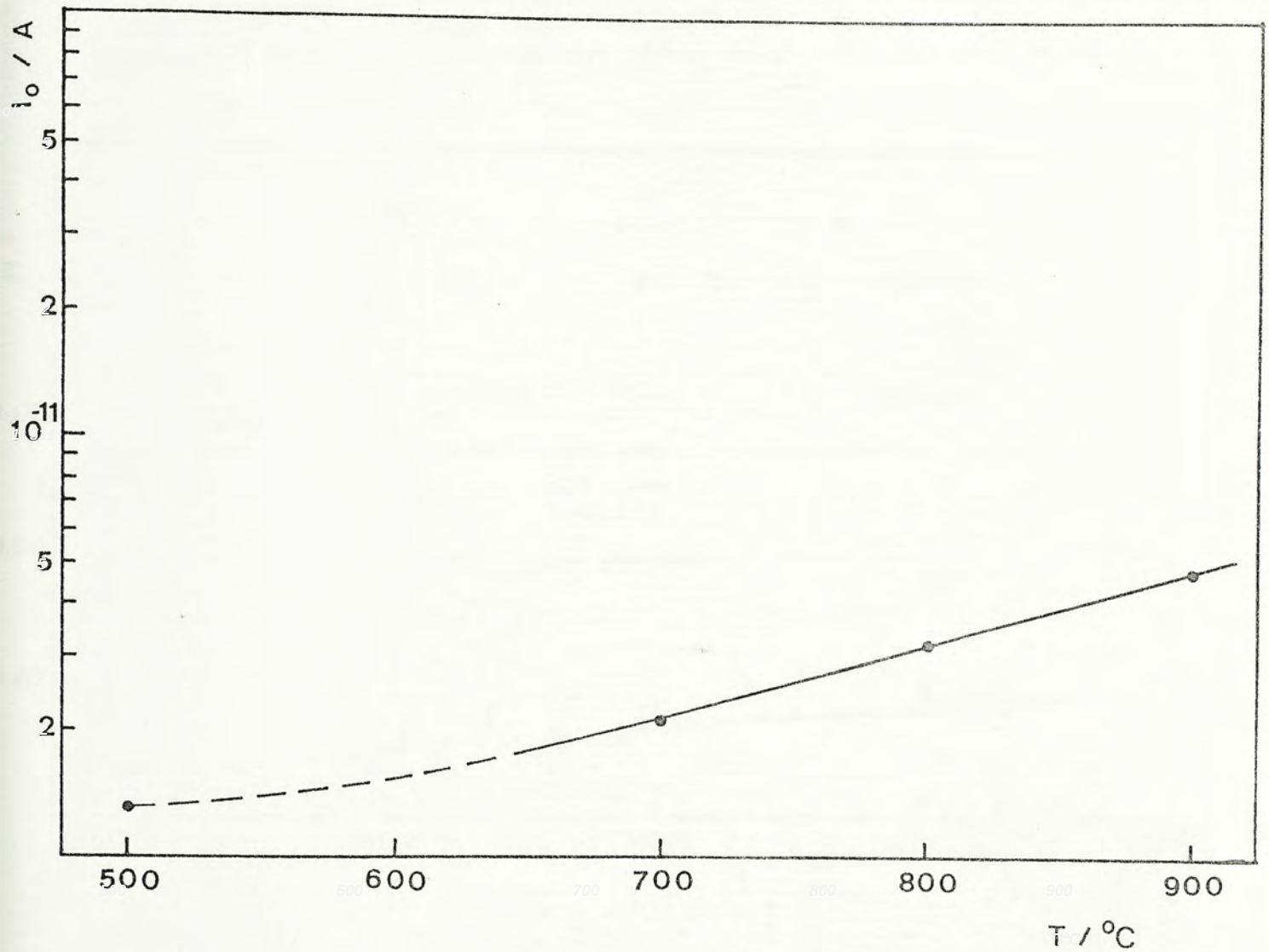

Fig. 3.7 Saturation current versus heat treatment temperature.

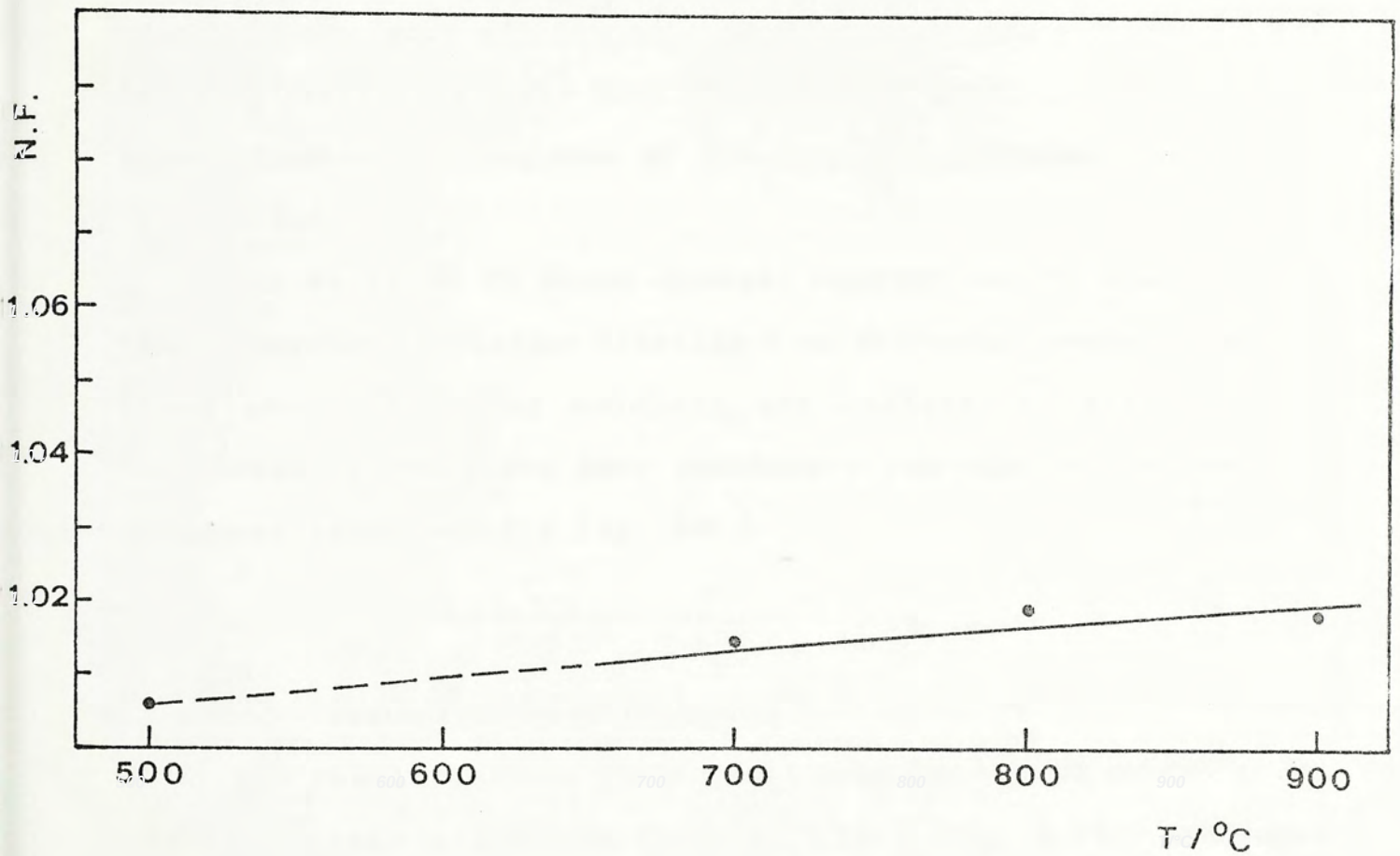

Fig. 3.8 Ideality factor versus heat treatment temperature.

after heat treatment which corresponds to a $I_{od} = 1.4 \times 10^{-12}$ A/cm^2. This value is substantially lower than the saturation current measured. This suggests that the increases in the saturation current and the ideality factor are not only due to the bulk lifetime degradation but also due to other effects such as recombination in space charge region and surface states. Furthermore, such effects are temperature dependent. The poorer surface properties after heat treatment is supported by the lower short wavelength response of the spectral response measurement (Fig. 3.9).

The decrease in short circuit current can be explained by the reduction of carrier lifetime (or diffusion length) so that less photo-generated carriers are collected. This is also supported by the lower long wavelength response of the spectral response measurement (Fig. 3.9).

3.4.2 Isothermal heat treatment

The results of the isothermal heat treatment at 800°C for various times are shown in Fig. 3.10 - Fig. 3.16. The open circuit voltage, short circuit current , fill factor and total area efficiency (Fig. 3.10 - Fig. 3.13) decrease steadily as heat treatment time increases. Fig. 3.14 and Fig. 3.15 show that the saturation current and the ideality factor increase as heat treatment time increases. The minority lifetime (Fig. 3.16) shows a slight decrease with some variations.

The general trend is similar to that observed in the

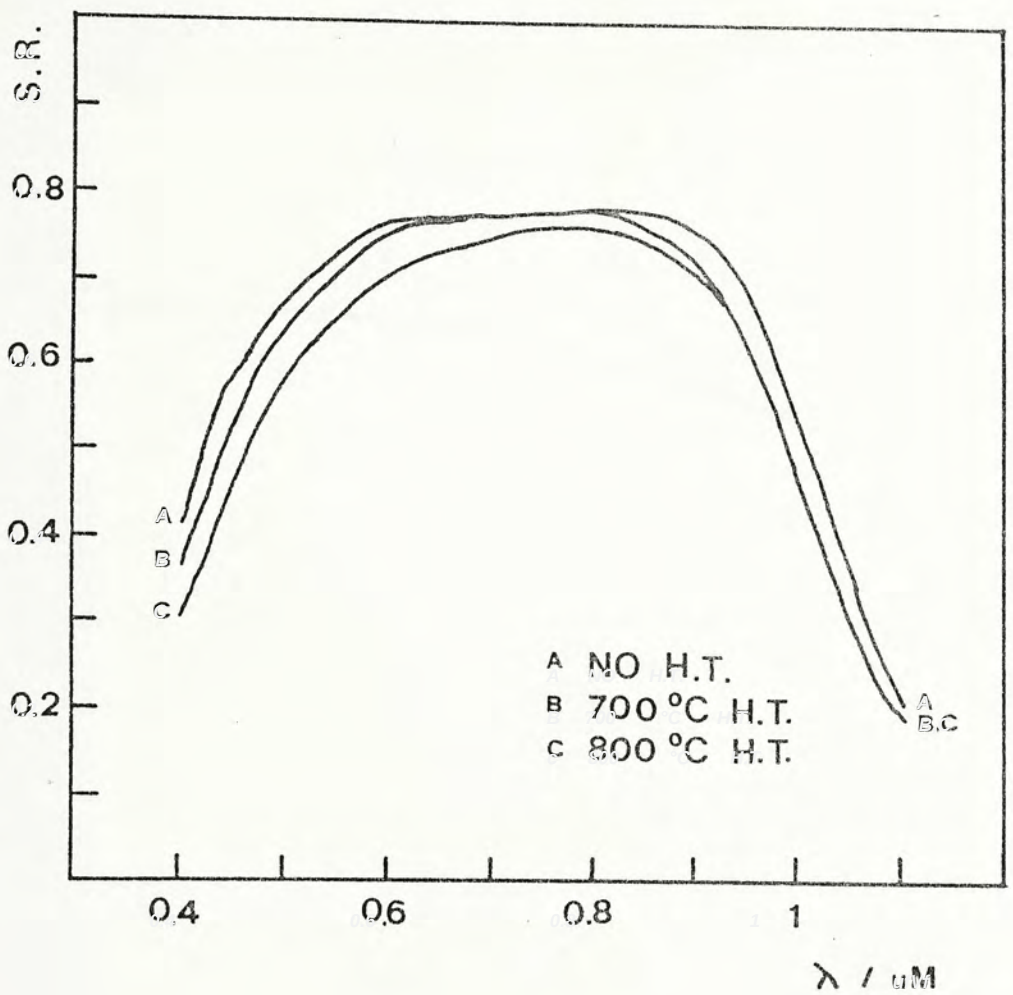

Fig. 3.9 Spectral responses for various heat treatment temperature.

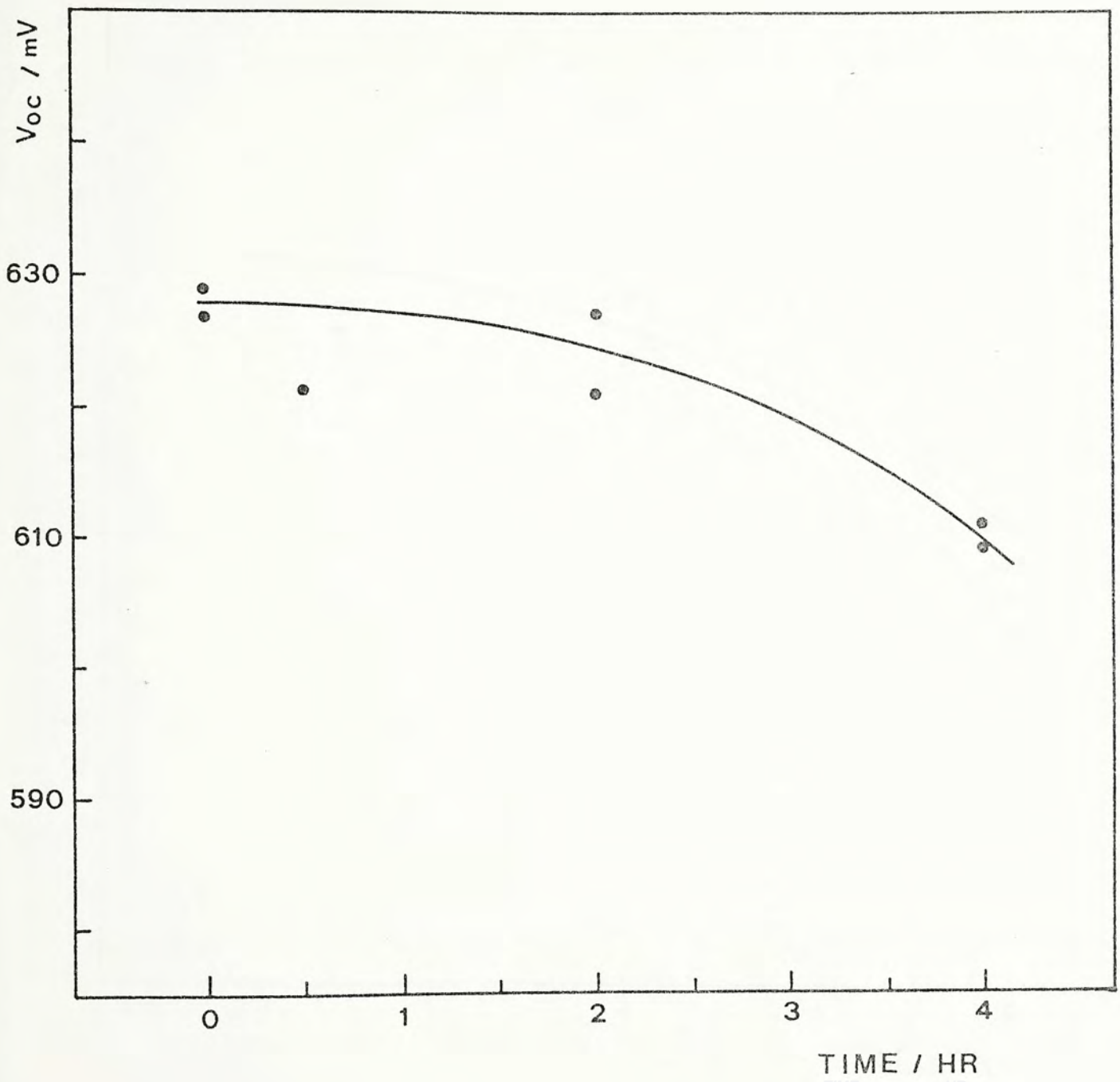

Fig. 3.10 Open circuit voltage versus heat treatment time at 800 °C.

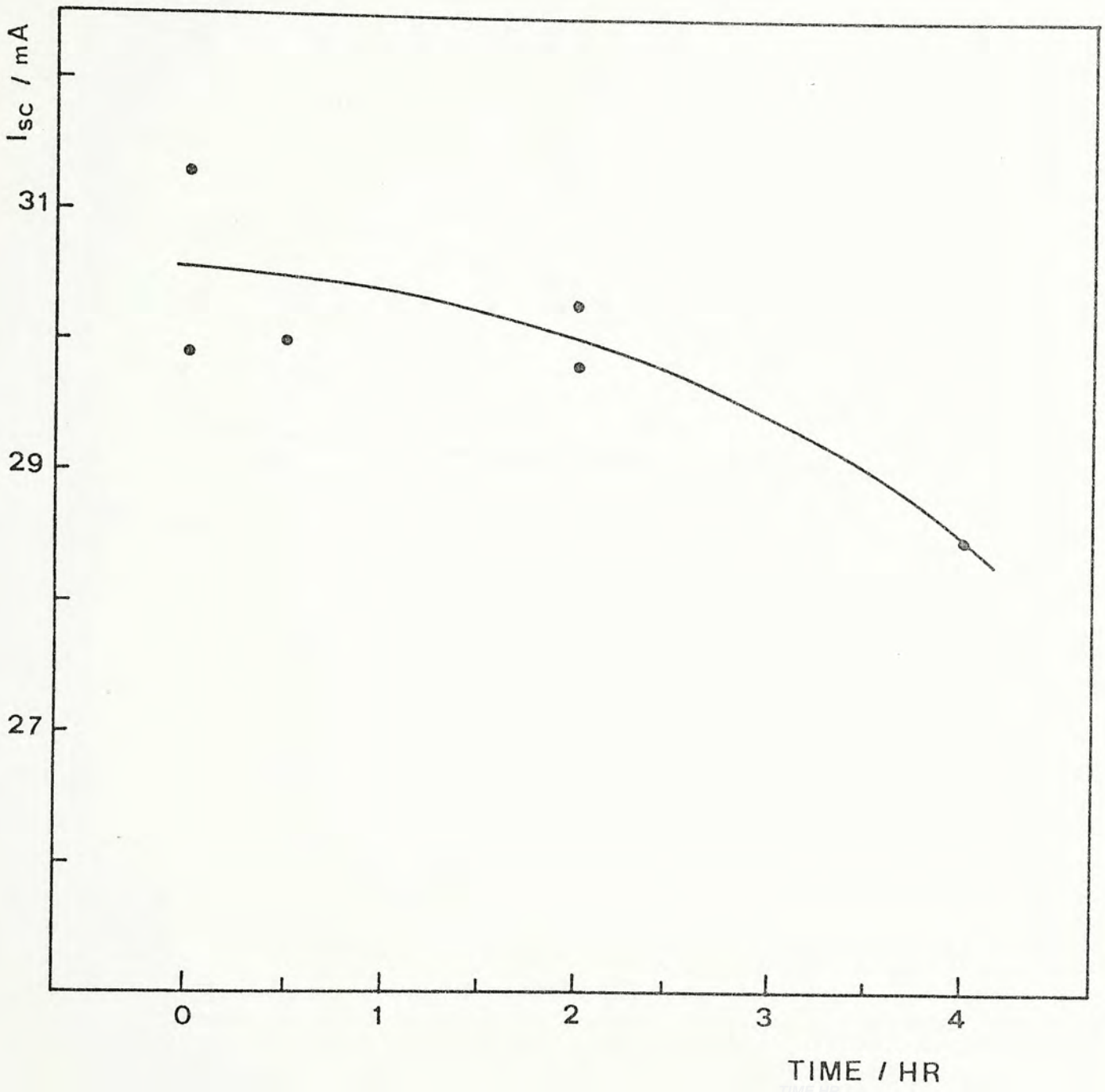

Fig. 3.11 Short circuit current versus heat treatment time at 800 °C.

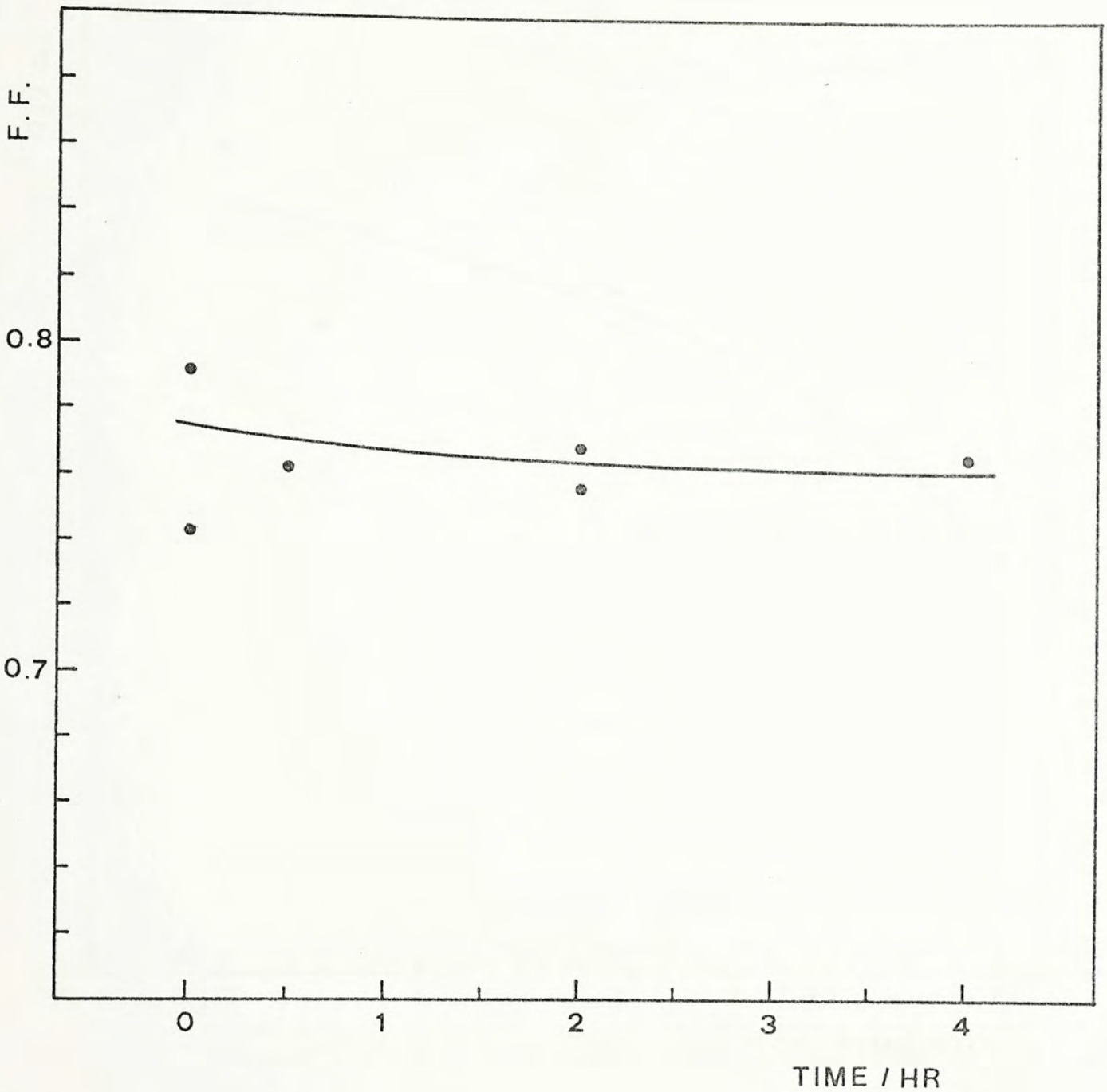

Fig. 3.12 Fill factor versus heat treatment time at 800 °C.

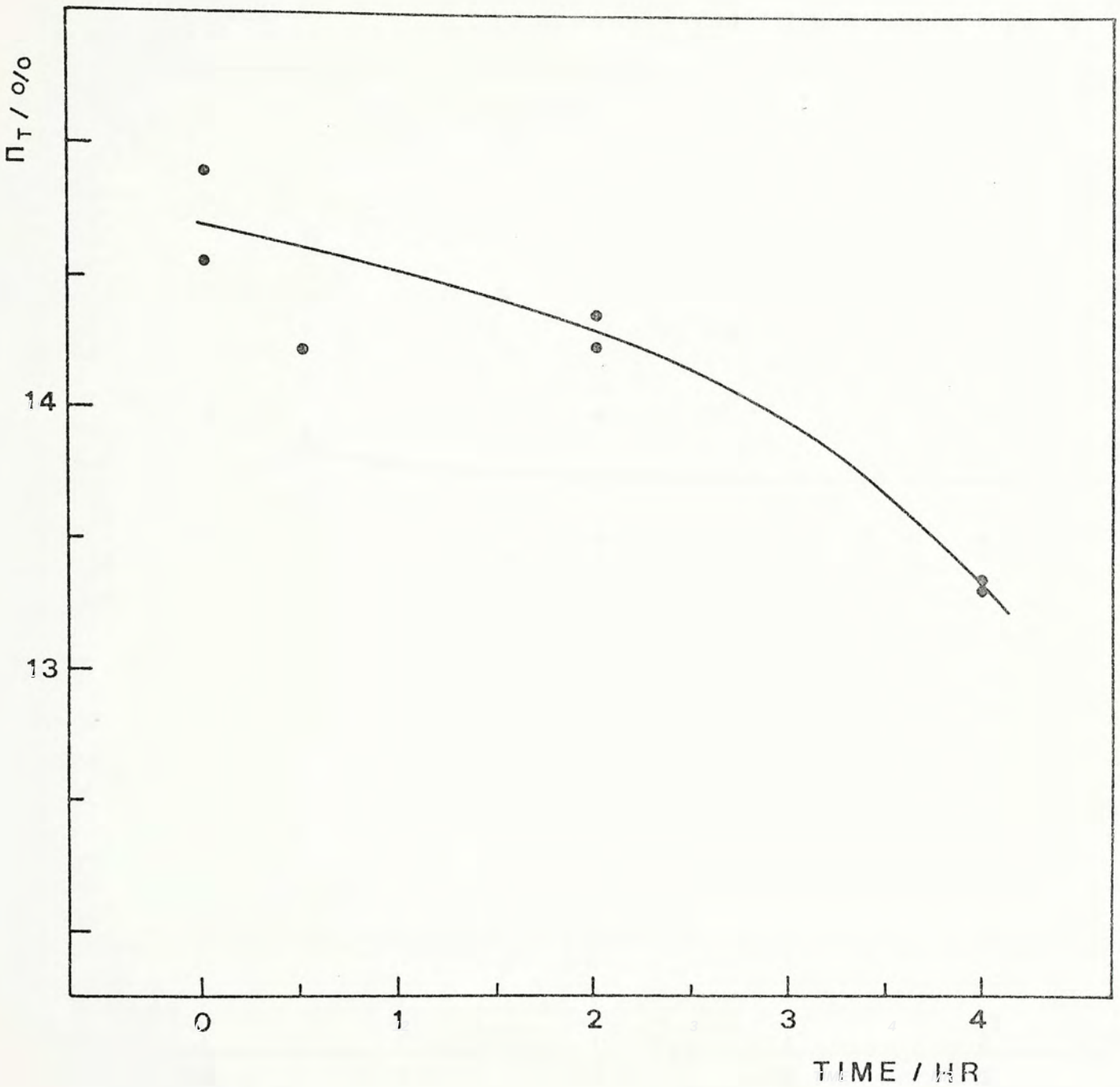

Fig. 3.13 Total area efficiency versus heat treatment time at 800 °

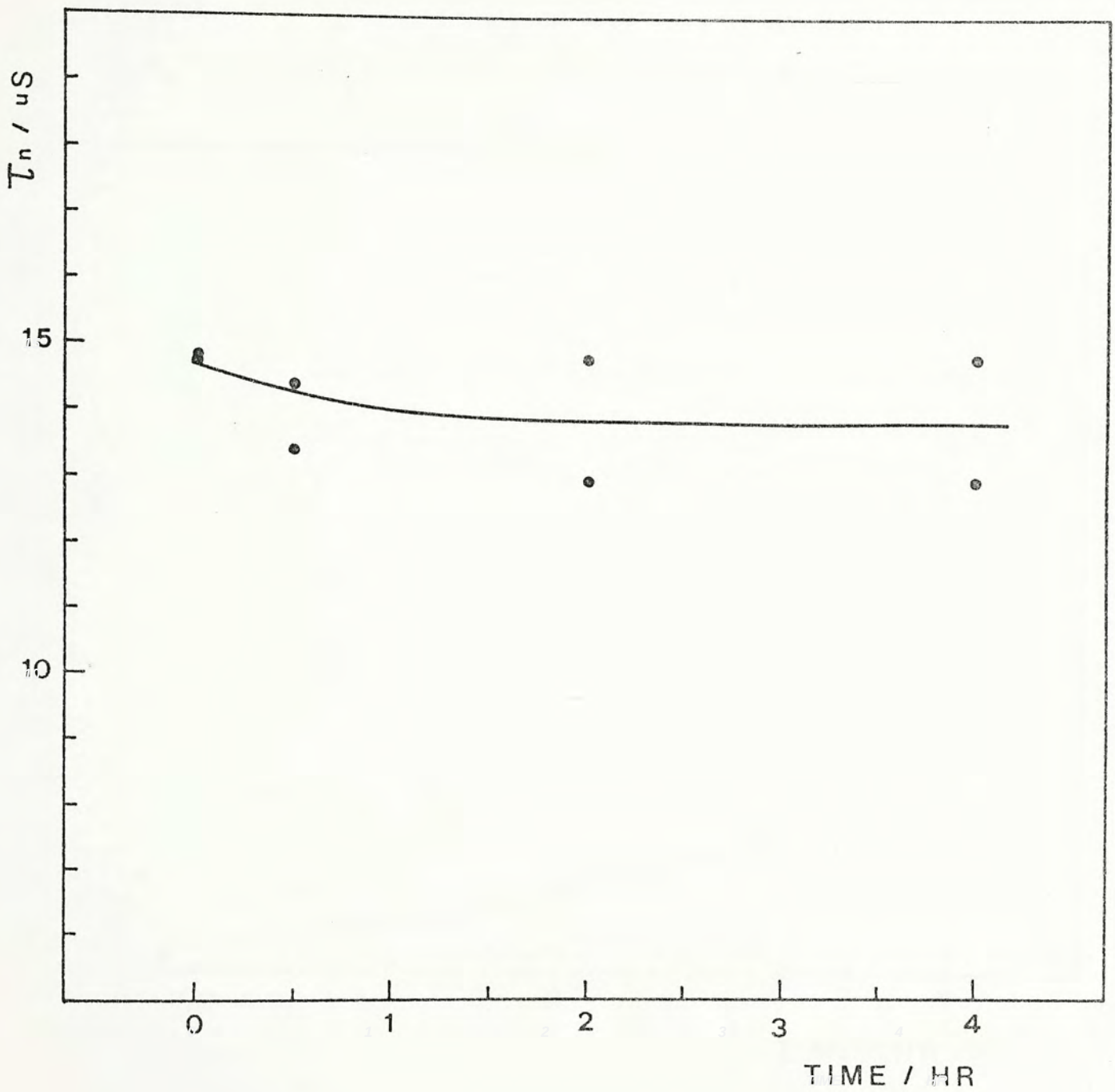

Fig. 3.14 Minority carrier lifetime versus heat treatment time at 800 °C.

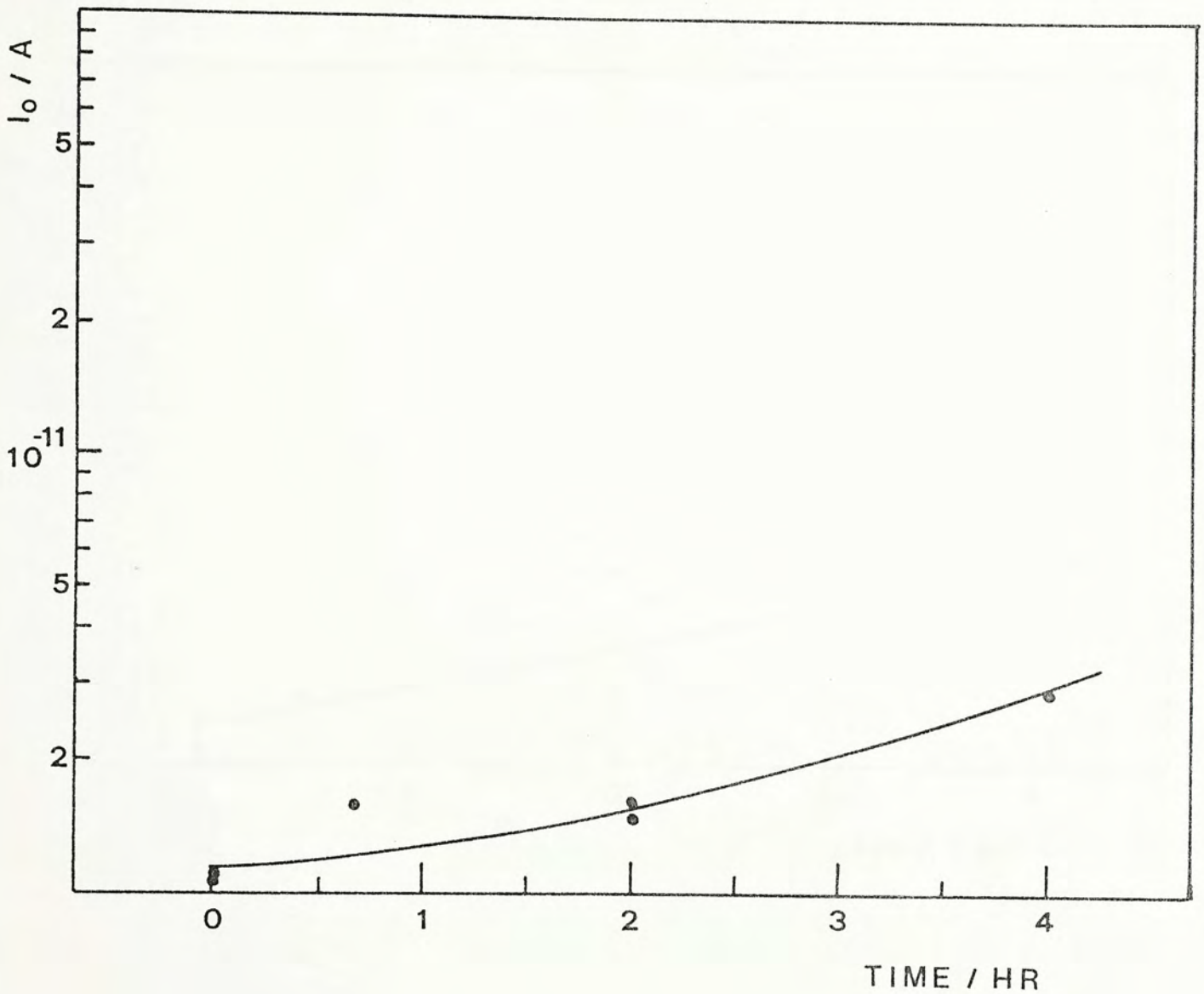

Fig. 3.15 Saturation current versus heat treatment time at 800 °C.

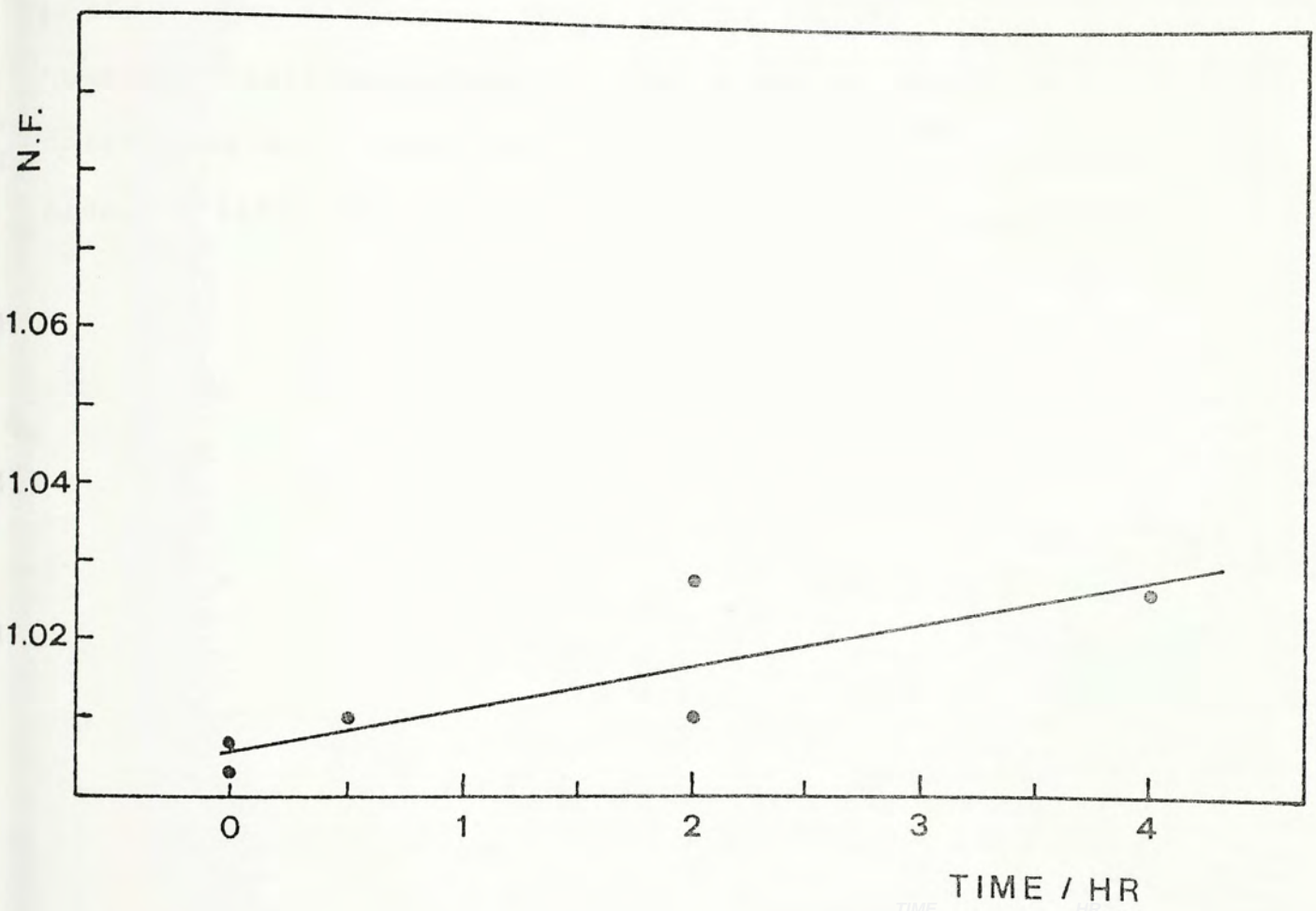

Fig. 3.16 Ideality factor versus heat treatment time at 800 °C.

isochronal heat treatment. Discussion in section 3.4.1 thus also applies here. Note that the percentage degradation in the isothermal heat treatment is larger than in the isochronal heat treatment.

The results in the isothermal heat treatment are consistent with Kalejs and Ladd [3] who observed degradation in cell performance after heat treament at 1200^{o}C for 10 and 60 min. However, their measurements were based on diffused p-n junction solarcells such that the diffusion effect has not been isolated. Also, no lifetime and spectral response measurement were reported.

3.5 Conclusions

Effects of isochronal and isothermal heat treatment on MIS grating solar cells are studied in detail. Degradation in cell performance against temperature and time is observed. The degradation which is solely due to high temperature heat treatment in the range of practical interest is reported for the first time.

An irreversible degradation in lifetime is observed. The degradation in cell performance can be partly explained by the lifetime degradation. Calculation shows that the increase in the saturation current due to the lifetime degradation is substantially less than the measured value. This suggests that an enhanced recombination current component results after heat treatment at the surface due to effects such as recombination in space charge region and surface states. The short and long wavelength degradation in spectral response supports the above intepretation.

The result of this study suggests that higher efficiency solar cell results from lower temperature and shorter time used to obtain the required doping and annealing.

References

[1] H. Fischer and W. Pschunder, "Impact of material and junction properties on silicon cell efficiency," 11th IEEE Photov. Spec. Conf., p.25, 1975.

[2] K. Graff, H. Pieper and G. Goldbach, "Carrier lifetime doping of p type silicon by annealing processes," Semiconductor Silicon, p.170, 1973.

[3] J.P. Kalejs and L.A. Ladd, "Influence of high temperature annealing on performance of edge-defined film-fed growth silicon ribbon solar cells," Appl. Phys. Lett., Vol. 45, p.540, 1984.

[4] K.K. Ng and H.C. Card, "A Comparison of majority and minority carrier silicon solar cells," IEEE Trans. Ele. Dev., Vol. 27, p.716, 1980.

[5] C.S. Hoi, "Studies of the electrical characteristics of MIS/MINP solar cells," M. Phil. thesis, CUHK, 1983.

[6] H.C. Card and E.H. Rhoderick, "Studies of tunnel MOS diodes I. interface effects in silicon Schottky diodes," J. Phys. D. Appl. Phys., Vol. 4, p.1589, 1971.

H.C. Card and E.H. Rhoderick, "Studies of tunnel MOS diodes II. thermal equilibrium considerations," J. Phys. D. Appl. Phys., Vol. 4, p.1602, 1971.

[7] L.B. Freeman and W.E. Dahlke, " Theory of tunneling into interface states," Solid State Ele., vol. 13, p.1483, 1970.

[8] S.M. Sze, Physics of Semiconductor Devices, 2/e., New York, Wiley, 1981.

[9] J. Fossum and D.S. Lee, "Significance of low temperature

processing in the fabrication of silicon solar cells," 15th IEEE Photov. Spec. Conf., p.120, 1981.

[10] W. Shockley and W.T. Read, "Statistics of the recombination of holes and electrons," Phys. Rev., Vol. 87, p.835, 1952.
R.H. Hall, "Electron hole recombination in Germanium," Phys. Rev., Vol. 87, p.387, 1952.

[11] J.G. Fossum, "Computer-aided numerical analysis of silicon solar cells," Solid State Ele., Vol. 19, p.269, 1976.

[12] D.L. Pulfrey, "MIS solar cells : a review," IEEE Trans. Ele. Dev., vol. 25, p.1308, 1978.

[13] M.C. Poon, "Experimental studies of Mg-MIS inversionn layer grating solar cells," M. Phil. thesis, CUHK, 1983.

[14] D.S Comporese, T.P. Lester and D.L. Pulfrey, "A fine line silicon shadow mask for inversion layer solar cells," IEEE Ele. Dev. Lett., Vol. 2, p.61, 1981.
D.S. Comporese, T.P. Lester and D.L. Pulfrey, "Development of fine line silicon shadow masks for deposition for solar cell grids," 15th IEEE Photov. Spec. Conf., p.527, 1981.

[15] H.B. Nguyen, "A proposed slotted mask for direct deposition of direct deposition of metal contact pattern on MIS solar cells," IEEE Trans. Ele. Dev., p.1303, 1980.

[16] P.A. Iles, "Antireflection coatings for solar cells," J. Vac. Sci. Tech., Vol. 14, p.1000, 1977.

[17] G. Hass and C.D. Salzberg, "Optical properties of silicon monoxide in the wavelength region from 0.24 to 14 microns," J. Optical Soc. Amer., Vol. 44, p.181, 1954.

[18] H.R. Philips, "Optical properties of non-crystalline Si,

SiO, SiO_x and SiO_2," J. Phys. Chem. Solids, Vol. 32, p.1935, 1971.

[19] Y.W. Lam, "A solar cell characteristics plotter," J. Phys. E : Sci. Instrum., Vol. 14, p.1302, 1981.

[20] P. Panayotatos and H.C. Card, "Use of V_{oc}/J_{sc} measurements for determination of barrier height under illumination and fill factor calculations in Schottky barrier solar cells," IEE Proc., Vol. 127, Pt. I, p.308, 1980.

[21] J.E. Mahan, "Measurement of minority carrier lifetime in solar cells from photo-induced open circuit voltage decay," IEEE Trans. Ele. Dev., Vol. 26, p.733, 1979.

[22] S.C. Jain, "Theory of photo-induced open circuit voltage decay in a solar cell," Solid State Ele., vol. 24, p.179, 1981.

[23] S.R. Dhariwal and N.K. Vasu, "Mathematic formulation for the photo-induced open circuit voltage decay method for measurement of minority carrier lifetime in solar cells," IEEE Ele. Dev. Lett., Vol. 2, p.53, 1981.

4. ION IMPLANTED MINP SOLAR CELLS

4.1 Introduction

Doping using ion implantation offers several advantages. It allows accurate control of ion dose, depth and uniformity which are essential especially for the low dose, shallow junction. It is a high throughput, dry, vacuum process and is suitable for automation. In addition, no back surface etching is needed as in the diffusion process.

However, an annealing step is required to activate the dopant atoms and to reduce damages caused by the implantation. Unactivated dopants and residual damages may act as recombination centres which increase the saturation current and lower the carrier lif etime. Undesirable broadening of the doping profile may also be caused by high temperature annealing.

The annealing behavior of phosphorus implant at energies 100 KeV and 150 KeV at a dose level of 2×10^{15} cm^{-2} on (100) and (111) 1 ohm-cm substrates through thermally grown SiO_2 (0.1 and 0.15 um) which also act as antireflection coating has been investigated by Zignani et al. [1]. They found that the electrical activity in (100) samples was about complete after annealing at 550°C whereas about 700°C annealing was neeeded for the (111) samples. Radiation damage has been studied by proton back scattering and transmission electron microscopy. The optimum annealing was concluded as 750°C 30 min because higher temperature annealing didnot significantly improve the implanted layers' electrical characteristics and didnot remove the residual

damage while it lowered the bulk lifetime.

Multiple step thermal annealing has been developed at Spire [2] as follows:

550°C	120 min	in N_2
850°C	15 min	in N_2
550°C	120 min	in N_2

The initial low temperature step causes effective epitaxial regrowth of damaged silicon lattice while the 850°C step activates the implanted dopants electrically. The final low temperature step is for lifetime enhancement.

Modified procedures which utilize an oxidizing ambient were found to produce higher open circuit voltage in cells of low resistivity silicon due to better surface passivation [3].

In addition to thermal annealing process, transient annealing process such as electron beam and laser annealing has also been investigated [5,6]. Defects in the near surface region such as the "dead layer" produced by conventional high temperature diffusion can be completely removed by laser irradiation [7].

A systematic study on the implant parameters (dose, energy ion species) and annealing techniques has been conducted by Douglas and D'aiello [8,9]. They showed that the three step annealing process and the backside boron-glass gettering procedure were capable of preserving or increasing the diffusion

length in the bulk region of the wafer. The optimum dose level was found to be $2x10^{15}$ - $5x10^{15}$ cm^{-2} with efficiency of 14 - 15 % at AM1 in the dose range studied ($2x10^{14}$ - 10^{16} cm^{-2}).

High dose ion implantation described above is primarily an alternative to diffusion in junction formation in conventional p-n junction colar cells. However, low dose ion implantation can be used to control the surface properties as discussed in chapter 2.

Ponpon and Siffert [10] have shown that the efficiency of their Schottky barrier solar cells increased by about 50 % by use of ion implantation at low dose.

Increase in open circuit voltage of Schottky barrier solar cells have also been observed by Pai et al. [11,12] using low dosage ion implantation.

Blakers et al. [13] have obtained open circuit voltage as high as 661 mV at AM0 on 0.1 ohm-cm substrate at dosage levels of 10^{13} and 10^{14} cm^{-2} of 20 KeV phosphorus ions. The implant dose of this MINP structure was 20 - 200 times lower than the conventional ion implanted solar cells. This makes ion implantation cost competitive to the diffusion process [14].

No detailed study has yet been made in low dose ion implantation MINP solar cell. This is the topic of the present chapter.

4.2 Experimentals

The implant parameters (dose, energy) and annealing conditions were systematically studied. The implant dose (phosphorus) ranged from 10^{12} to 10^{15} cm^{-2} while ion energies of 20 KeV and 30 KeV were used. Anneals were carried out in nitrogen ambient. Single step and three step annealing were employed with details indicated in Table 4.1.

Table 4.1

single step annealing	three step annealing	
	550°C	120 min
T 15 min	T	15 min
	550°C	120 min
$600^{\circ}C \leq T \leq 900^{\circ}C$		

Temperature as low as 600°C was included since low temperature annealing was essential to solar cell fabrication.

Implants through thin thermal oxide grown at 800°C for 30 min in dry oxygen were also investigated.

The implant and annealing conditions are summarized in Table 4.2.

The as implanted profile parameters [15] are tabulated in Table 4.3.

There are a little impurity redistribution in high temperature anneals.

Table 4.2

set	implant	annealing
A	20 KeV	single step
B	20 KeV	three step
C	30 KeV	three step
D	30 KeV through oxide	three step

The annealed implant samples were then subjected to normal MIS fabrication procedure as described in section 3.3.2. The front grid evaporation was carried out using a 51 fingers/cm silicon mask.

Measurement were taken as described in section 3.3.3.

Table 4.3

Energy / KeV	20				
Dose / cm^{-2}	10^{12}	10^{13}	$5x10^{13}$	10^{14}	10^{15}
N_{max} / cm^{-3}	$4.3x10^{17}$	$4.3x10^{18}$	$2.1x10^{19}$	$4.3x10^{19}$	$4.3x10^{20}$
x_j / A	476	556	601	618	671
$\overline{N}$ / cm^{-3}	$2.1x10^{17}$	$1.8x10^{18}$	$8.3x10^{18}$	$1.6x10^{19}$	$1.5x10^{20}$
Energy / KeV	30				
Dose / cm^{-2}	10^{12}	10^{13}	$5x10^{13}$	10^{14}	10^{15}
N_{max} / cm^{-3}	$3.1x10^{17}$	$3.1x10^{18}$	$1.5x10^{19}$	$3.1x10^{19}$	$3.1x10^{20}$
x_j / A	655	771	834	859	934
$\overline{N}$ / cm^{-3}	$1.5x10^{17}$	$1.3x10^{18}$	$6.0x10^{18}$	$1.2x10^{19}$	$1.1x10^{20}$
Energy / KeV	30 (through oxide)				
Dose / cm^{-2}	10^{12}	10^{13}	$5x10^{13}$	10^{14}	10^{15}
N_{max} / cm^{-3}	$3.1x10^{17}$	$3.1x10^{18}$	$1.6x10^{19}$	$3.1x10^{19}$	$3.1x10^{20}$
x_j / A	573	690	753	778	853
$\overline{N}$ / cm^{-3}	$1.8x10^{17}$	$1.5x10^{18}$	$6.6x10^{18}$	$1.3x10^{19}$	$1.2x10^{20}$

4.3 Results and Discussion

4.3.1 Set A - 20 KeV implant, single step annealing

Cell peformance measured under AM1.5 illumination is shown in Fig. 4.1 - Fig. 4.4.

As shown in Fig. 4.1, high open circuit voltages are attained after 800°C anneals. 700°C and 900°C annealed samples show a gradual decrease in open circuit voltage as the surface doping dose increases.

The interesting dip for the 600°C annealed samples can be explained by insufficient anneal. When the dosage is low, the residual damage and unactivated dopants are small in quantity so that their effects are small. When the dosage is high, an amorphous layer is formed which facilitates recrystallization and activation at lower temperature. There exists a intermediate dosage at which the effect of insufficient anneal is most prominent. The lowest open circuit voltage was found at a medium dosage of 10^{13} cm^{-2}.

The low open circuit voltage of heavily doped MINP (10^{15} cm^{-2}) is in agreement with Green et al. [16].

Shown in Fig. 4.2 are the short circuit currents under various doses with annealing temperature as a parameter. All samples under various anneals show a general increase in short circuit current as dose level increases which are attributed to a lowerseries resistance in the surface layer as dose level increases (also see Fig. 2.8). For a particular dose level, higher short circuit current is obtained at lower annealing

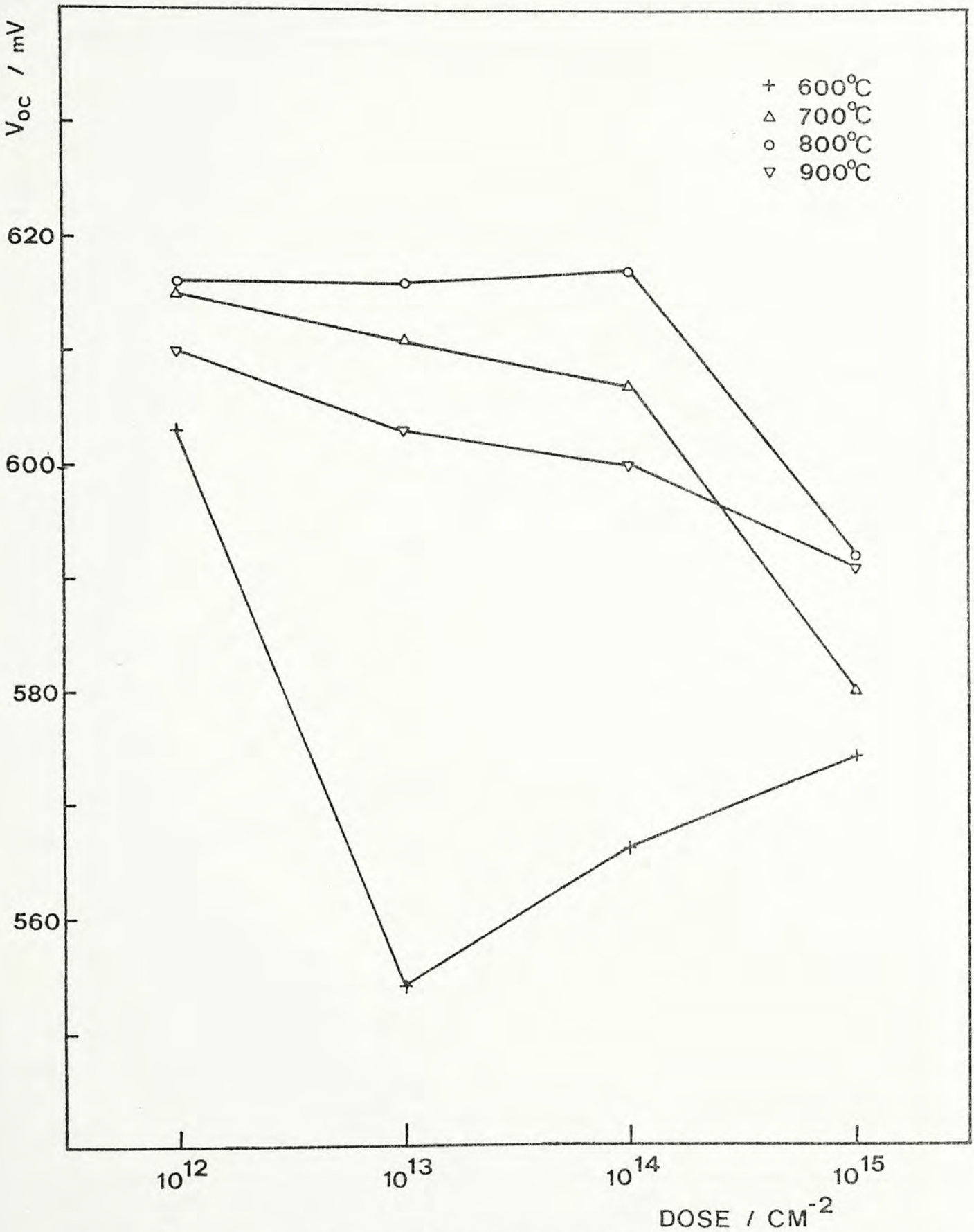

Fig. 4.1 Open circuit voltage versus dose for various annealing temperatures. (set A - 20 KeV implant, single step annealing)

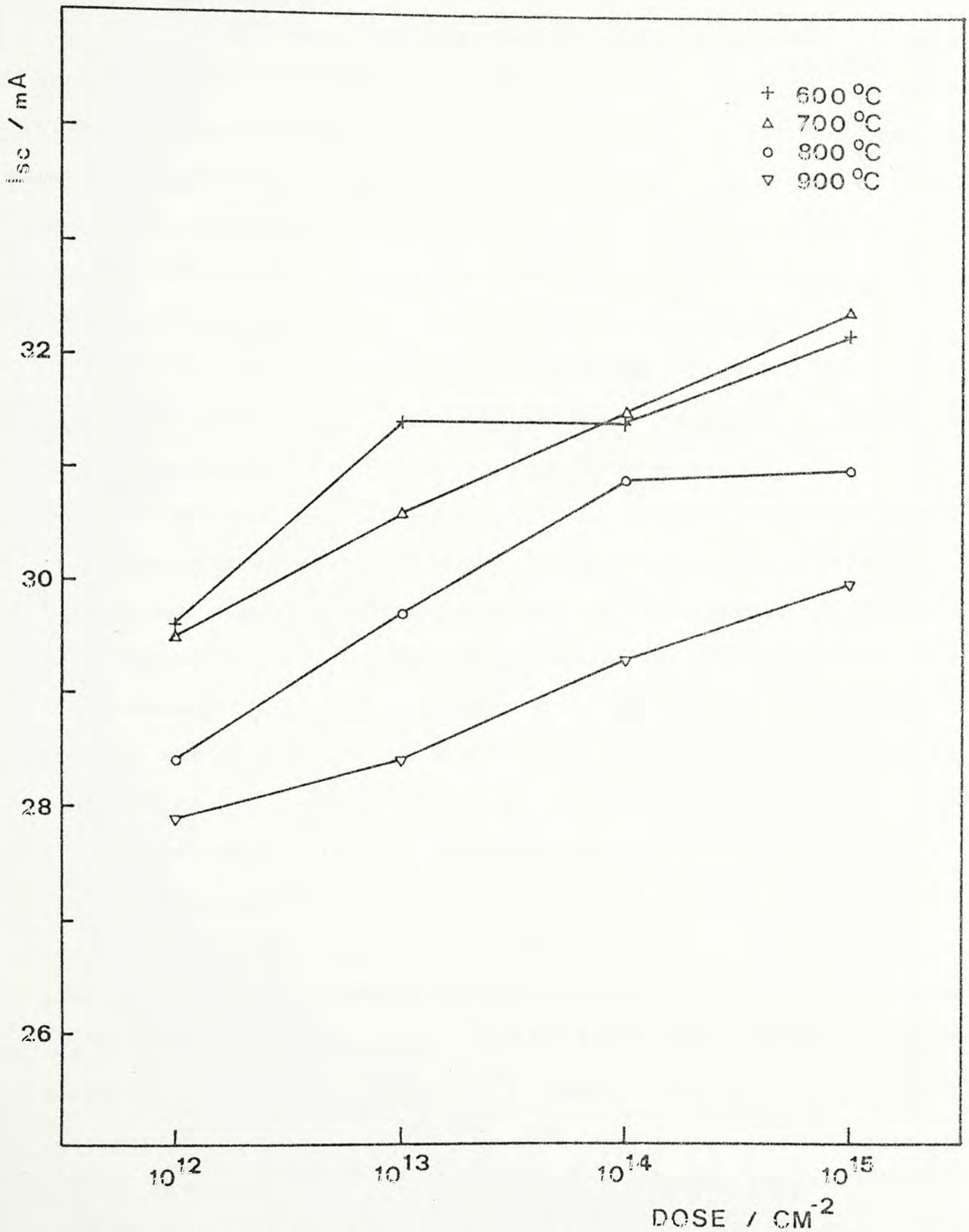

Fig. 4.2 Short circuit current versus dose for various annealing temperatures. (set A - 20 KeV implant, single step annealing)

temperature. This is consistent with the result obtained in heat treated MIS solar cells (Fig. 3.4).

Fig. 4.3 shows that the fill factor of various anneals starts to fall at dose level of 10^{14} cm^{-2}. This is due to a higher recombination current component in the depletion region which has an ideality factor of 2 at higher dose level. It will be discussed in more detail later.

The efficiency at AM1.5 is shown in Fig. 4.4. The 700°C - 900°C annealed samples show an optimum dose around 10^{13} cm^{-2} - 10^{14} cm^{-2}. The "anomalous" behavior of the 600°C annealed samples is due to the cause as for their behavior in the open circuit voltage (Fig. 4.1), as explained above.

The optimum annealing condition of the ion implanted solar cells are determined by two incompatible mechanisms. Activating dopants and removing damage require high temperature on one hand while perserving carrier lifetime demands low temperature on the other hand. In this set of experiments, 800°C, 15 min anneal attains the highest efficiency which is consistent with that reported in [1] (750°C, 30 min).

The minority carrier lifetime shown in Fig. 4.5 indicates that the degradation in carrier lifetime is dominated by the dose level. Low annealing temperature (600°C) has marginal advantage over high annealing temperature (700°C - 900°C) while 700°C - 900°C anneals show little difference due to partial recovery of lifetime during 500°C back contact sintering (also see section 3.4.1).

A detailed look at the current voltage characteristic reveals that there is about two to three orders of magnitude

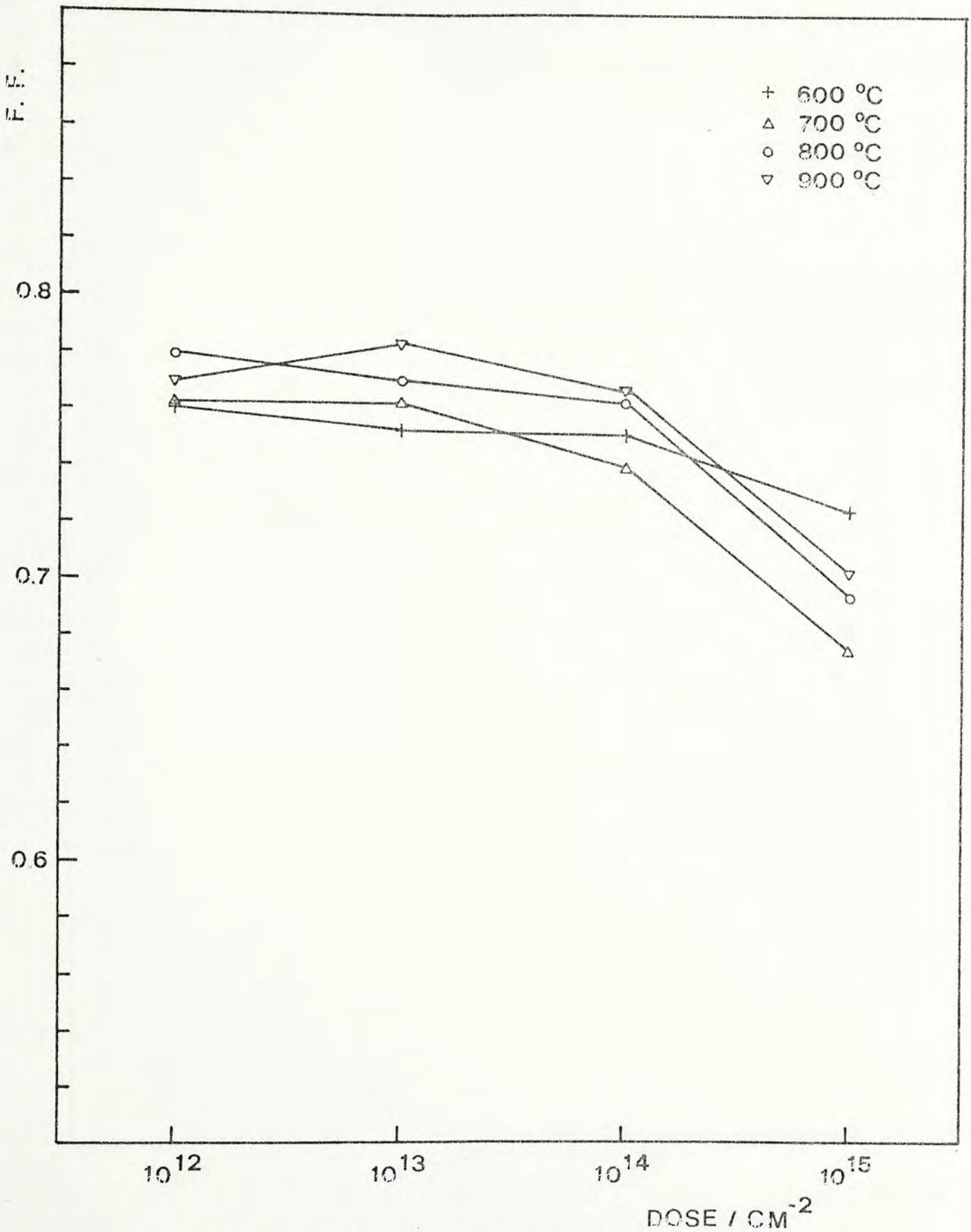

Fig. 4.3 Fill factor versus dose for various annealing temperatures. (set A - 20 KeV implant, single step annealing)

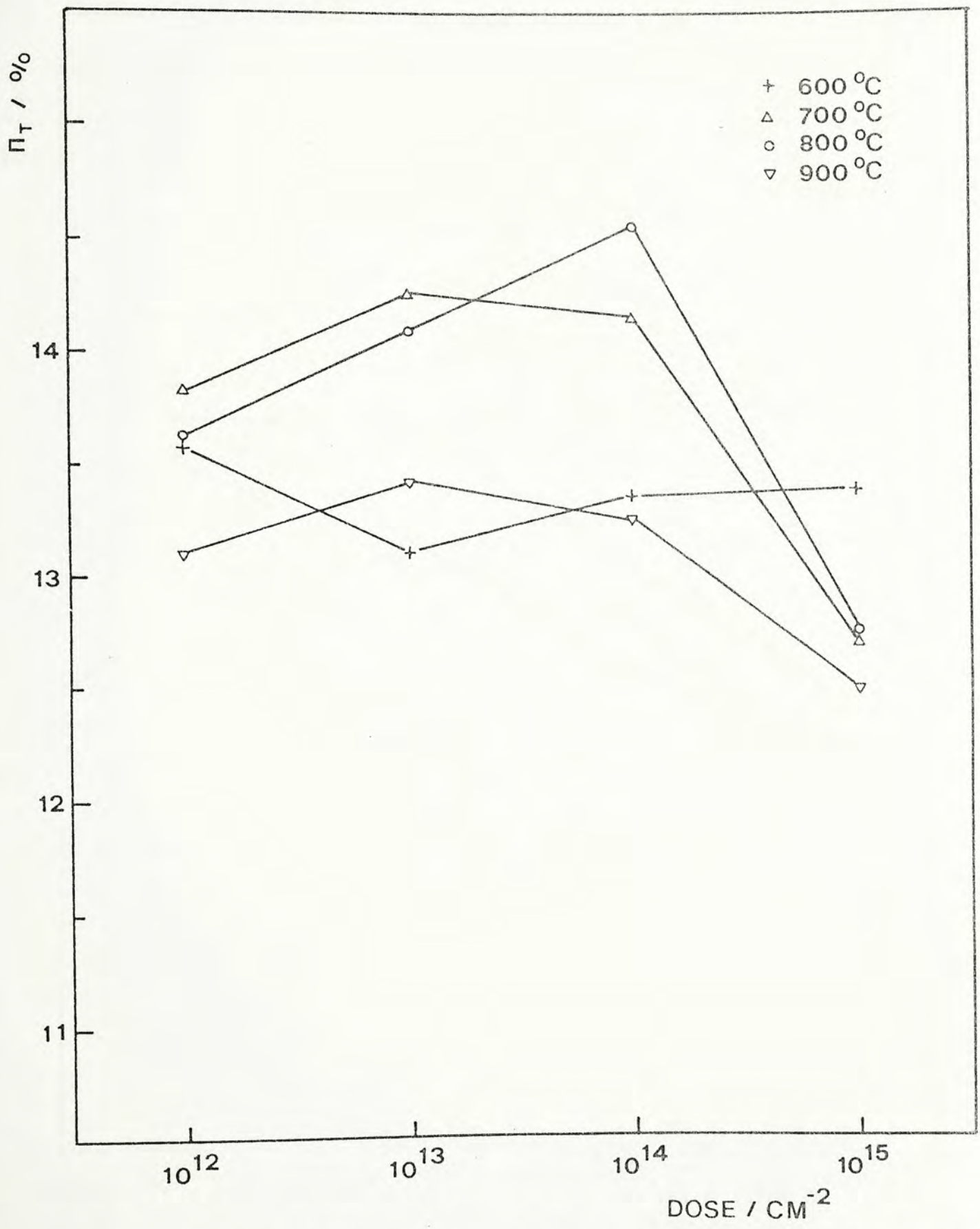

Fig. 4.4 Total area efficiency versus dose for various annealing temperatures. (set A - 20 KeV implant, single step annealing)

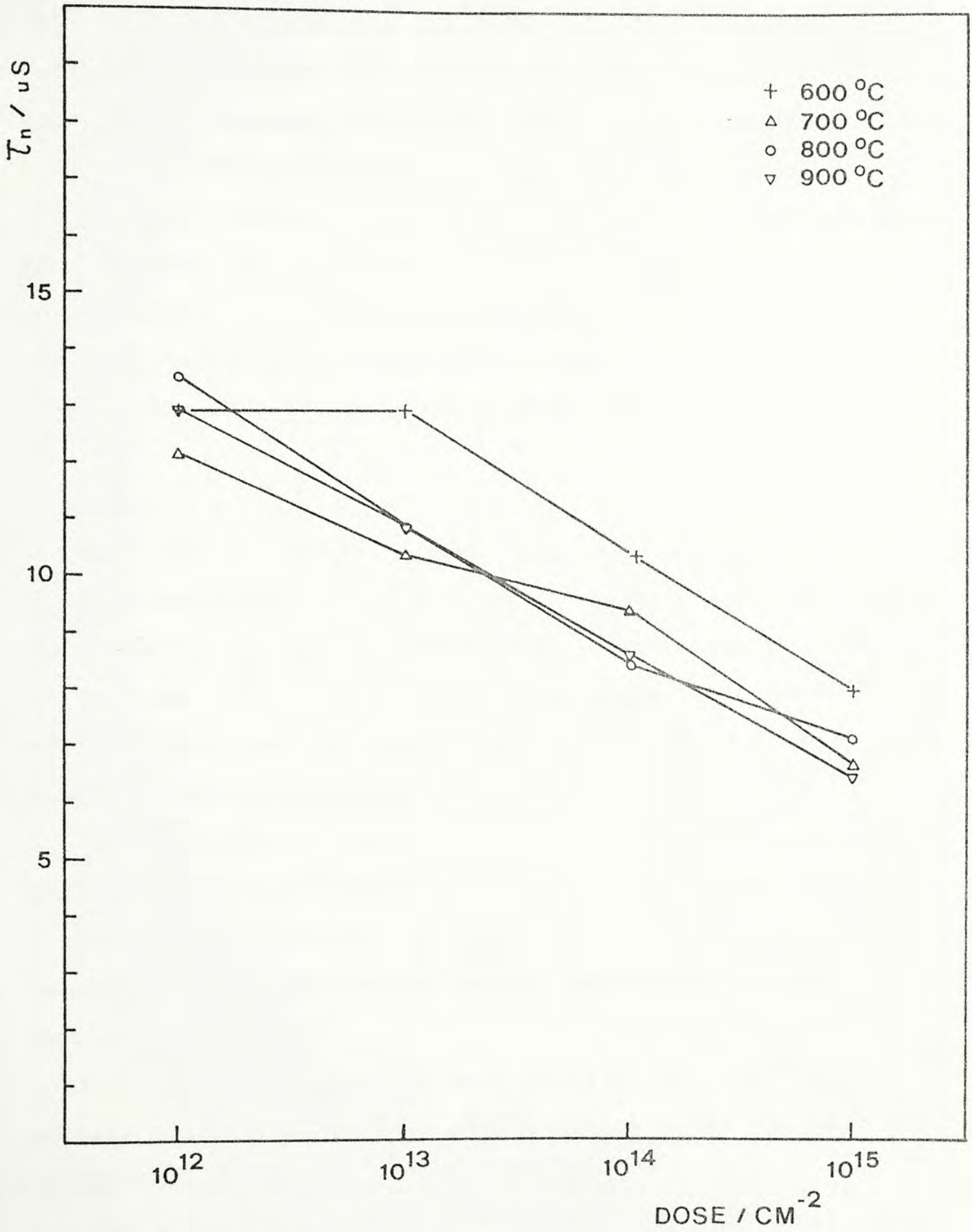

Fig. 4.5 Minority carrier lifetime versus dose for various annealing temperatures. (set A - 20 KeV implant, single step annealing)

increase in the saturation current from dose level 10^{12} cm^{-2} to 10^{15} cm^{-2} as shown in Fig. 4.6. The increase in the saturation current with the dose level also helps to explain the decrease in open circuit voltage (Fig. 4.1). Insufficient anneal at 600°C - 700°C is also revealed at dose level 10^{12} cm^{-2} - 10^{14} cm^{-2}.

Fig. 4.7 shows the ideality factor against various dose. The ideality factor increases with the dose level. This is consistent with the calculation shown in Fig. 2.5. A high ideality factor that soften the current voltage characteristic degrades the fill factor as observed in Fig. 4.3.

4.3.2 Set B - 20 KeV implant, three step annealing

The results of 20 KeV implant, three step annealed samples are shown in Fig. 4.8 - Fig. 4.14. The results are qualitatively the same as in set A (20 KeV implant, single step annealing) so that no detailed discussion will be given. However, the following points are noted.

1. The open circuit voltage (Fig. 4.8) of samples annealed at 800°C and 900°C are higher than those in set A (Fig. 4.1).
2. The larger variation in short circuit current (Fig. 4.9) is attributed to the relaxed control over antireflection coating during process.
3. The fill factor peaks at dose level of $10^{13}cm^{-2}$ and starts to fall down (Fig. 4.10). 800°C anneal gives the best fill factor.
4. The efficiency (Fig. 4.11) peaks at dose level around

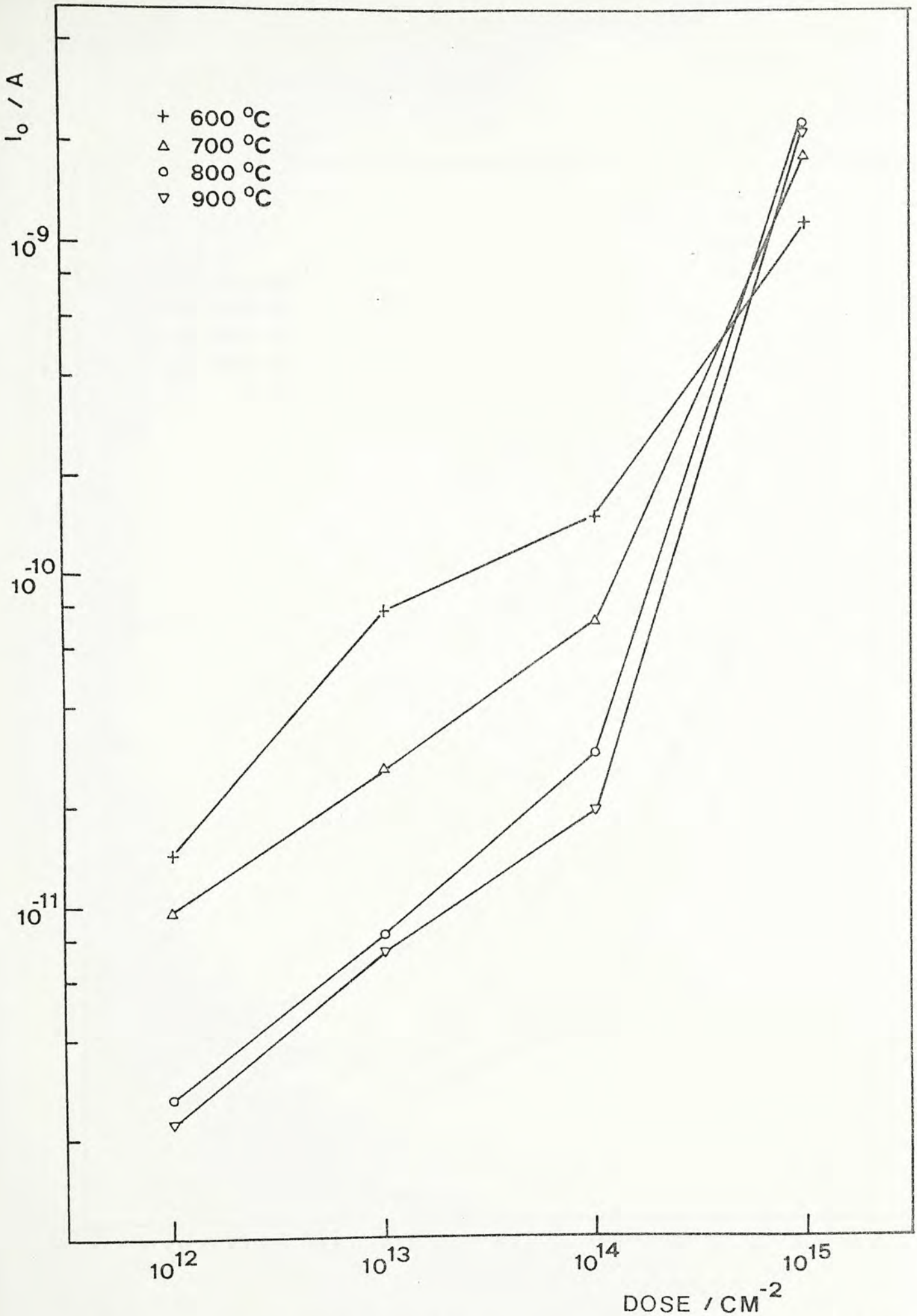

Fig. 4.6 Saturation current versus dose for various annealing temperatures. (set A - 20 KeV implant, single step annealing)

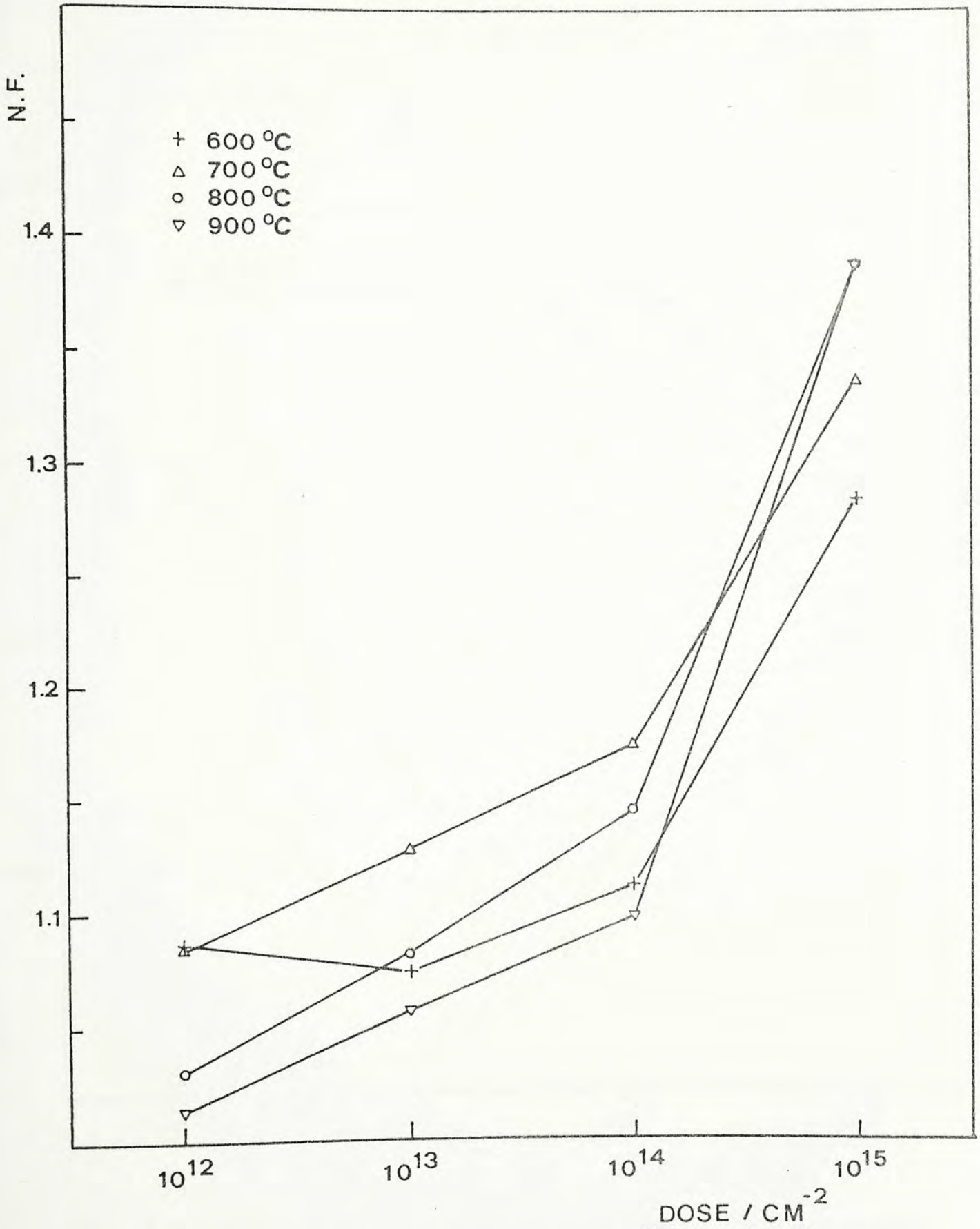

Fig. 4.7 Ideality factor versus dose for various annealing temperatures. (set A - 20 KeV implant, single step annealing)

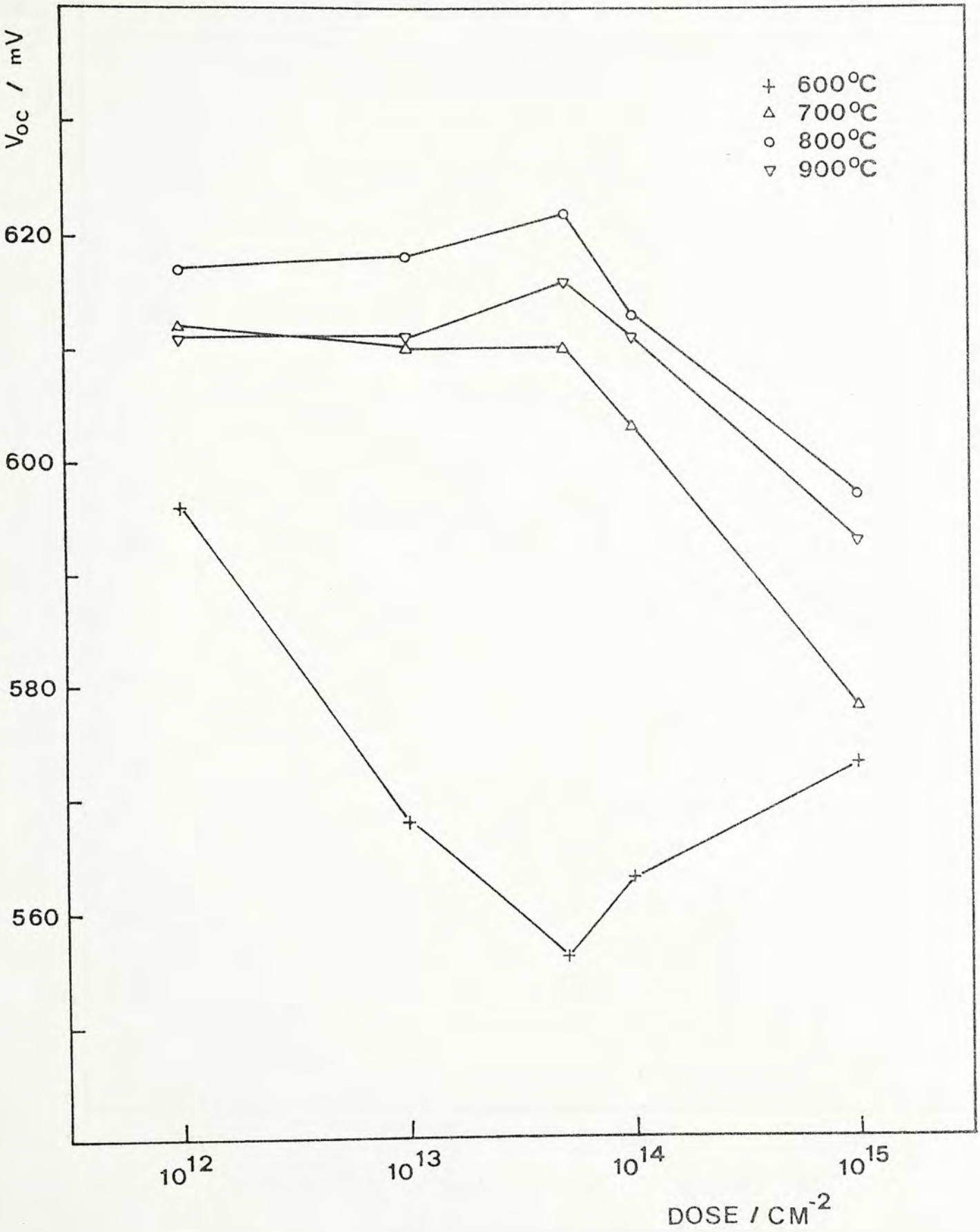

Fig. 4.8 Open circuit voltage versus dose for various annealing temperatures. (set B - 20 KeV implant, three step annealing)

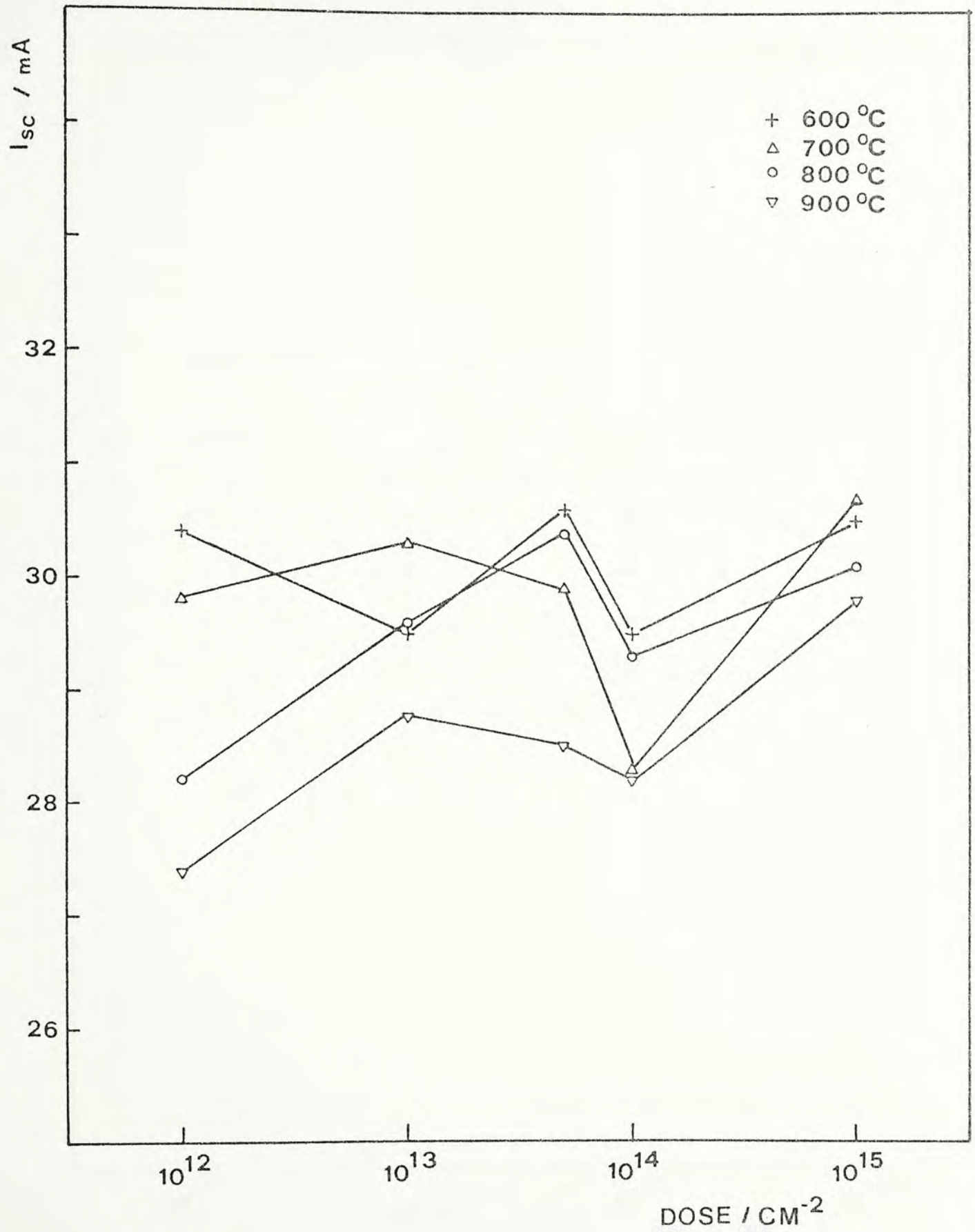

Fig. 4.9 Short circuit current versus dose for various annealing temperatures. (set B - 20 KeV implant, three step annealing)

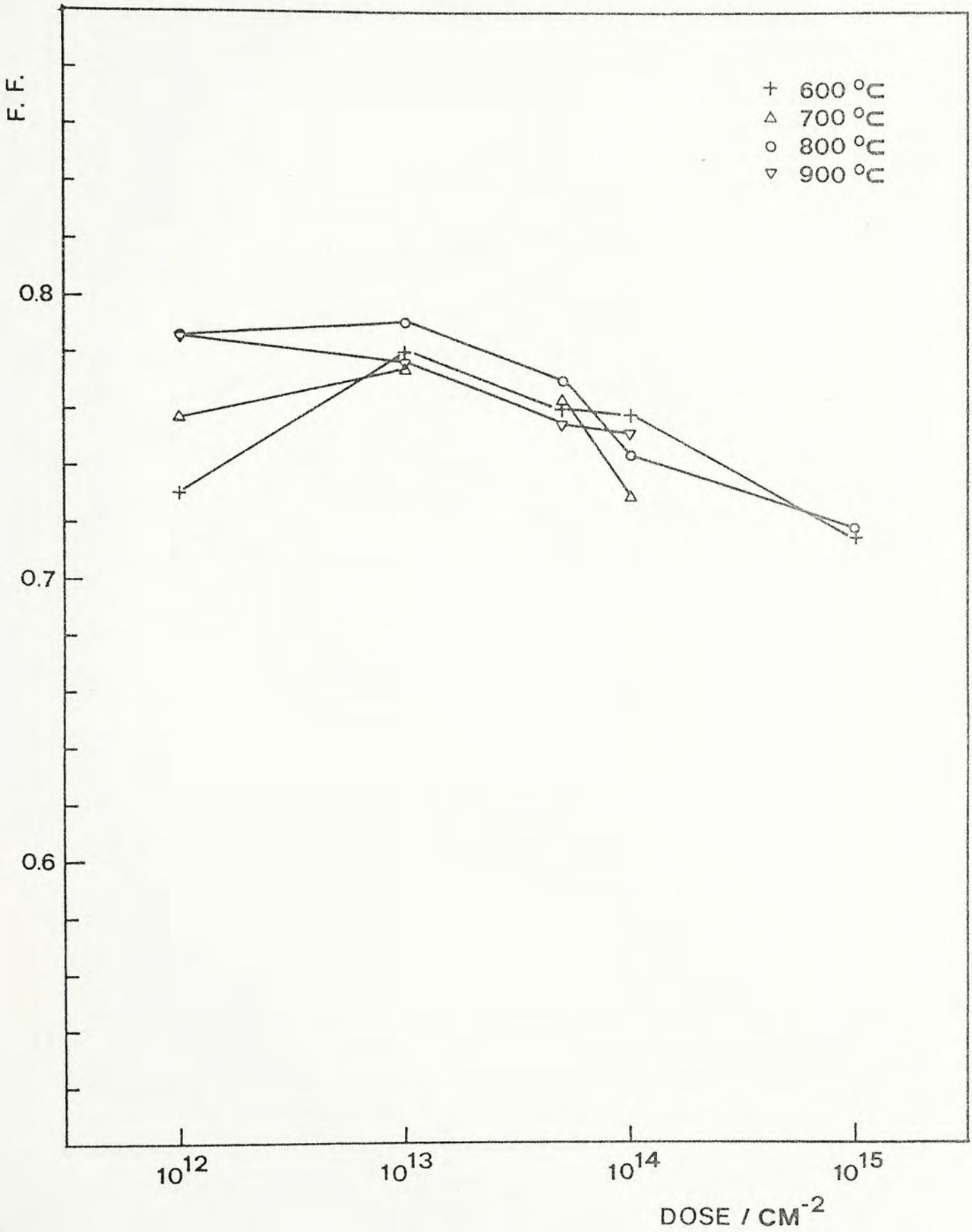

Fig. 4.10 Fill factor versus dose for various annealing temperatures. (set B - 20 KeV implant, three step annealing)

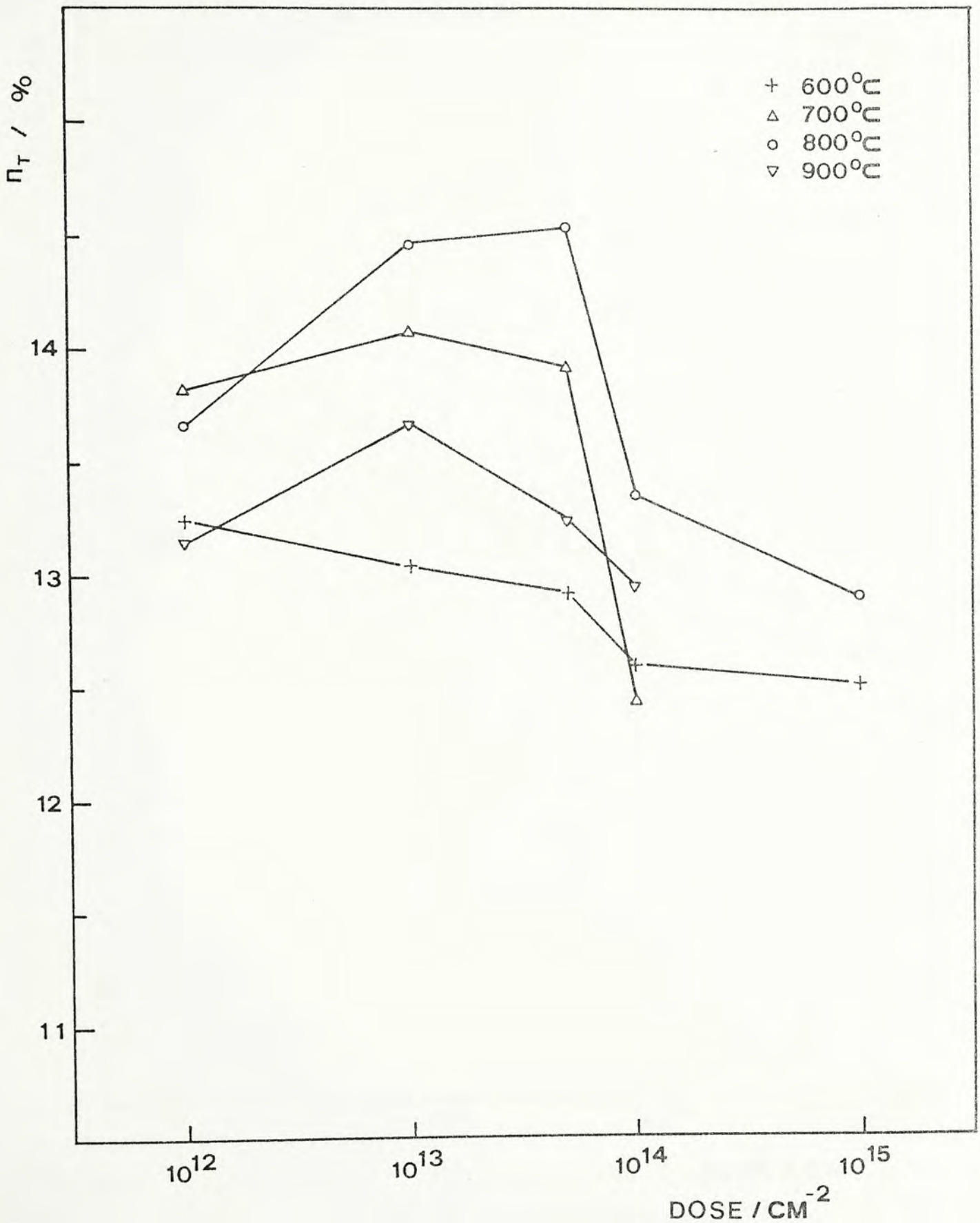

Fig. 4.11 Total area efficiency versus dose for various annealing temperatures. (set B - 20 KeV implant, three step annealing)

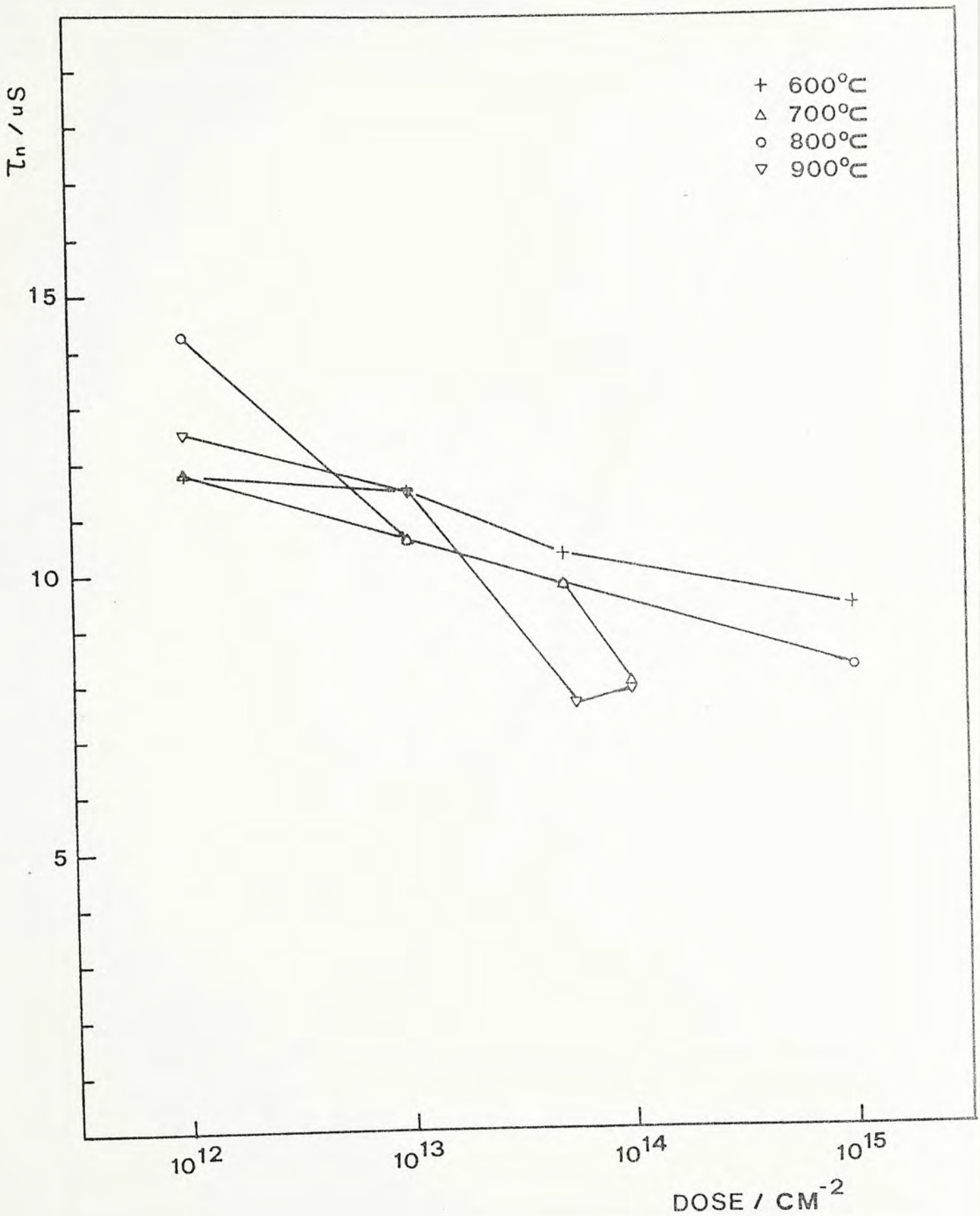

Fig. 4.12 Minority carrier lifetime versus dose for various annealing temperatures. (set B - 20 KeV implant, three step annealing)

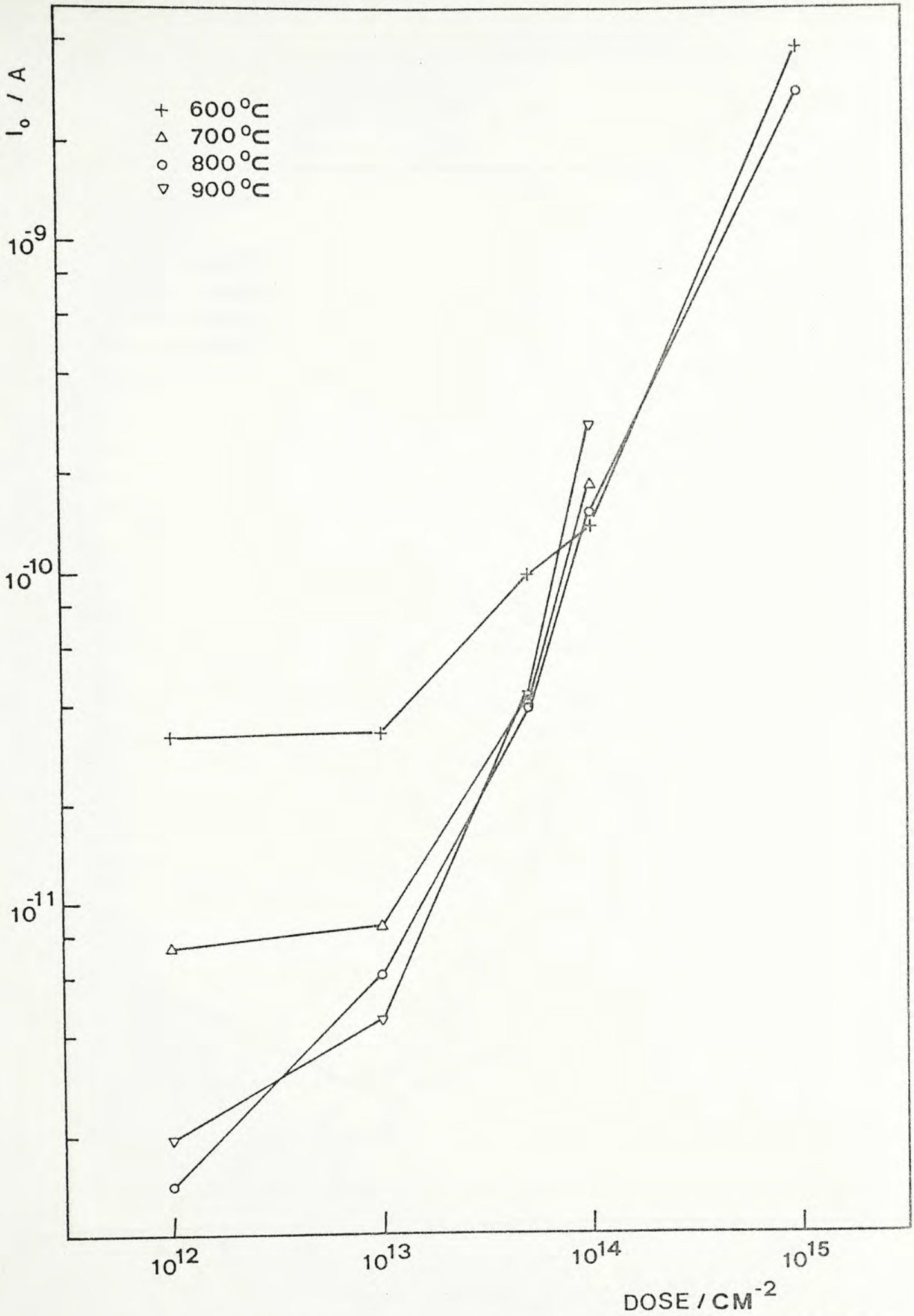

Fig. 4.13 Saturation current versus dose for various annealing temperatures. (set B - 20 KeV implant, three step annealing)

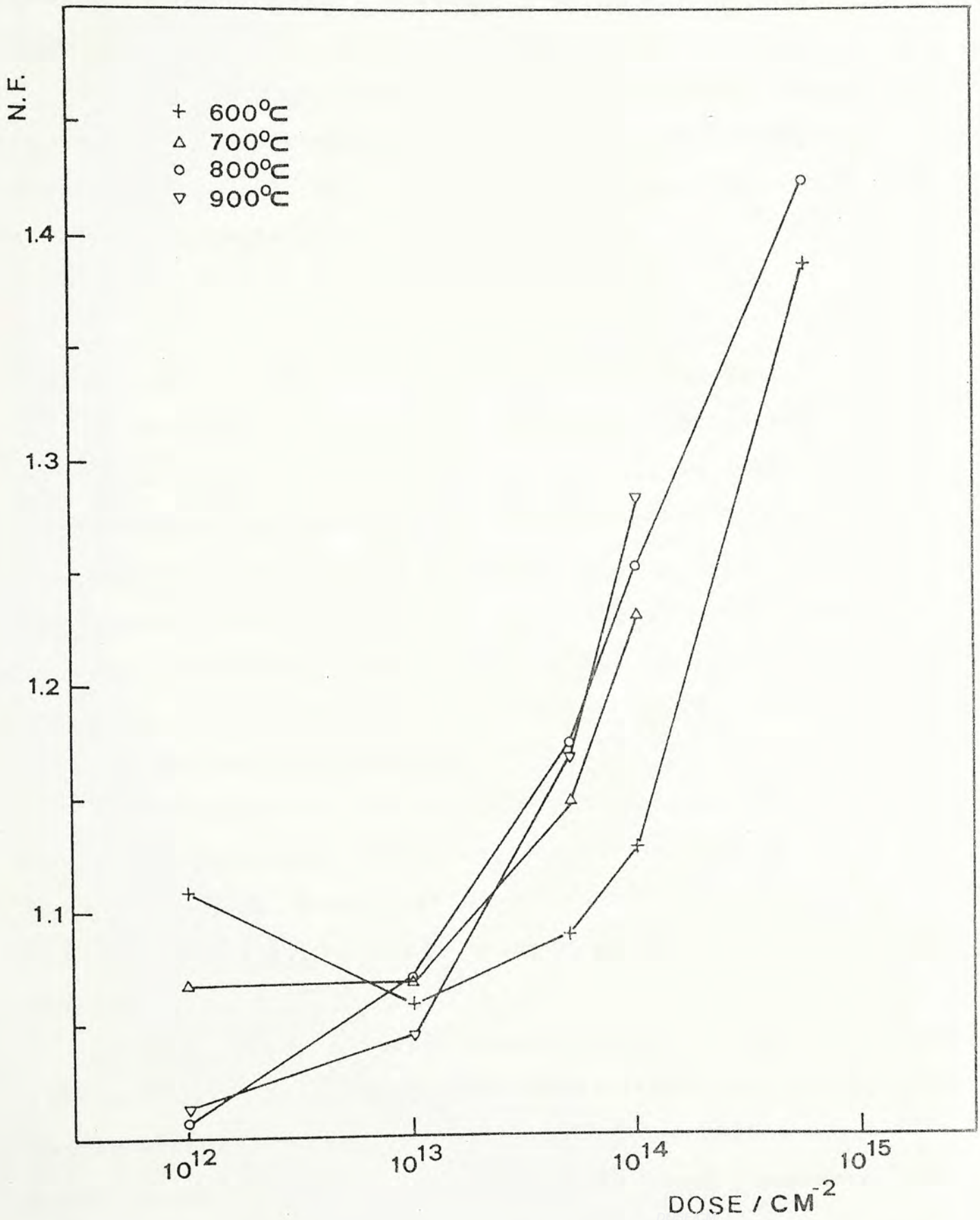

Fig. 4.14 Ideality factor versus dose for various annealing temperatures. (set B - 20 KeV implant, three step annealing)

10^{13} cm^{-2} - $5x10^{13}$ cm^{-2} under 800°C anneal. The peak is broader than that in set A which allows a large range of optimum dose level.

Although no significant advantage in efficiency is observed in the three step annealing over the single step annealing, it does yield a higher open circuit voltage. Therefore, three step annealing is adopted in the following study.

4.3.3 Set C - 30 KeV implant, three step annealing

In this set of experiments, the annealing temperature was chosen as 750°C to 900°C in 50°C increments in order to give a more detailed picture on the dependence of the annealing temperature. The results are shown in Fig. 4.15 - Fig. 4.21. The general behavior is again similar to set A and set B. However, performance variation against different annealing conditions is smaller which suggests that 750°C - 900°C anneals all give satisfactory annealing effects.

The results will be discussed briefly as follows. In Fig. 4.15, high open circuit voltage is obtained by 800°C and 850°C anneals at dose level of 10^{13} cm^{-2} and 10^{14} cm^{-2}. In Fig. 4.16, the short circuit current increases with the dose level as in set A.

In Fig. 4.17, the fill factor peaks at dose level of 10^{13} cm^{-2} while lower temperature anneal result in a higher fill factor except for heavily doped cases. The efficiency (Fig. 4.18) rises and then falls as the dose level increases. It peaks at a dose level of 10^{13} cm^{-2} under 800°C anneal which is

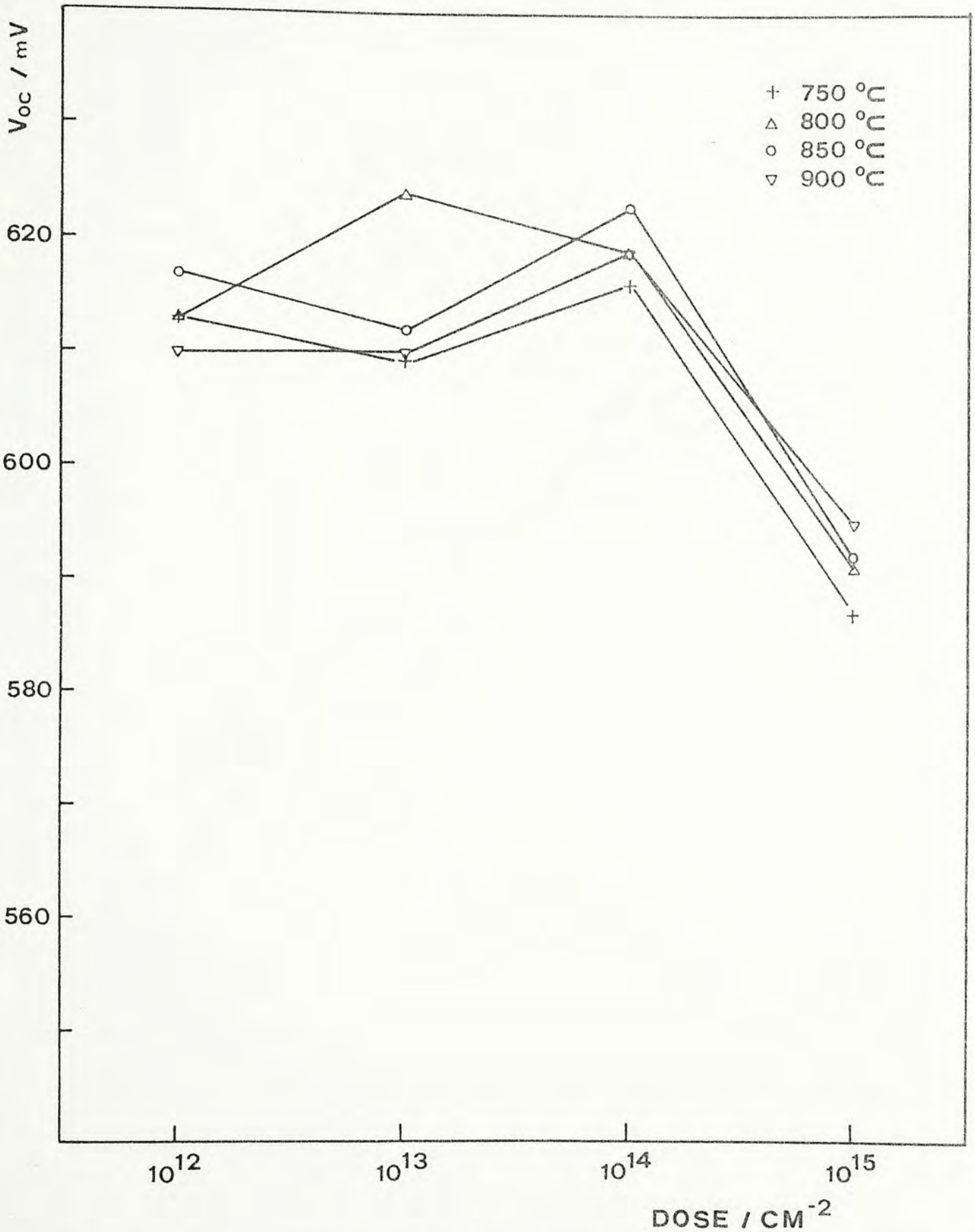

Fig. 4.15 Open circuit voltage versus dose for various annealing temperatures. (set C - 30 KeV implant, three step annealing)

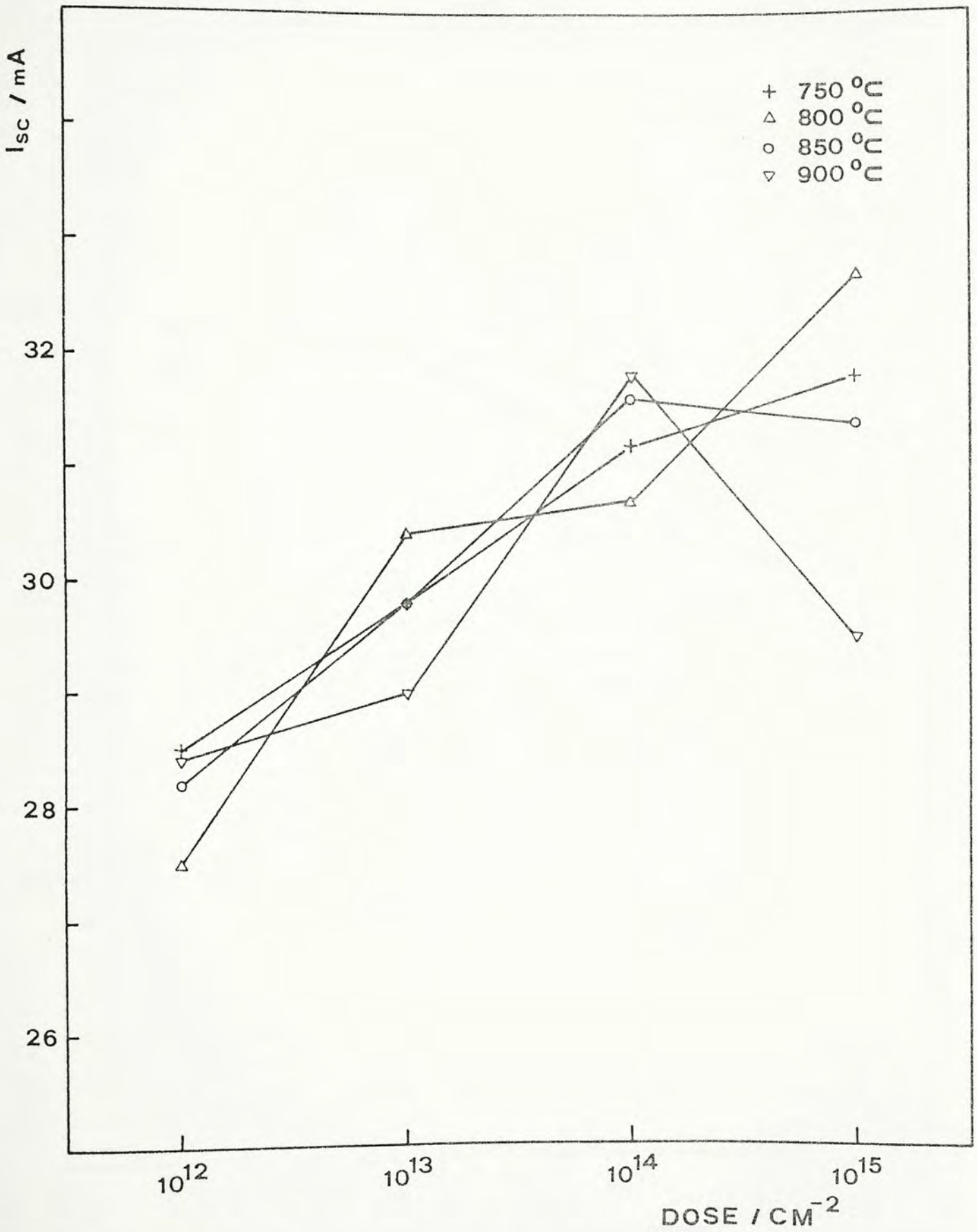

Fig. 4.16 Short circuit current versus dose for various annealing temperatures. (set C - 30 KeV implant, three step annealing)

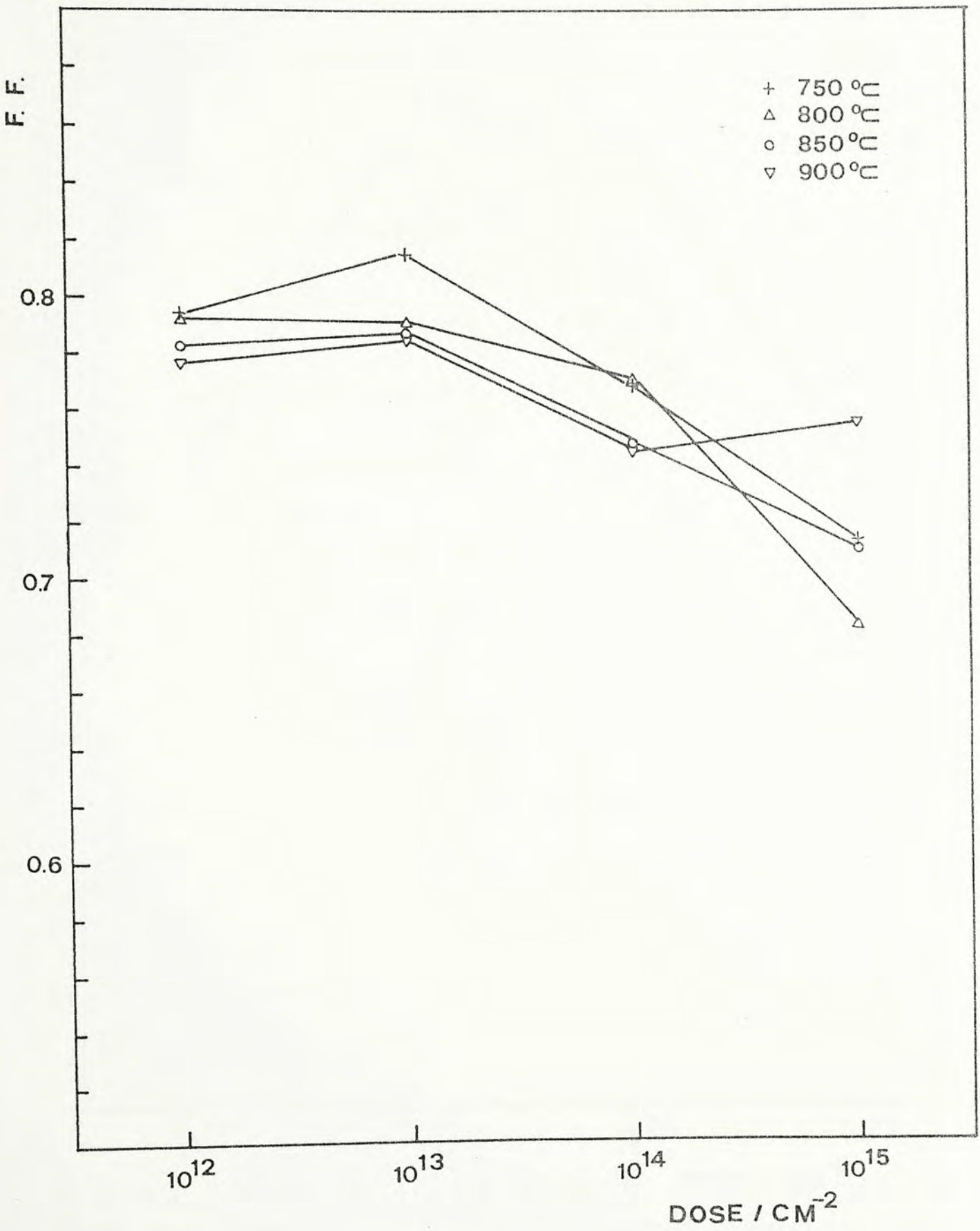

Fig. 4.17 Fill factor versus dose for various annealing temperatures. (set C - 30 KeV implant, three step annealing)

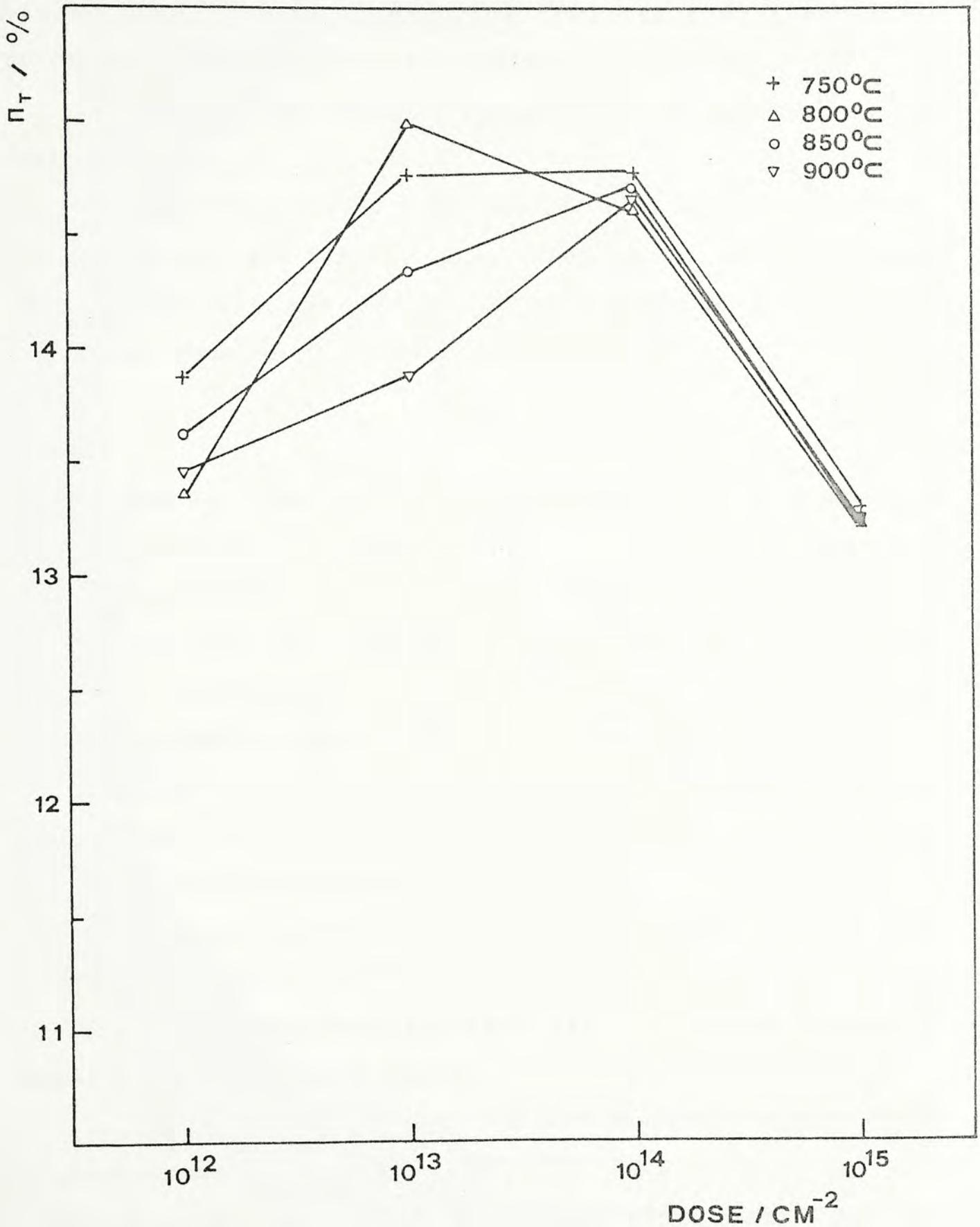

Fig. 4.18 Total area efficiency versus dose for various annealing temperatures. (set C - 30 KeV implant, three step annealing)

higher than that of set B. This implies that there is a performance advantage of 30 KeV implant over 20 KeV implant.

In Fig. 4.19, the minority carrier lifetime decreases as the dose increases.

In Fig. 4.20 and Fig. 4.21, the saturation current and the ideality factor are slightly lower than that of set B although they follow the same trend. These help to explain the efficiency advantage observed in Fig. 4.18.

4.3.4 Set D - 30KeV through oxide implant, three step annealing

The results are shown in Fig. 4.22 - Fig. 4.29. Similar general behavior is also observed as in previous sets.

In Fig. 4.22, 800°C and 900°C anneals give high open circuit voltage. Insufficient anneal is observed at 700°C anneal in addition to 600°C anneal in set B.

The increase in short circuit current with dose level is small (Fig. 4.23). In Fig. 4.24, the fill factor follows the same trend as previous sets.

800°C anneal yields high efficiency (Fig. 4. 25) with peak at dose level of 10^{13} cm^{-2} which is a bit lower than that of set C. Same "anomalous" behavior as in set B is observed at 600°C anneal due to insufficent anneal.

In Fig. 4. 26, the carrier lifetime follows the same trend as previous sets.

In Fig. 4. 27 and Fig. 4.28, the saturation current and the ideality factor are higher than set C although they follow the

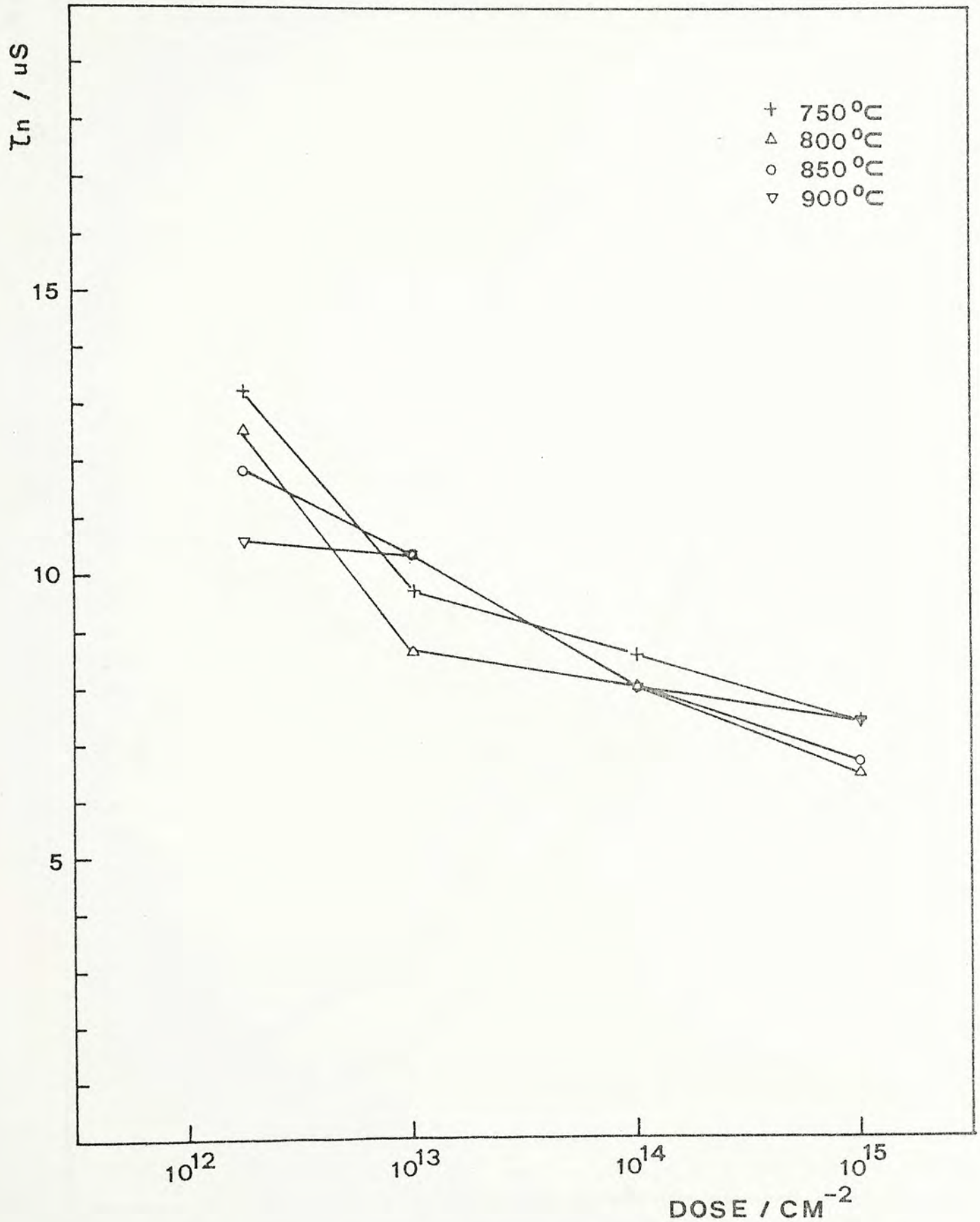

Fig. 4.19 Minority carrier lifetime versus dose for various annealing temperatures. (set C - 30 KeV implant, three step annealing)

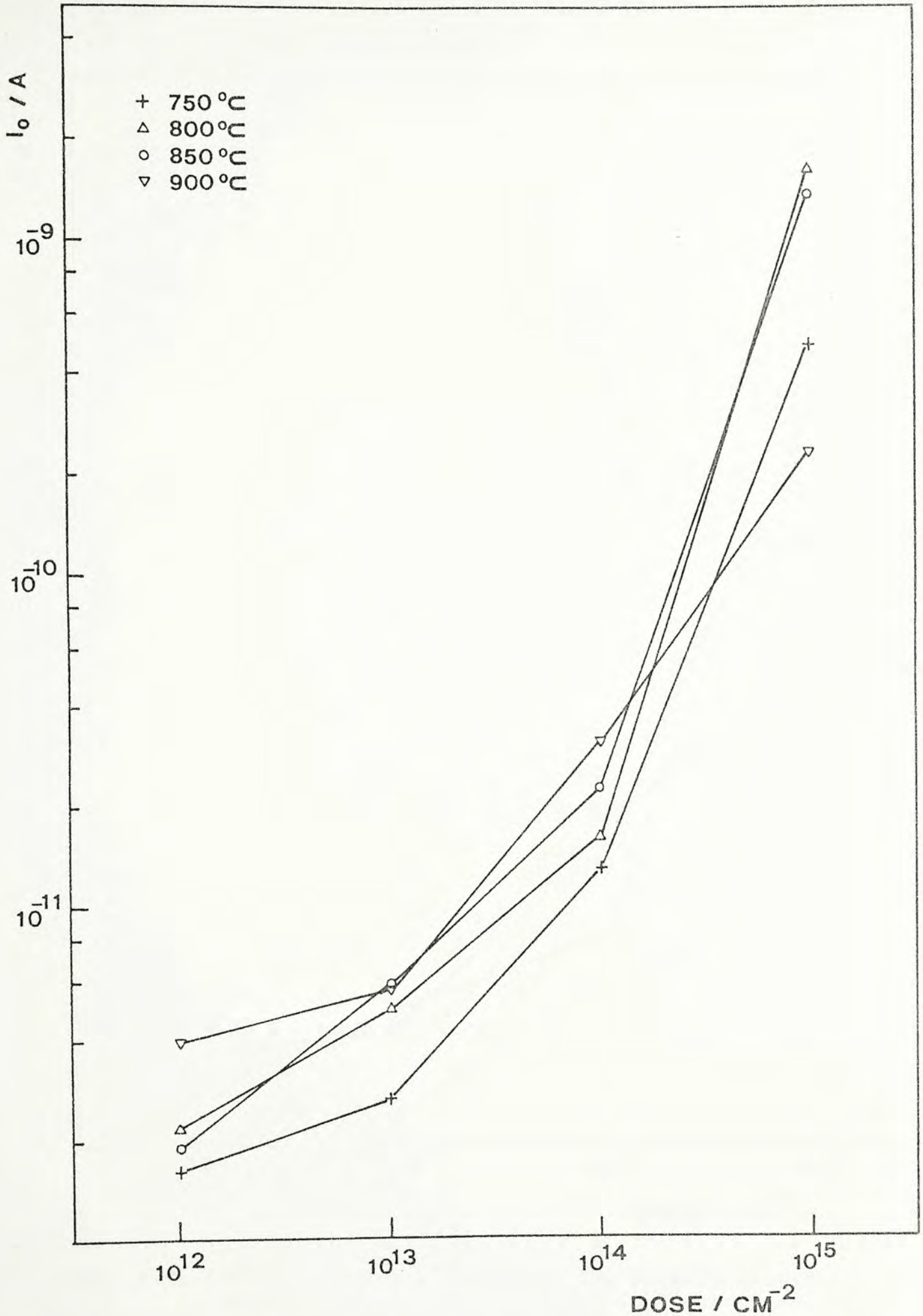

Fig. 4.20 Saturation current versus dose for various annealing temperatures. (set C - 30 KeV implant, three step annealing)

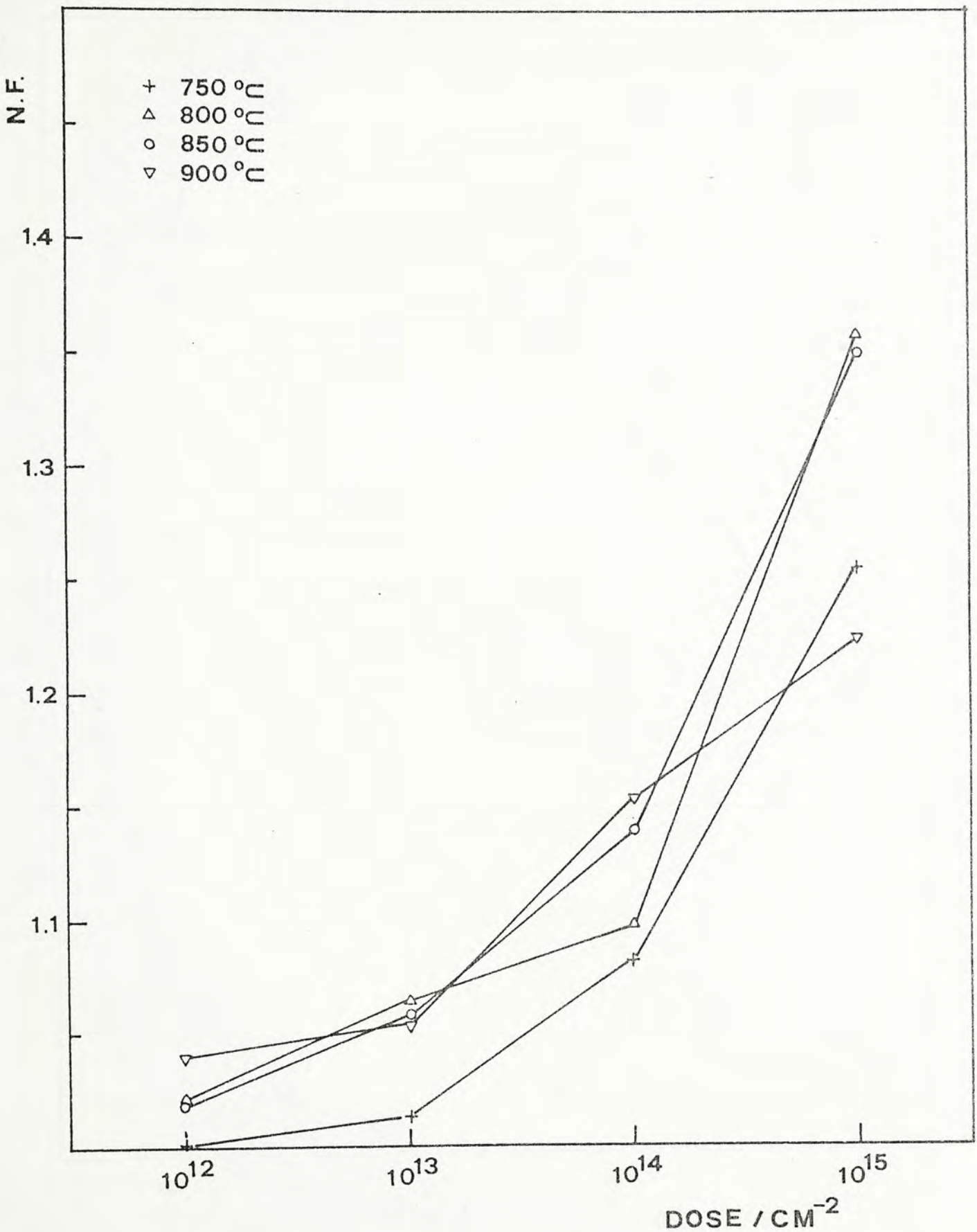

Fig. 4.21 Ideality factor versus dose for various annealing temperatures. (set C - 30 KeV implant, three step annealing)

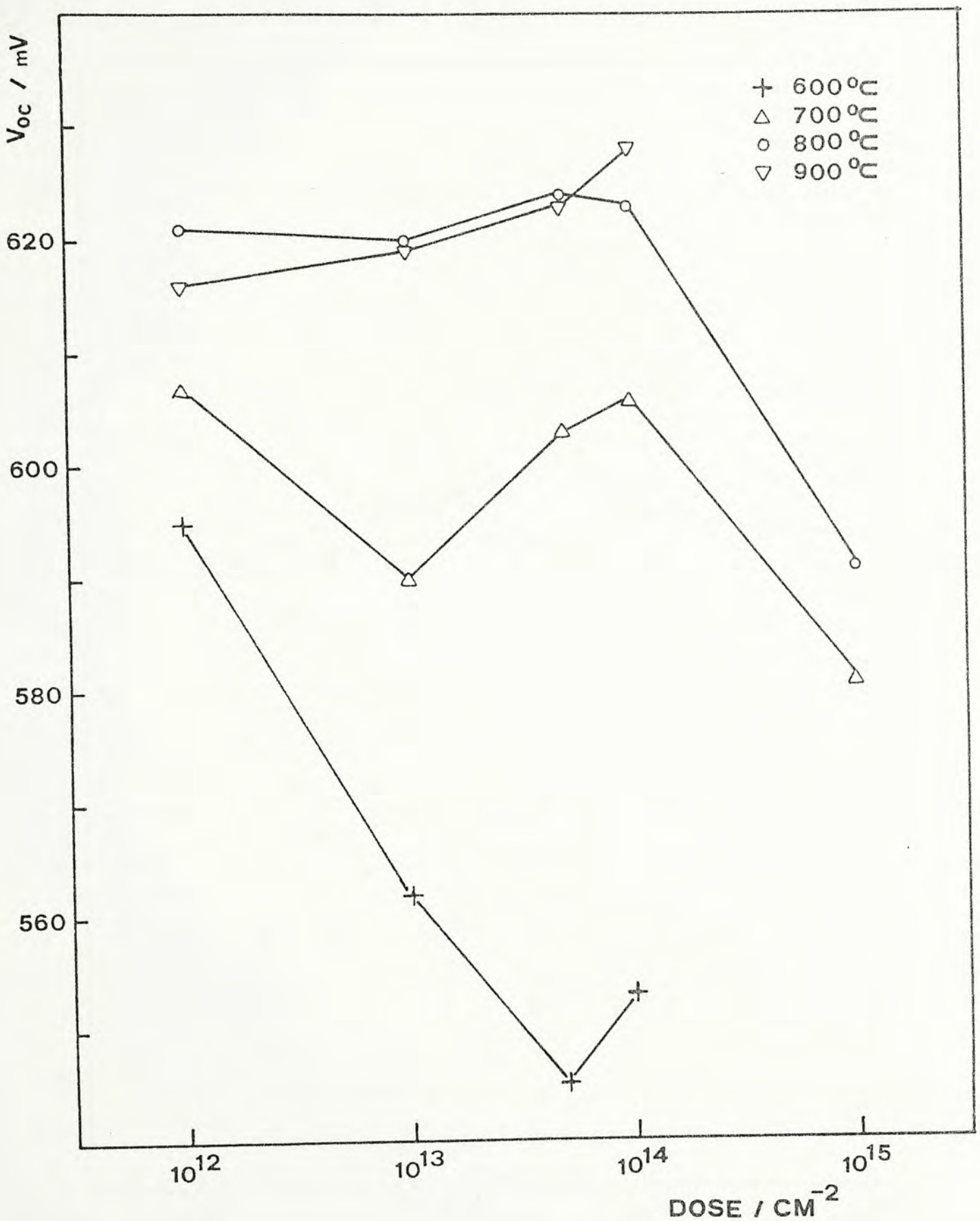

Fig. 4.22 Open circuit voltage versus dose for vaious annealing temperatures. (set D - 30 Kev through oxide implant, three step annealing)

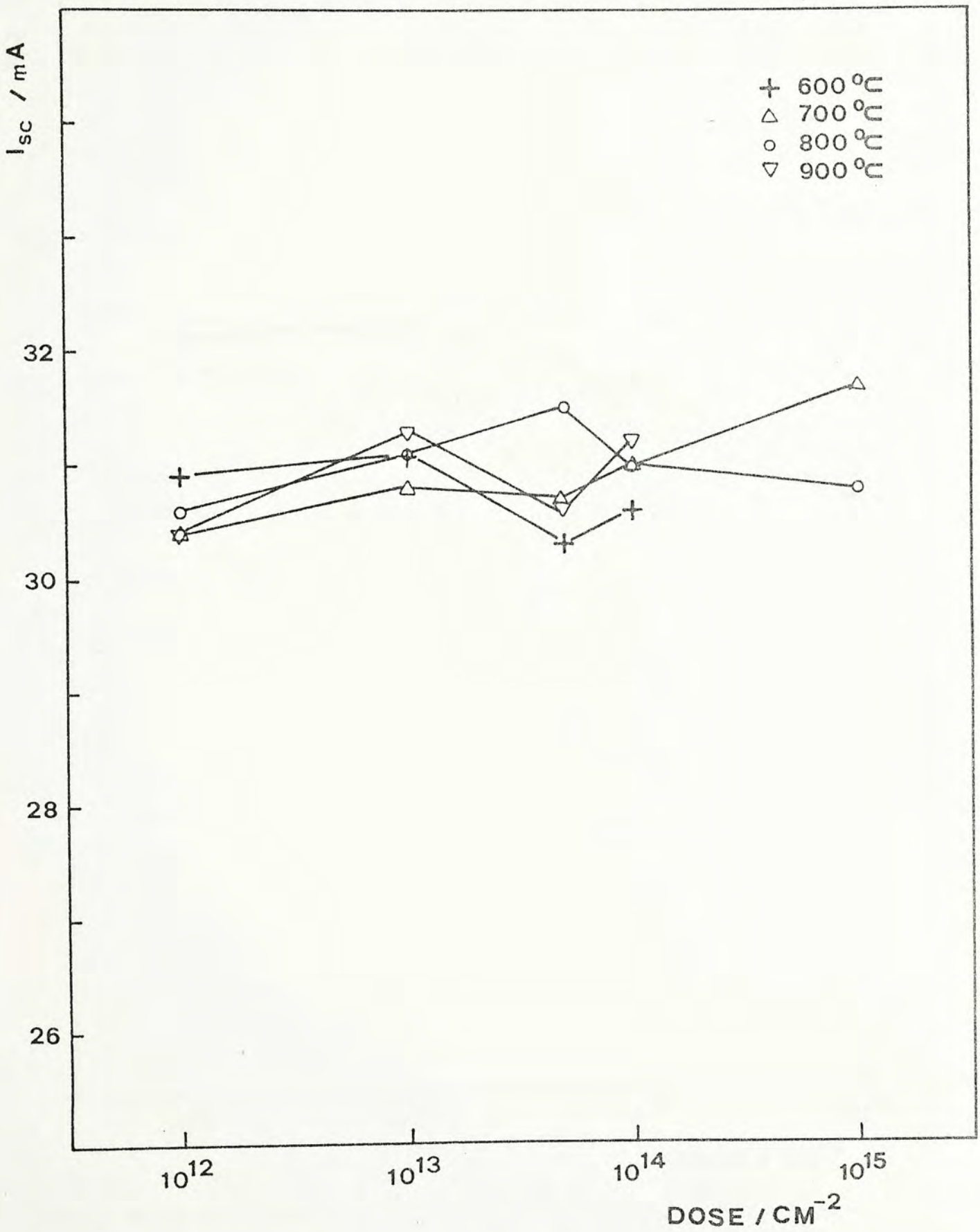

Fig. 4.23 Short circuit current versus dose for various annealing temperatures. (set D - 30 KeV through oxide implant, three step annealing)

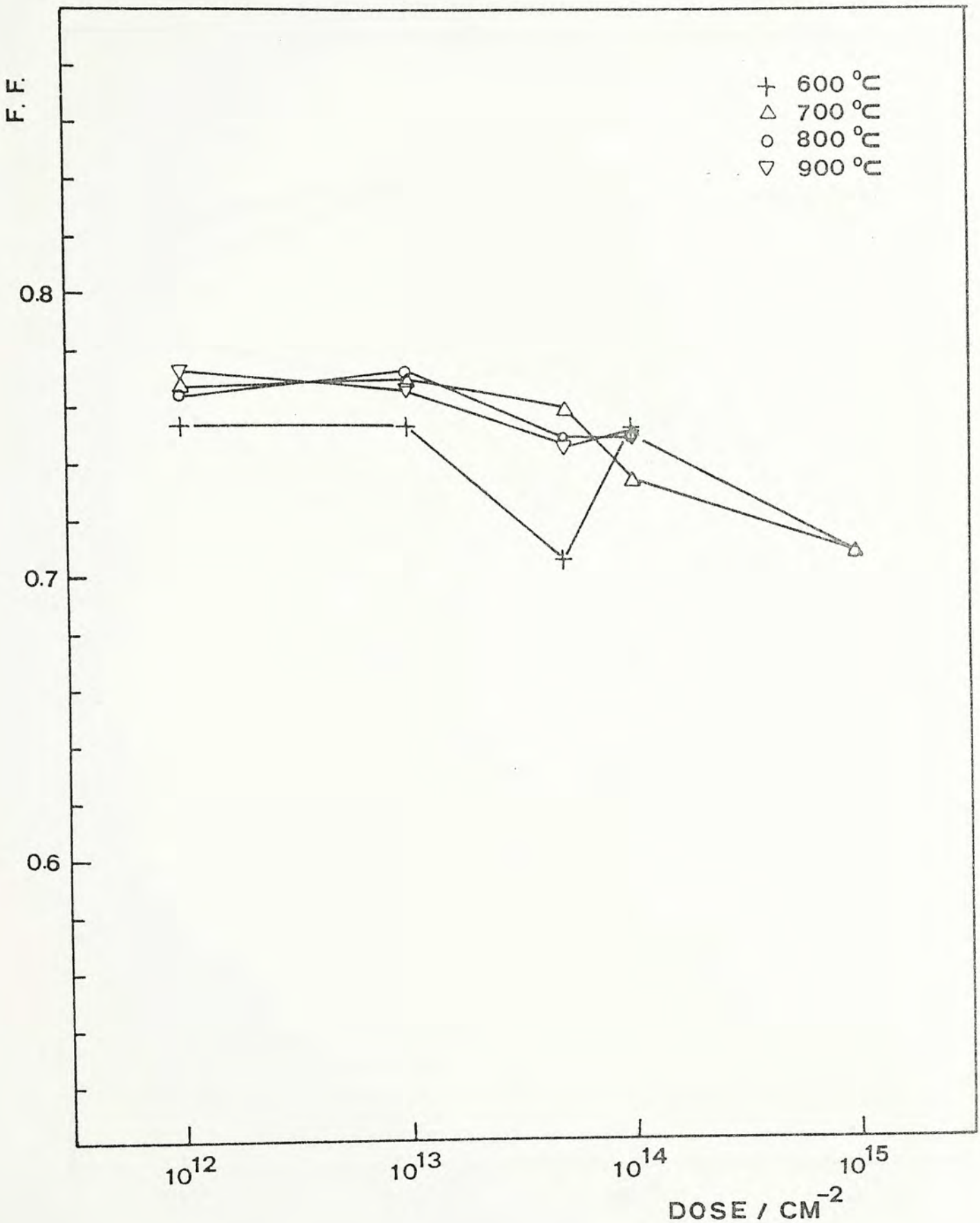

Fig. 4.24 Fill factor versus dose for various annealing temperatures. (set D - 30 KeV through oxide implant, three step annealing)

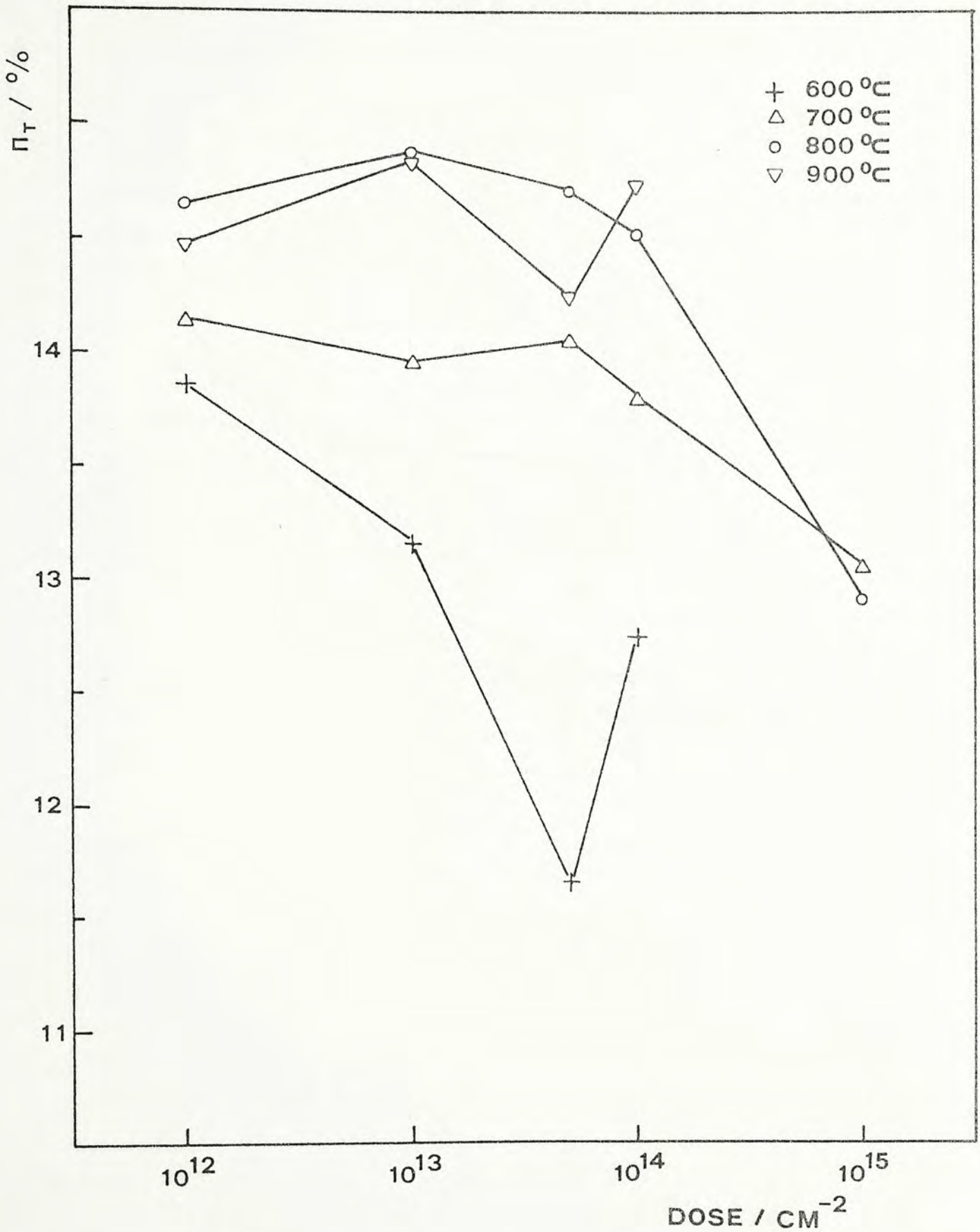

Fig. 4.25 Total area efficiency versus dose for various annealing temperatures. (set D - 30 KeV through oxide implant, three step annealing)

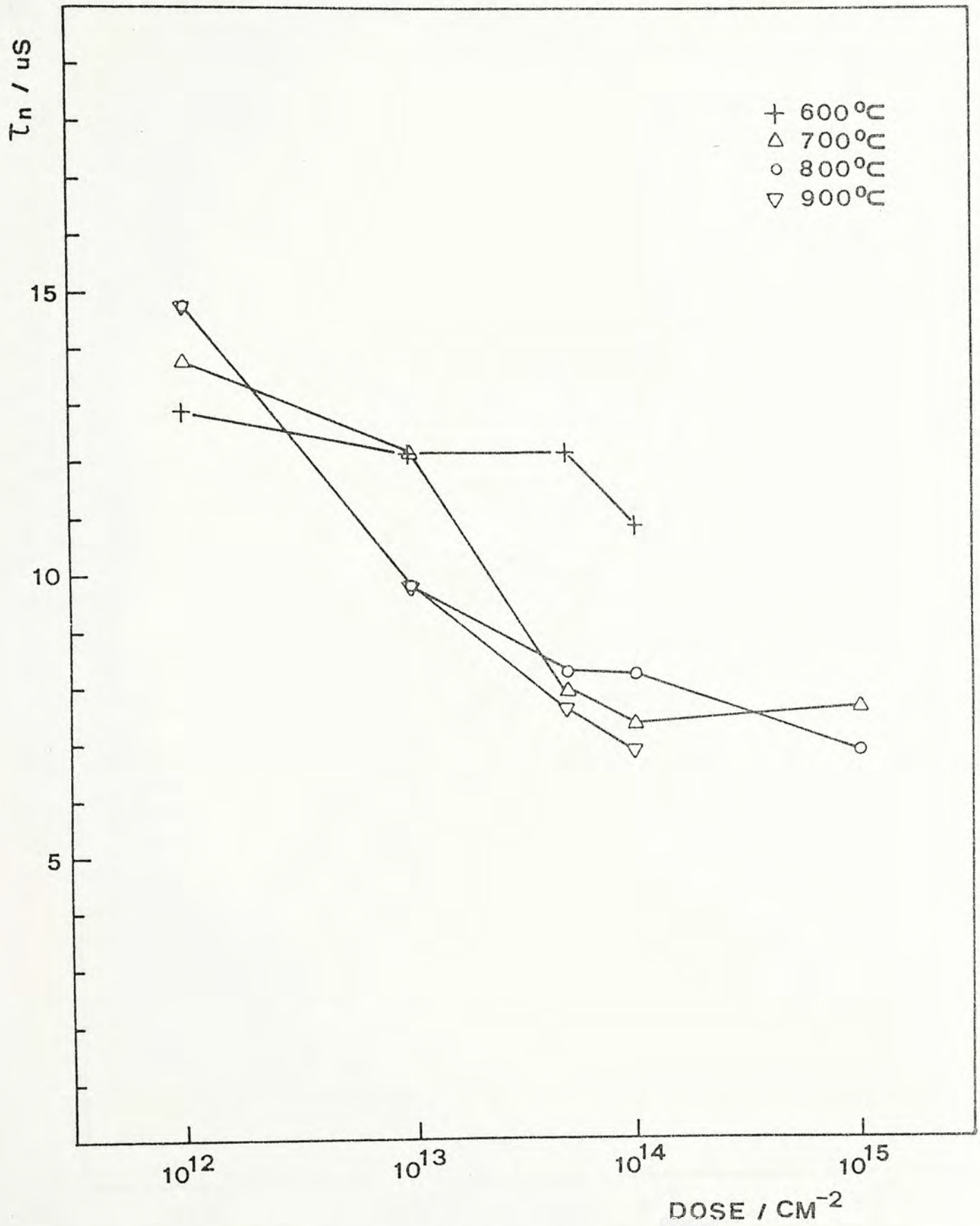

Fig. 4.26 Minority carrier lifetime versus dose for various annealing temperatures. (set D - 30 KeV through oxide implant, three step annealing)

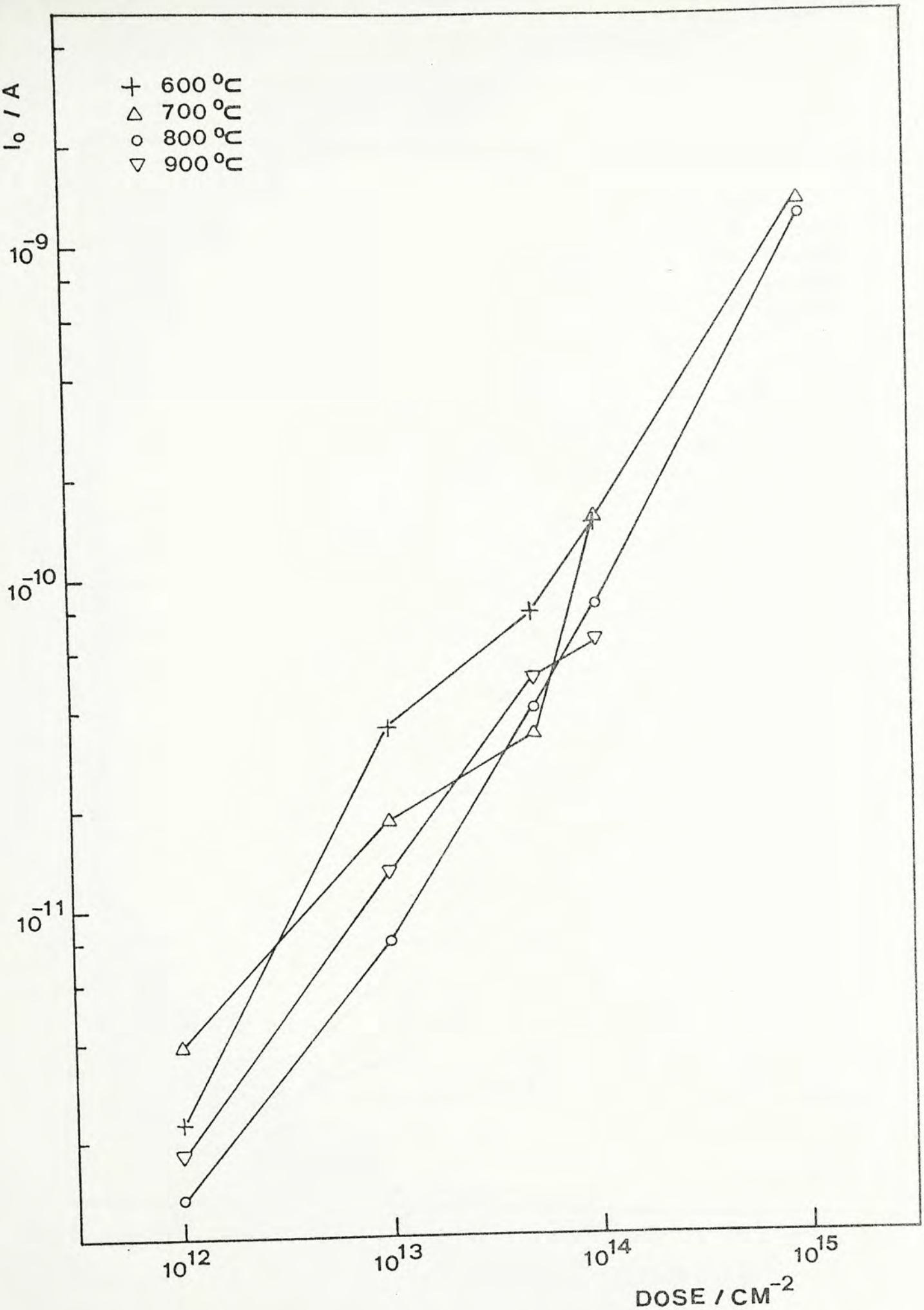

Fig. 4.27 Saturation current versus dose for various annealing temperatures. (set D - 30 KeV through oxide implant, three step annealing)

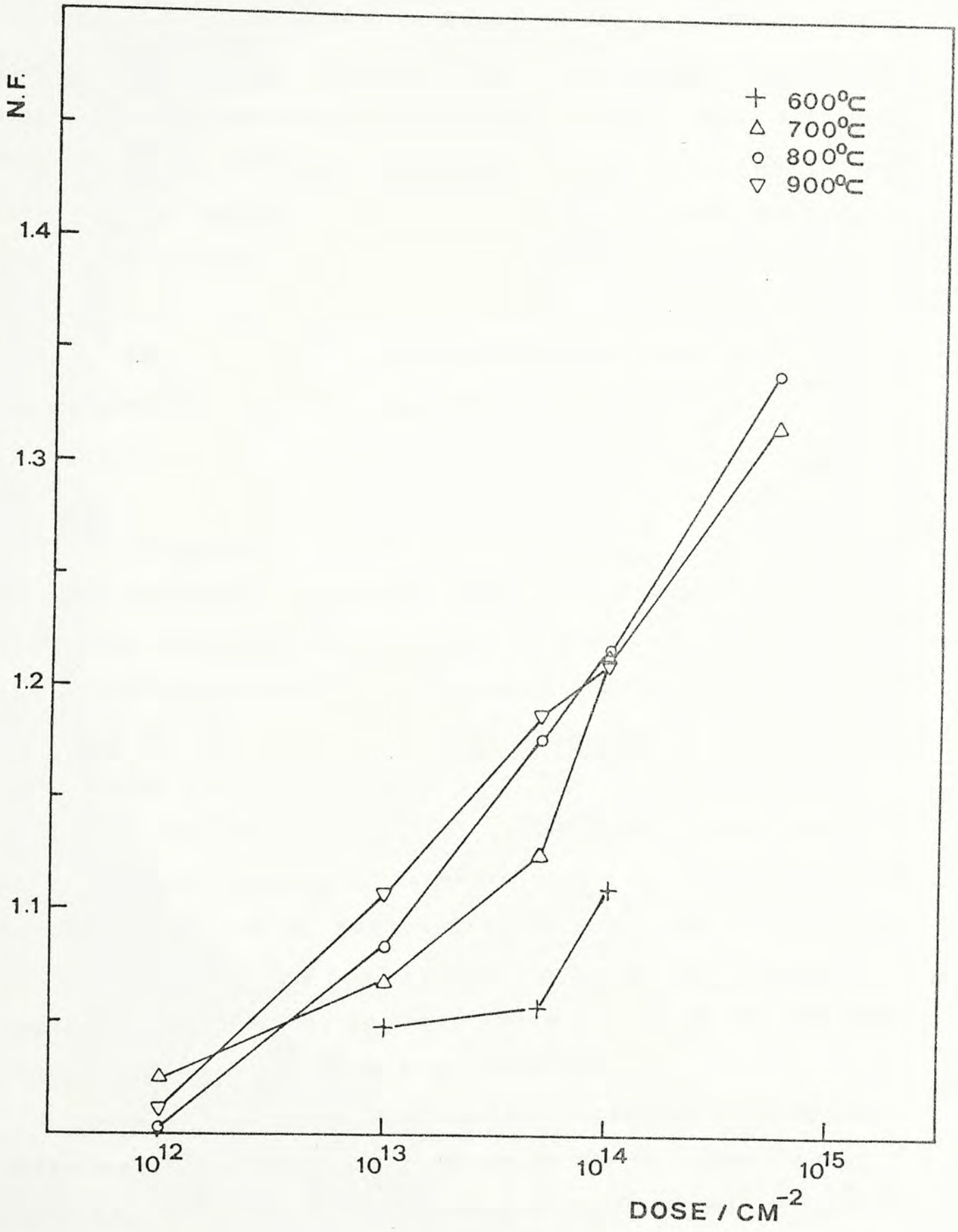

Fig. 4.28 Ideality factor versus dose for various annealing temperatures. (set D - 30 KeV through oxide implant, three step annealing)

same trend.

The spectral response is shown in Fig. 4. 29 for various dose at 800°C anneal. Cell with dose level of $5x10^{13}$ cm^{-2} shows superior short wavelength response than others. While cell with dose level of 10^{12} cm^{-2} indicates a lower long wavelength response than others. The superior short wavelength response at dose level of $5x10^{13}$ cm^{-2} suggests that there is optimum surface concentration which reduces the surface recombination (section 2.2.1). The lower long wavelength response indicates a higher series resistance at dose level of 10^{12} cm^{-2}.

4.3.5 Comparison

The optimized performance parameters of each set of implant and anneal conditions are tabulated in Table 4.4. The optimized annealing temperature in all cases is 800°C. Also shown in Table 4.4 are typical performance parameters of MIS and 800°C heat treated MIS solar cells.

Among the four sets of implant and anneal conditions, the 30KeV implant, three step annealing (set C) yields the best performance. The 30 KeV implants (set C and set D) are superior to the 20 KeV implants (set A and set B). There is no significant difference in performance for the 20 KeV implants under single step and three step annealing.

There is a definite performance advantage of MINP solar cells over MIS solar cells as shown in the efficiency entry of Table 4.4. This is due to the superior short circuit current in MINP cells than MIS cells since there is only marginal advantage

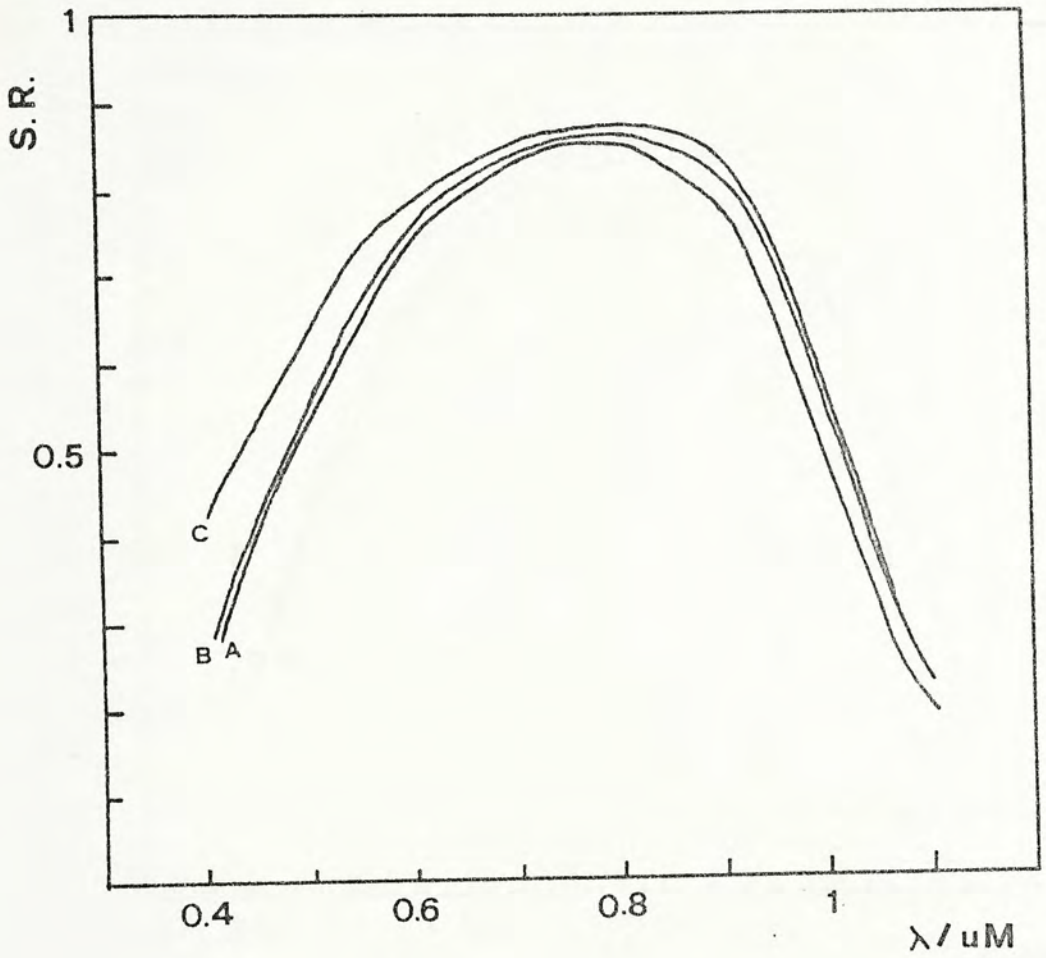

Fig. 4.29a Spectral responses (arbitrary unit) for various doses. A - 10^{12} cm^{-2}, B - 10^{13} cm^{-2}, C - $5x10^{13}$ cm^{-2}

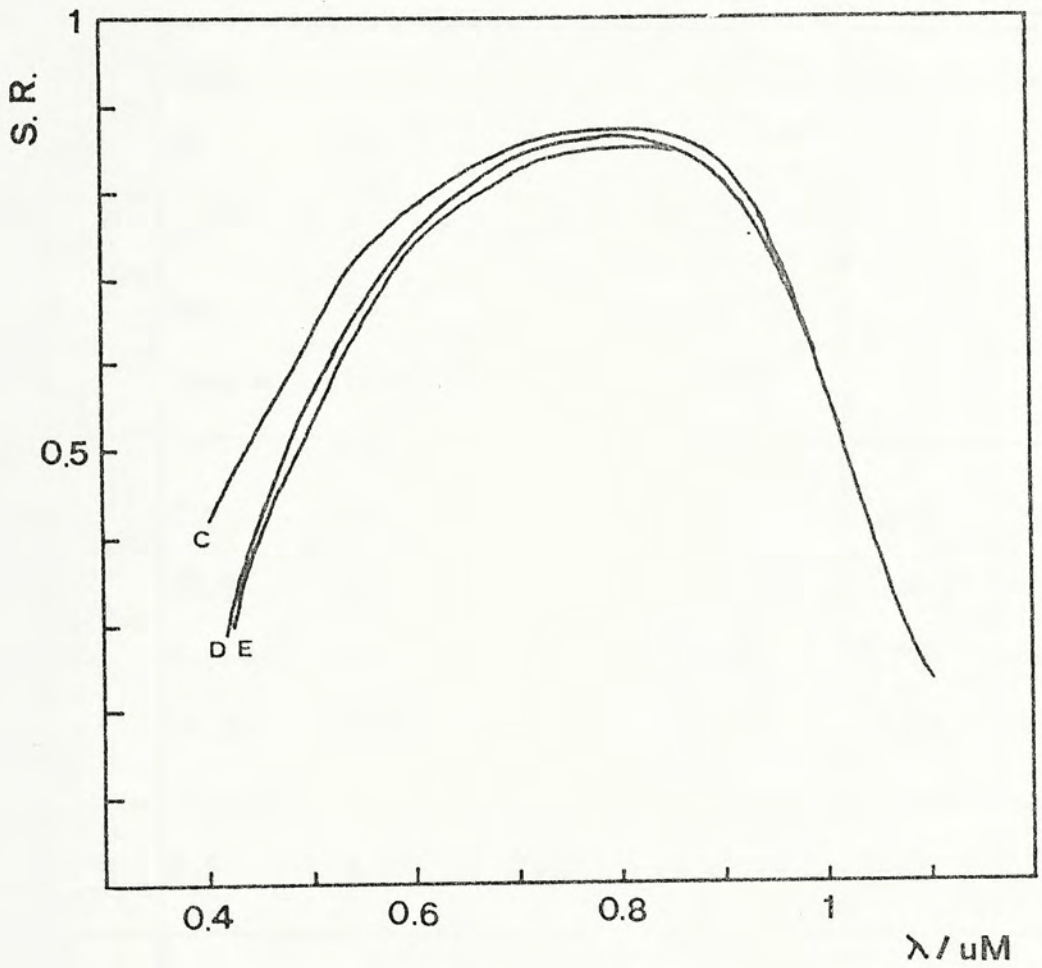

Fig. 4.29b Spectral responses (arbitrary unit) for various doses. C - 5×10^{13} cm^{-2}, D - 10^{14} cm^{-2}, E - 10^{15} cm^{-2}

Table 4.4

	MINP				MIS	MIS (800°C H.T.)
Energy / KeV	20	20	30	30 thro' oxide		
Dose / cm^{-2}	10^{14}	$5x10^{13}$	10^{13}	10^{13}		
Annealing temperature/°C and step	800 single	800 three	800 three	800 three		
V_{oc} / mV	617	622	624	620	620	612
I_{sc} / mA	30.9	30.4	30.4	31.1	28.7	27.2
FF	0.764	0.770	0.791	0.772	0.774	0.766
n_m / %	14.56	14.56	15.00	14.89	13.78	12.75
τ_n / us	8.5	9.8	8.6	9.9	14.8	13.2
I_o / $10^{-12}Acm^{-2}$	29.3	39.7	4.95	8.02	1.32	3.26
n	1.145	1.174	1.066	1.085	1.006	1.039

on open circuit voltage.

As shown in Table 4.4, the saturation current of the MINP cells is generally higher than the MIS cells which erode the potentially higher open circuit voltage resulting from the superior short circuit current through (3.22). Also, if the low carrier lifetime of the MINP cells can be raised to the level of the MIS cells, an even higher short circuit current and efficiency will be obtained. However, this may involve other annealing procedures [7].

Comparing to the lifetime degradation in the pre-processing heat treated MIS cells, the percentage degradation in the ion implanted MINP cells are much severer than the former. We conclude that the lifetime degradation of the latter is mainly due to the effect from ion implantation (residual damage and unactivated dopants). Results also indicate that different annealing conditions do not offset the above conclusion.

The saturation current and the ideality factor of the ion implanted MINP cells again increase to a larger extent than that of the MIS cells. These also lead to a similar conclusion that the effects are dominated by the doping level. The increase in the ideality factor is in qualitative agreement with the calculation shown in Fig. 2.5.

The saturation current due to the diffusion component in the bulk as the bulk lifetime decrease to 7 us (the extreme value measured) is 1.8×10^{-12} A/cm^2. However, the measured saturation

current is one to two order of magnitude above this figure. This implies that a recombination current through traps in the surface region dominates the total saturation current since the saturation current due to diffusion in the surface n region is only of the order of 10^{-12} A/cm^2.

In a recent publication [17], Anderson et al. observed a field emission current in their MINP cells. They deduced the excess current by subtracting the diffusion current component using the value obtained from V_{oc}/J_{sc} measurements from the total current. The ideality factor of the excess current component should be equal to two and independent of temperature if the current is due to recombination through traps in the depletion region. It has been observed [18] in a heavily doped metal/nSi junction where high field effects occur, the ideality factor increased at decreased temperature. Anderson et al. found that the product of the ideality factor of the excess current and the temperature is constant for their cells which have a high surface dose of 2×10^{15} cm^{-2}. Thus, they suggested that the excess current component was a field emission current resulting from edge effects rather than a recombination current for MINP cells. By diamond sawing the edge of the cells, they improved the ideality factor of the excess current from 3.3 to 2.6.

Typical values of the excess current and the ideality factor for our cells are shown in Table 4.5. The ideality factor of the excess current at high dose (10^{15} cm^{-2}) is exceptionally high and agrees with the founding of Anderson et al.. But at a lower dose, the ideality factor is still reasonably close to two. This suggests that the recombination current through traps in the

depletion region dominates.

Table 4.5

Dose (cm^{-2})	n_e	J_e (A/cm^2)
10^{13}	2.1	2.0×10^{-7}
5×10^{13}	2.3	3.6×10^{-7}
10^{14}	2.2	2.7×10^{-7}
10^{15}	2.8	4.3×10^{-6}

The junction recombination current through traps for forward bias is given approximately by [19]

$$J_{rg} = q\int_{x_p}^{x_n} U_{max}\, dx = J_{rgo}\,(\exp(qV/2kT) - 1) \qquad (4.1)$$

$$\text{where } J_{rgo} = \frac{n_i W_d kT}{2(V_d - V)\,\tau_{no}}$$

To explain a $2\text{-}4 \times 10^{-7}$ A/cm^2 excess current using (4.1) with W_d = 0.2 um, V = 0.5 V, it requires τ_{no} to be 3.8×10^{-9} sec. Such a τ_{no} is not unreasonable since unactivated dopants and residual damage may exists in this region.

The finding that the field emission component occurs at high dose but not at low dose is consistent with the theory of field emission. A heavier doped semiconductor favors the field emission current to occur [20]. However, such component is not intrinsic to MINP cells but occurs also in MNP cells [17].

4.4 Conclusions

Implant and annealing conditions have been studied in detail for the ion implanted MINP cells. The dependence on such conditions has not been found in the literature.

The ion implanted MINP cells have shown to have a definite peformance advantage over the MIS cells due to the superior short circuit currrent and the marginal increase in open circuit voltage.

Among the four sets of implant and annealing conditions, the 30 KeV implant, three step annealing (set c) yields the best performance. The 30 KeV implants (set C and set D) are superior to the 20 KeV implants (set A and set B). No significant performance difference is observed for 20 KeV implants under single step and three step annealing.

Annealing behavior of ion implantation is complex in nature. Insufficient anneal occurs at low temperature (600^{o}C). A dip in open circuit voltage and efficiency at medium dosage relative to low and high dosage is observed. It is explained by the effects of unactivated dopants, residual damage and formation of amorphous layer. High temperature annealing (900^{o}C) does not produce further activation of dopants and removal of residual damage, but lowers the carrier lifetime. The optimum annealing temperature is found to be 800^{o}C.

The best ion implanted MINP cell is fabricated under a dose level of 10^{13} cm^{-2} and three step annealing at 550^{o}C 2 hours, 800^{o}C 15 min, 550^{o}C 2 hours. The performance parameters are V_{oc} = 624 mV, I_{sc} = 30.4 mA, FF = 0.791 and n_T = 15 % at AM1.5 illumination. The dose level is 200 times less than that used in

conventional ion implanted p-n junction solar cells. This implies that ion implantation using a MINP structure may be cost competitive to diffusion.

The degradation in the carrier lifetime in the ion implanted MINP solar cells is much more severe than that of the heat treated MIS solar cells which leads to a conclusion that the lifetime of the former is mainly due to the effects of unactivated dopants and residual damage brought about by ion implantation. Results also indicate that different annealing conditions do not offset the above conclusion.

Increases in the saturation current and the ideality factor are observed. The extent of increases is again larger thanthat of the heat treated MIS cells leading to a similar conclusion that the effects are dominated by the doping level. The increase in the ideality factor is in qualitative agreement with the calculation in chapter 2.

The saturation current is analyzed to show that a recombination current through traps in the depletion region dominates at low dose level. While at high dose level, our result is consistent with Anderson et al. who have suggested that the field emission current dominates in their high dose MINP cells.

Spectral response measured supports the explanation of the performance dependence.

References

[1] F. Zignani, "Study of ion implanted n^+ layers for silicon solar cells," 1st Photov. Solar Energy Conf., p.113, 1977.

[2] A.R. Kirkpatrick et al., "Production technology for high efficiency ion implanted solar cells," 13th IEEE Photov. Spec. Conf., p.706, 1978.

[3] A.R. Kirkpatrick et al., "silicon solar cells by ion implantation and pulsed energy processing," 13th IEEE Photov. Spec. Conf., p.299, 1978.

[4] J.A. Minnucci et al., "Silicon solar cells with high open circuit voltage," 14th IEEE Photov. Spec. Conf., p.93, 1980.

[5] G. Miccoli, P Ostoja and S. Solmi, "The effects of laser and electron beam annealing on ion implanted silicon solar cells," 3rd Photov. Solar Energy Conf., p.719, 1980.

[6] G. Soncini, "The annealing of ion implanted silicon solar cell processing," 3rd Photov. Solar Energy Conf., p.270, 1980.

[7] R.T. Young, "Pulsed laser techniques for solar cell processing," IEEE Trans. Ele. Dev., Vol. 27, p807, 1980.

[8] E.C. Douglas and R.V. D'aiello, "An experimental study of the factors which control the efficiency of ion implanted silicon solar cells," 14th IEEE Photov. Spec. Conf., p.825, 1980

[9] E.C. Douglas and R.V. D'aiello, "A study of the factors which control the efficiency of ion implanted silicon solar cells," IEEE Trans. Ele. Dev., Vol. 27, p.792, 1980.

[10] J.P. Ponpon and P. Siffert, "Silicon solar cells made by ion

implantation and glow discharge," 11th IEEE Photov. Spec. Conf., p.342, 1975.

[11] Y.P. Pai, H.C. Lin, M. Peckerar and R.L. Kocher, "Ion implanted Schottky barrier solar cell," IEDM Tech. Dig., p.470, 1977.

[12] Y.P. Pai and H.C. Lin, "Analysis of ion implanted solar cells," 13th IEEE Photov. Spec. Conf., p.661, 1978.

[13] A.W. Blakers, M.A. Green and M.R. Willison, "High performance silicon solar cells using low dose phosphorus implants," Nucl. Instrum. Methods., Vol. 191, p.51, 1981.

[14] H. Goldman and M. Wolf, "Low cost processes for fabricating silicon solar cells," 14th IEEE Photov. Spec. Conf., p.923, 1980.

[15] E.C. Dougals, R.S. Silver and C.W. Mueller, "Ion implantation basics," RCA Lab. PRRL-72-TR-100, June, 1972.

[16] M.A. Green et al., "The MINP solar cell - a new high voltage, high efficiency silicon solar cell," 15th IEEE Photov. Spec. Conf., p.1405, 1981.

[17] B.B. Rao, S. Banerjce, W.A. Anderson and M.K. Kan, "Excess current in MINP type solar cells," IEEE Trans. Ele. Dev., Vol. 32, p817, 1985.

[18] A.N. Saxena, "Forward current voltage characteristics of Schottky barrier on n type silicon," Surface Science, Vol. 13, p.151, 1969.

[19] A.L. Fahrenbruch and R.H. Bube, Fundamentals of Solar Cells, Academic Press, p.119, 1983.

[20] E.H. Rhoderick, Metal Semiconductor Contacts, Clarendon Press, Oxford, p.97, 1978.

5. DIFFUSED MINP SOLAR CELLS

5.1 Introduction

Low temperature heat treatment which induces metallurgical reactions between the Al and n-Si has shown to increase the barrier height of the contact to majority carriers and decrease the dark current thereby increasing the open circuit voltage [1].

Green et al. have proposed a MINP structure which combined the advantages of metal-insulator-semiconductor and p-n junction technologies [2,3]. A thin surface doped layer is introduced by either diffusion or ion implantation. The latter has been discussed in chapter 4. Open circuit voltage as high as 694 mV (AM0) has been reported [4] by liquid source $POCl_3$ diffusion. The effect of partial pressure of $POCl_3$ during diffusion has been studied. A reduction in voltage at high pressure was, however, observed [4].

Further improvement in performance has been reported. Efficiency of 18 % (AM1.5) and 18.7 % (AM1.5) are obtained with the following modifications:

1. replacing top contact metal Mg by Ti/Pd/Ag multilayer contact metallization with reduced metal coverage,
2. employing thermal oxide surface passivation, and
3. employing double layer antireflection coating.

The highest efficiency in silicon cell reported to date is 19.1 % (AM1.5) [7] in which special attention has been paid to emitter passivation by thermal oxide and reduction of metal contact area.

Despite recent advancements, detailed dependence of

performance on diffusion conditions has not been reported in the literature. Investigation will be taken up in this chapter.

5.2 Experimentals

5.2.1 Experimental design

The two key independent parameters that can be controlled in diffusion are temperature and time. We have investigated the performance dependence on temperature and time under a single step diffusion process. Single step diffusion results in a steeper impurity gradient which has been shown to be beneficial for high performance in solar cells [8]. The important profile parameters calculated [9] with diffusion constants obtained from [10] are shown in Table 5.1. Section 5.3.1 gives the results of this investigation.

The surface doping also reduces the series resistance of the surface layer as discussed in section 2.2.2. A wider grid spacing than that demanded by the MIS cells is expected to give a high efficiency as well. Results are given in section 5.3.2.

It has been shown in [2] that the voltage advantage of the MINP cells over the MIS cells is maximum at a substrate resistivity of 0.1 ohm-cm and decreases as resistivity increases. We have compared the performance of the MINP cells on two available substrate resistivities, namely, 0.5 ohm-cm and 1.5 ohm-cm (see section 5.3.3).

5.2.2 Fabrication

$POCl_3$ liquid source diffusion was employed. The source was kept at 0^oC by an ice water bath and was introduced into the furnace by bubbling nitrogen through it at 30 cc/min. Oxygen

Table 5.1

a. Total Dose / cm^{-2}

Temp./°C \ Time/min	5	10	15
750	5.9×10^{12}	7.6×10^{12}	9.3×10^{12}
800	1.9×10^{13}	2.7×10^{13}	3.4×10^{13}
850	9.5×10^{13}	1.3×10^{14}	1.6×10^{14}
900	3.2×10^{14}	4.5×10^{14}	5.5×10^{14}

b. Junction Depth / A

Temp./°C \ Time/min	5	10	15
750	18	24	29
800	46	64	80
850	118	166	202
900	270	379	465

c. Average Doping Concentration / cm^{-3}

Temp./°C \ Time/min	5	10	15
750	3.3×10^{19}	3.2×10^{19}	3.2×10^{19}
800	4.2×10^{19}	4.2×10^{19}	4.2×10^{19}
850	8.0×10^{19}	8.0×10^{19}	8.0×10^{19}
900	1.2×10^{20}	1.2×10^{20}	1.2×10^{20}

rich ambient was provided by passing 20 cc/min O_2 together with 450 cc/min nitrogen which acted as a carrier gas.

After diffusion, the diffused back side of the wafer was etched by a silicon etch while the front surface was protected by negative photoresist.

Normal MIS fabrication procedure (see section 3.3.2) was then followed. Completed cells were measured as described in section 3.3.3.

5.3 Results and Discussion

5.3.1 Diffusion temperature and time

Diffusion was carried out for time ranged from 5 min to 15 min at each temperature from 750°C to 900°C at 50°C interval. Lower tempeature was not tried since 750°C already represented the lower bound at which diffusion could occur using the $POCl_3$ liquid source. Degradation has been observed when "diffused" at 700°C [11].

10 min diffusion time has found to yield the best performance at each temperature. For clarity, only results corresponding to a diffusion time of 10 min are shown in Fig. 5.1 to Fig. 5.4 except of efficiencies for which three diffusion times are indicated in Fig. 5.4 (see section 5.3.3 for performance dependence on diffusion time at 800°C).

800°C diffusion has found to be the optimum temperature at which the open circuit voltage (Fig. 5.1), short circuit current (Fig. 5.2), fill factor (Fig. 5.3) and efficiency (Fig. 5.4) reach their maximum values.

The lower performance at 750°C diffusion is attributed to the low surface layer concentration. Also, this layer is so thin (see Table 5.1) that non-uniformity and non-continuity of the layer are not unexpected. These are likely to result in a lower performance.

On the contrary, the lower performance of 900°C diffusion is attributed to the heavier surface doping concentration than optimum [2]. In addition, more serious degradation due to high temperature heat treatment is also expected (see chapter 3).

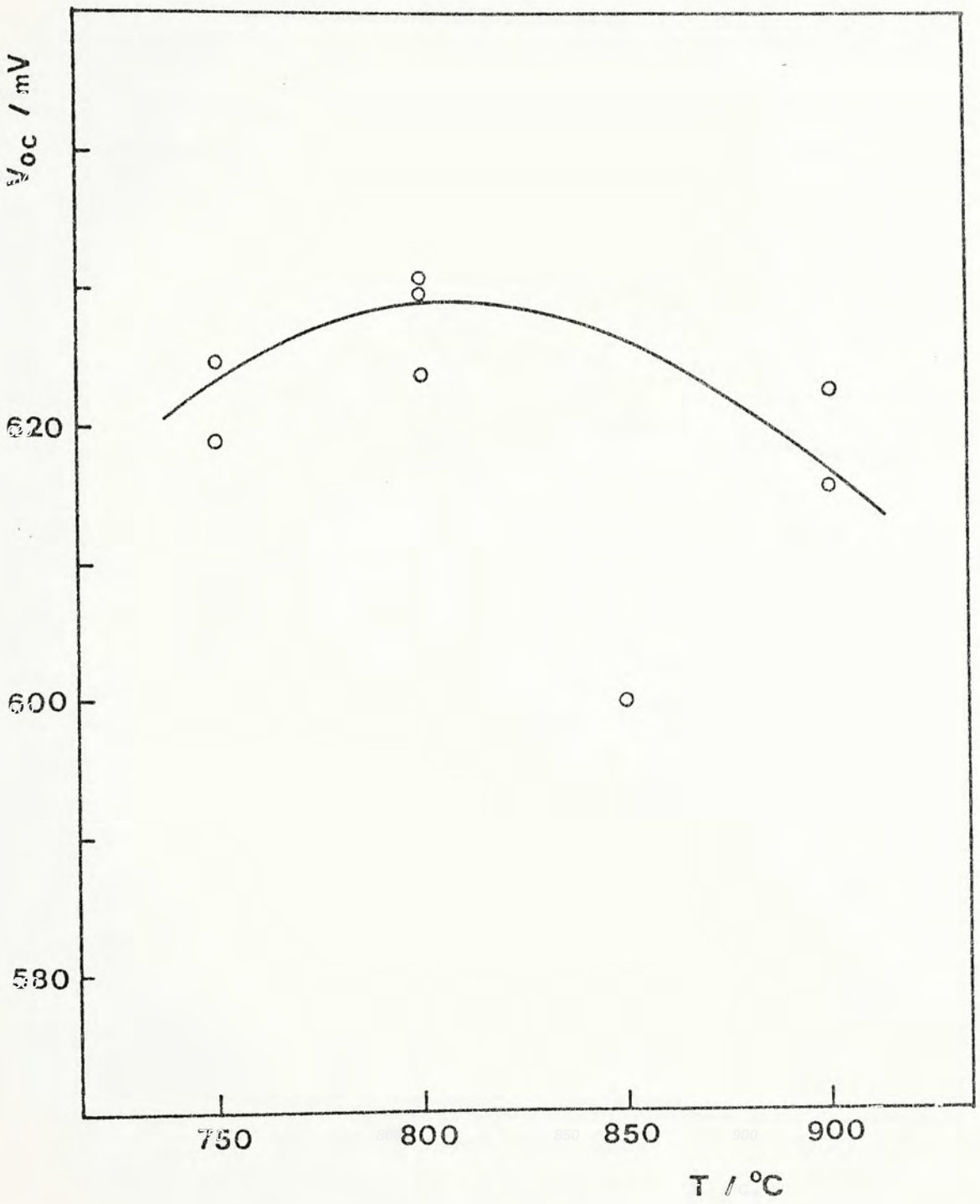

Fig. 5.1 Open circuit voltage versus diffusion temperature. Diffusion time = 10 min. Grid fingers = 76/cm.

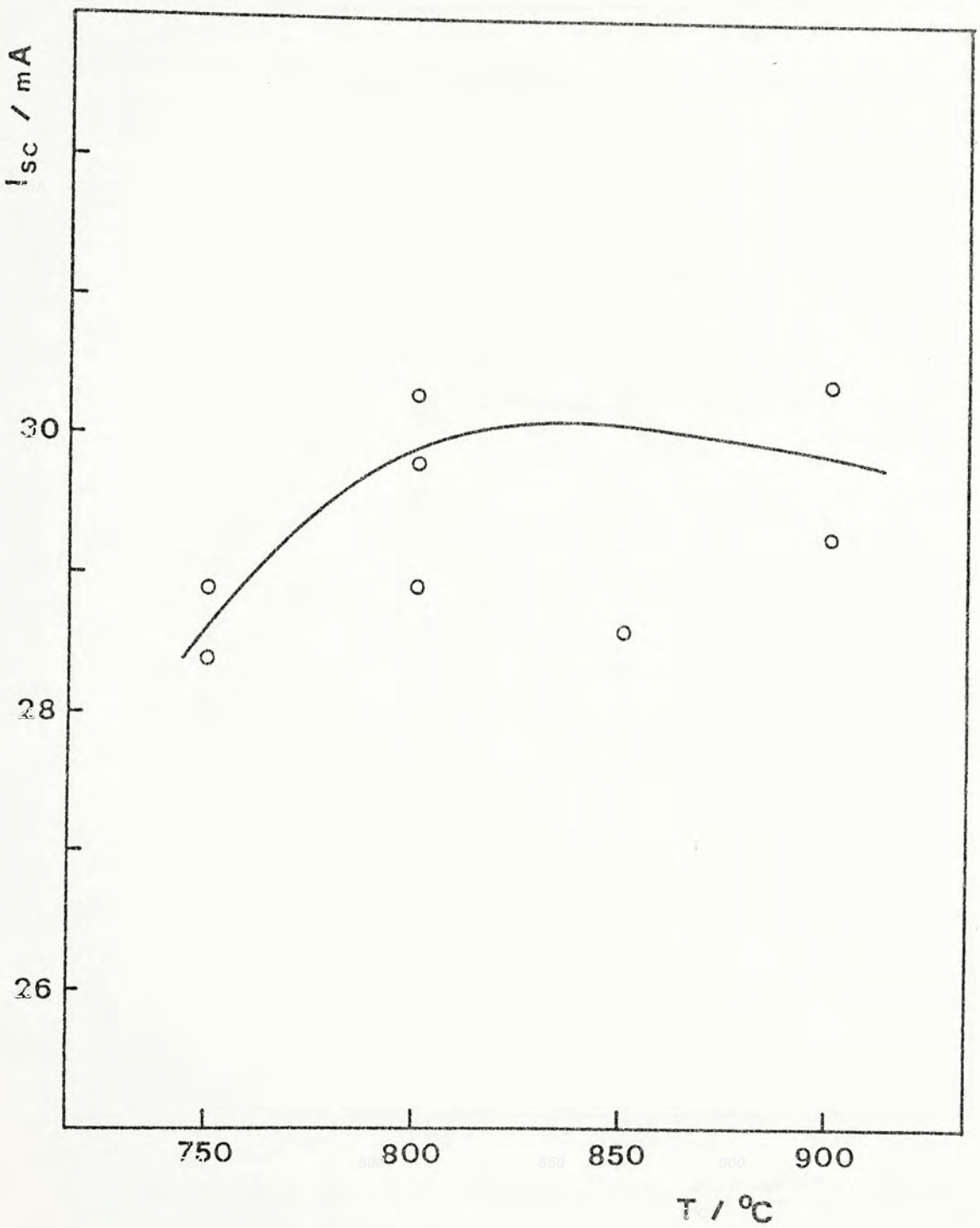

Fig. 5.2 Short circuit current versus diffusion temperature. Diffusion time = 10 min. Grid fingers = 76/cm.

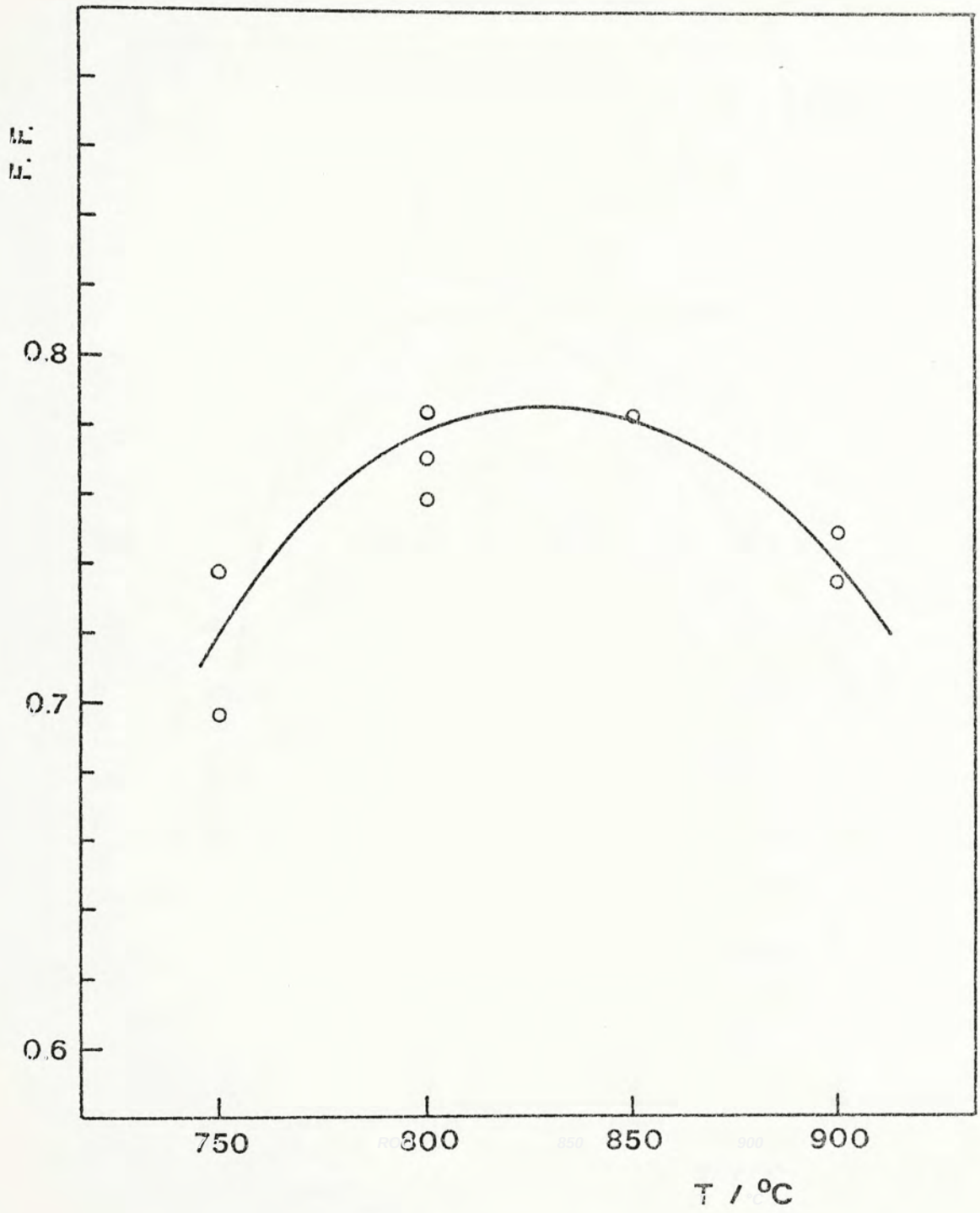

Fig. 5.3 Fill factor versus diffusion temperature.
Diffusion time = 10 min. Grid fingers = 76/cm.

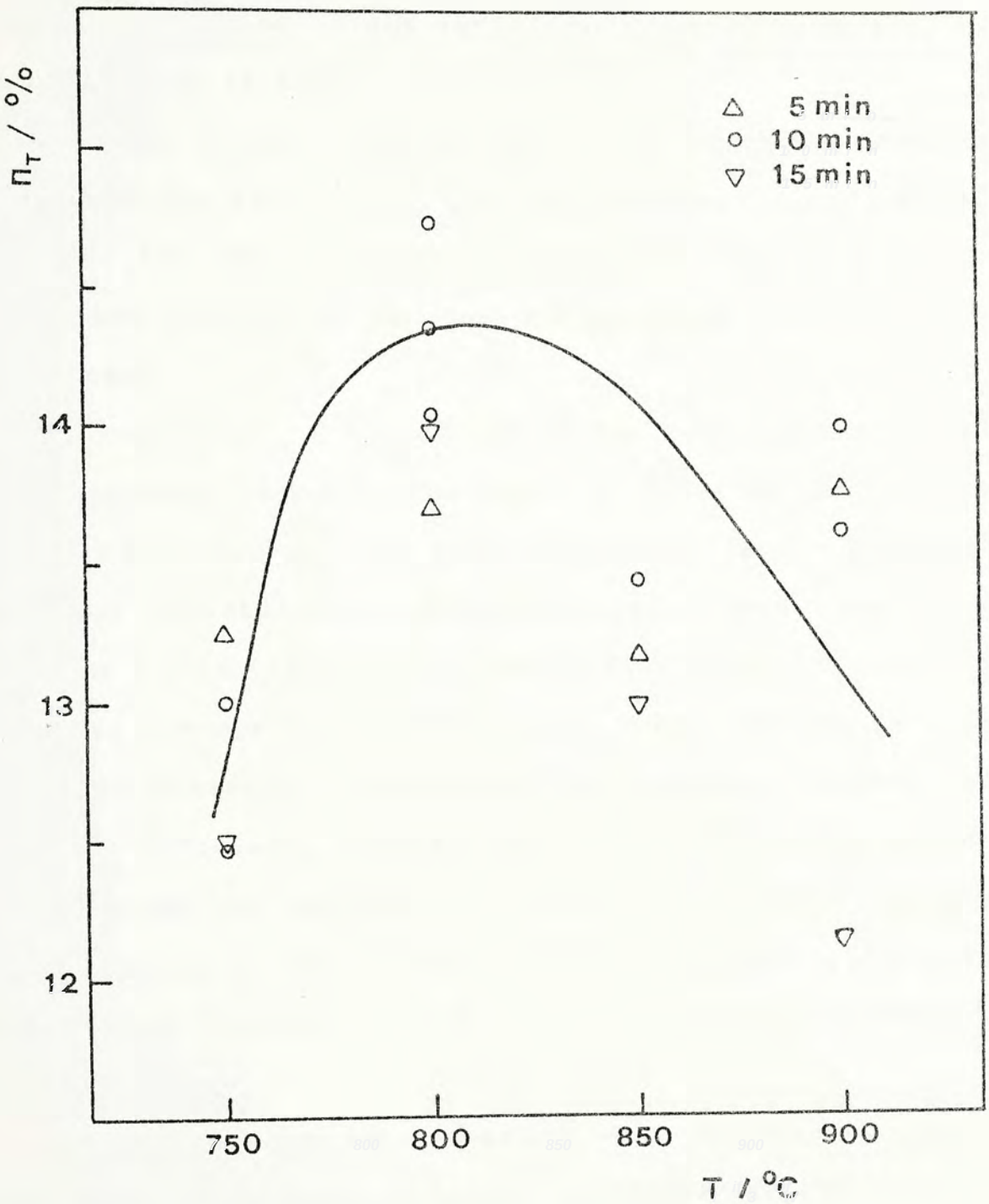

Fig. 5.4 Total area efficiency versus diffusion temperature. Diffusion time = 10 min. Grid fingers = 76/cm.

5.3.2 Grid spacing

The effect of different grid spacings on cell performance was studied. Due to slight variation in metal coverage, active area efficiency is used.

As shown in Fig. 5.5, the efficiency of the MINP cells are higher than the MIS cells. The margin of efficiency advantage increases with the grid spacing. Over 2 % efficiency difference between the MINP cells and the MIS cells is observed at large grid spacing.

The rapid drop in efficiency as the grid spacing of the MIS cells increases is due to the rapid fall off of the fill factor as shown in Fig. 5.6. The decrease in fill factor is due to the high sheet resistivity of the inversion layer. As one moves away from a grid finger, the local bias voltage increases until it reaches the open circuit voltage. That results in a finite collection distance. Visschere [12], however, showed that the collection efficiency started falling correspondingly before this critical value was reached. He explained that there was a second critical value at which the collection of minority carriers changed from vertical (one dimensional) to lateral (two dimensional).

Our results are in agreement with Visschere. The fill factor of the MINP cells is better maintained as the grid spacing increases due to a lower sheet resistivity of the surface doped layer.

Although the series resistance is reduced by the surface doping, the grid spacing should only be increased to an extent that the carrier collection is still vertical to assure a high

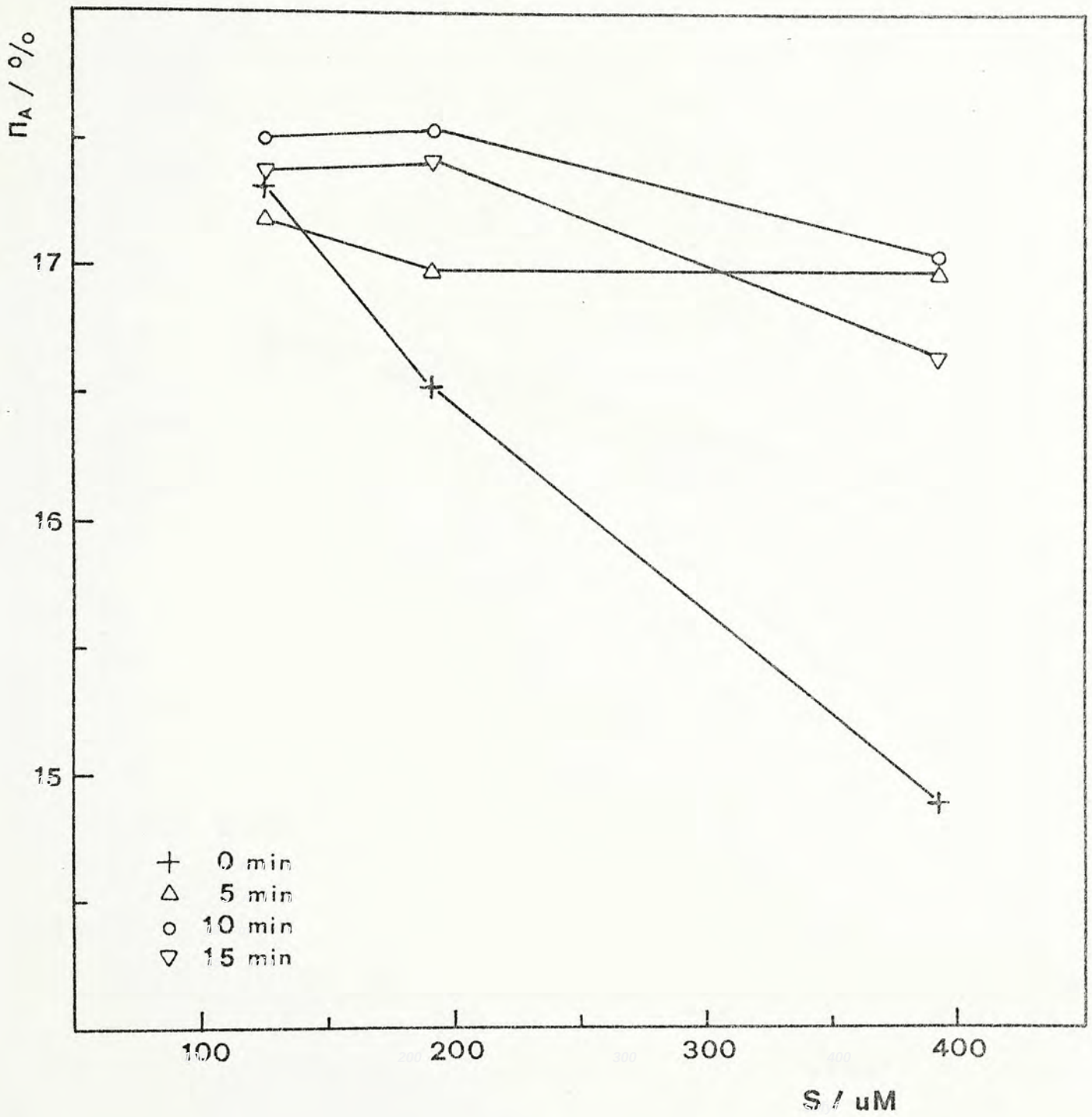

Fig. 5.5 Active area efficiency versus grid spacing.
Various diffusion time at 800 °C.

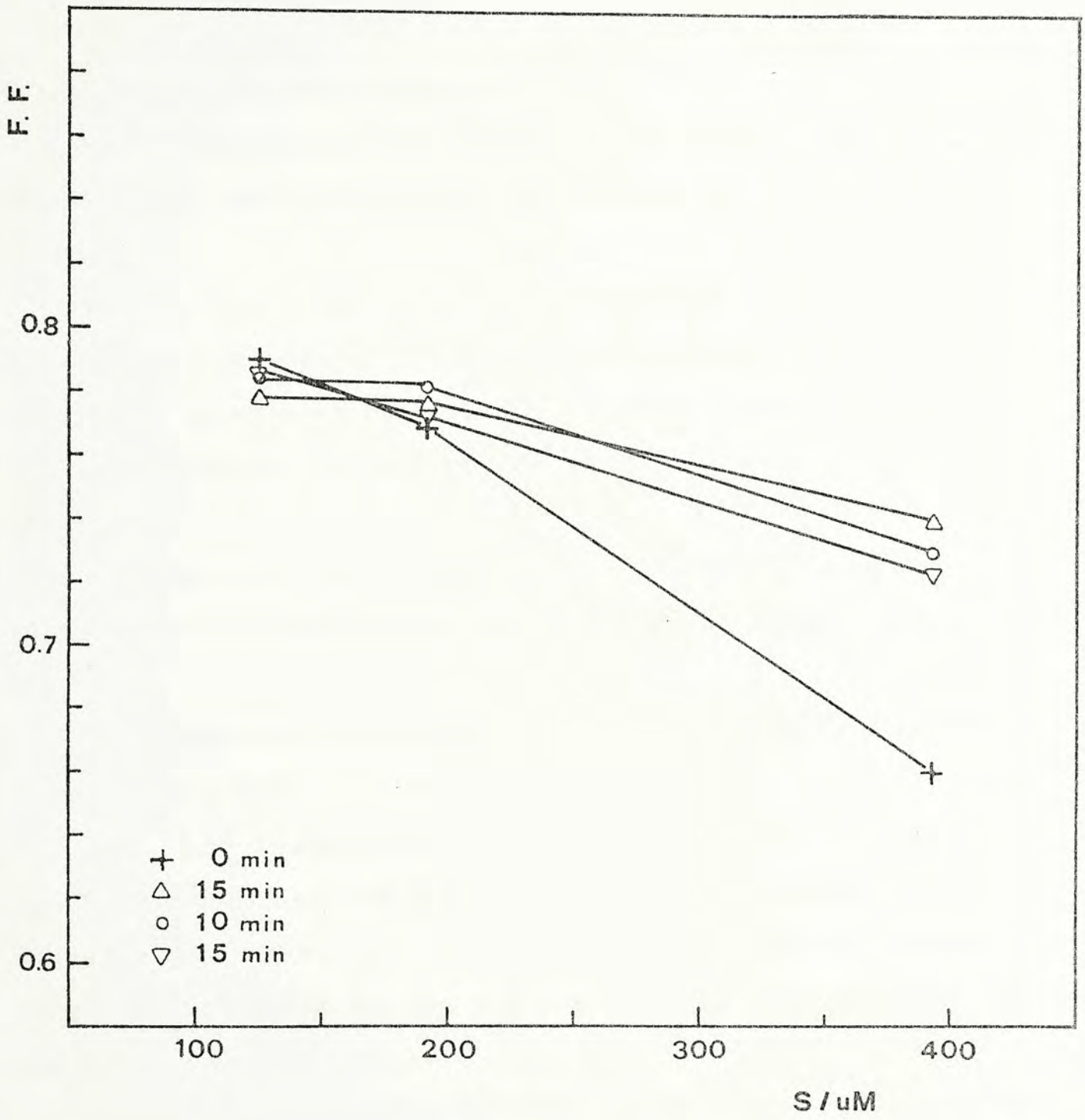

Fig. 5.6 Fill factor versus grid spacing.
Various diffusion time at 800 °C.

fill factor.

5.3.3 Substrate resistivity

FZ 0.5 ohm-cm and CZ 1.5 ohm-cm base resistivity cells are fabricated at 800°C diffusion. The results are shown in Fig. 5.7 - Fig. 5.13.

In Fig. 5.7, the higher open circuit voltage of the 0.5 ohm-cm cells are due to the lower base resistivity which results in a lower saturation current. There is a slight enhancement in the open circuit voltage of the MINP structure over the MIS structure.

The current advantage of the MINP structure is more significant in both the 0.5 and 1.5 ohm-cm cells as shown in Fig. 5.8.

No significant difference is observed in the fill factor as shown in Fig. 5.9.

Fig. 5.10 indicates that a high efficiency is obtained in the MINP structure and the 0.5 ohm-cm cells produce a larger increase than the 1.5 ohm-cm cells. The optimum diffusion condition is 10 min for the 0.5 ohm-cm substrate and 5 min for the 1.5 ohm-cm substrate.

Fig. 5.11 shows the carrier lifetime dependence. The carrier lifetime of cells fabricated from both resistivities decrease as the diffusion time increases. The higher lifetime in the lower resistivity cell is due to the different crystal preparation method used for the wafer of this cell (FZ). FZ

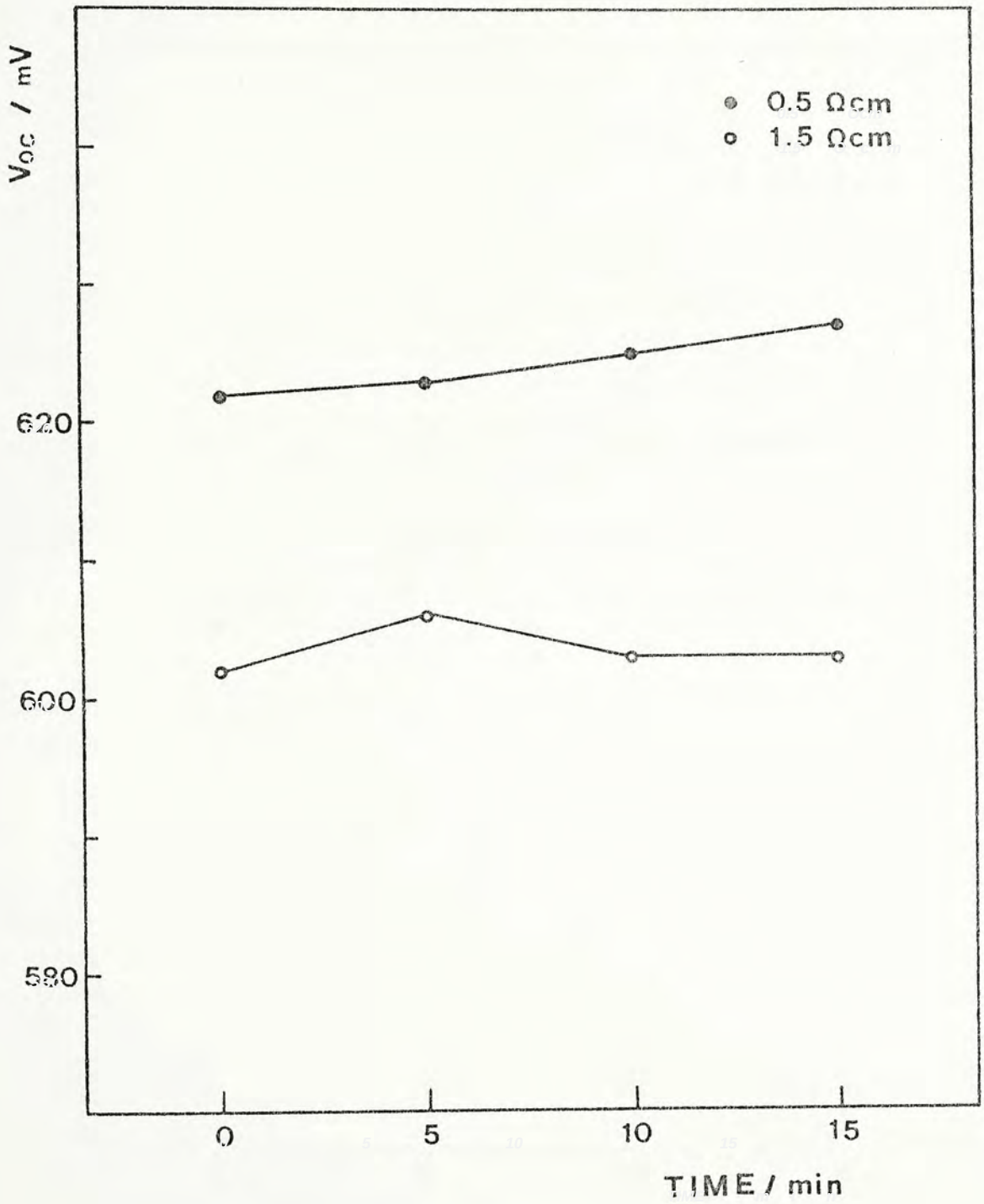

Fig. 5.7 Open circuit voltage versus diffusion time for different substrate resistivities. Diffusion temperature = 800 °C.

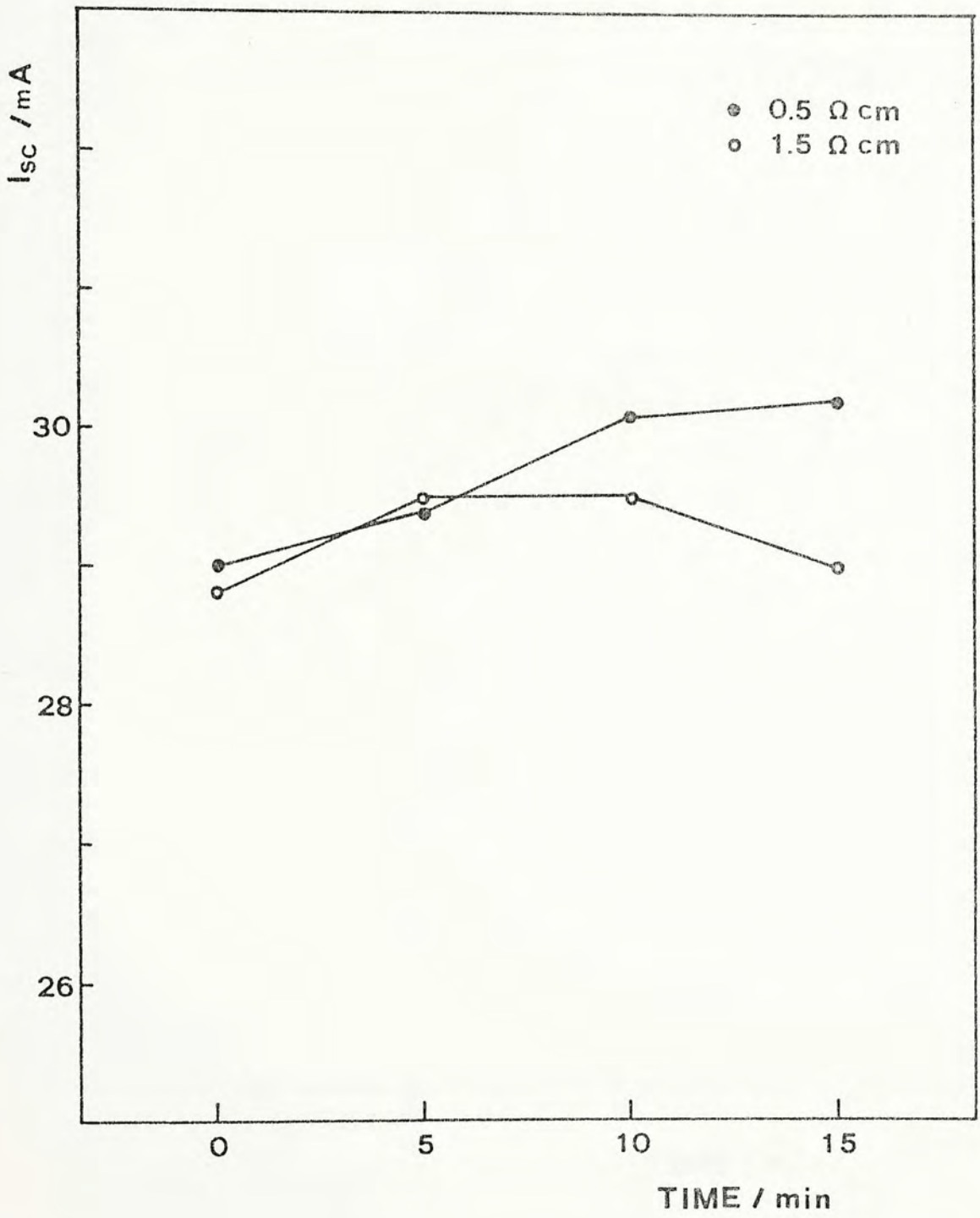

Fig. 5.8 Short circuit current versus diffusion time for different substrate resisitivities. Diffusion temperature = 800 °C.

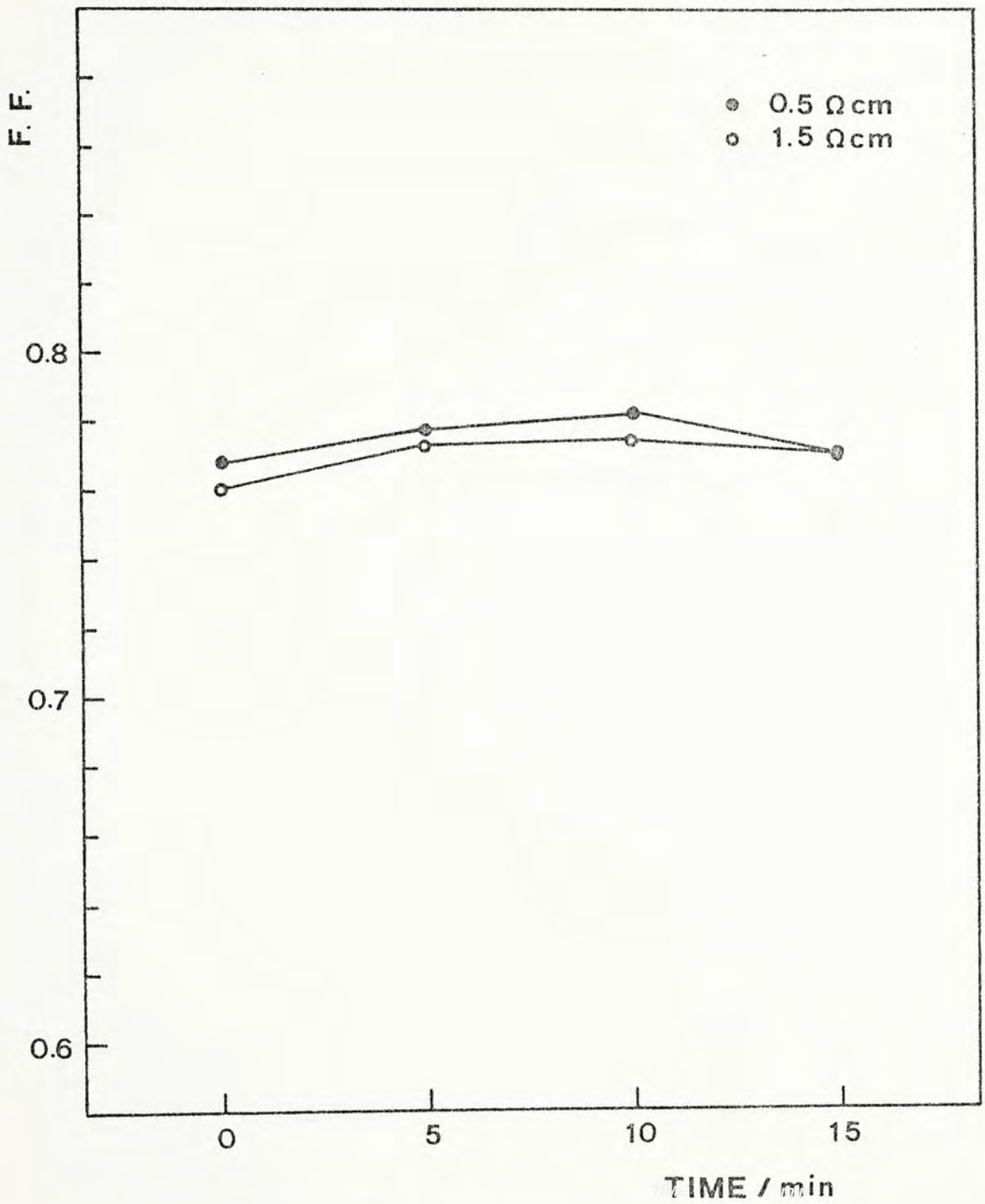

Fig. 5.9 Fill factor versus diffusion time for different substrate resisitivities.
Diffusion temperature = 800 °C.

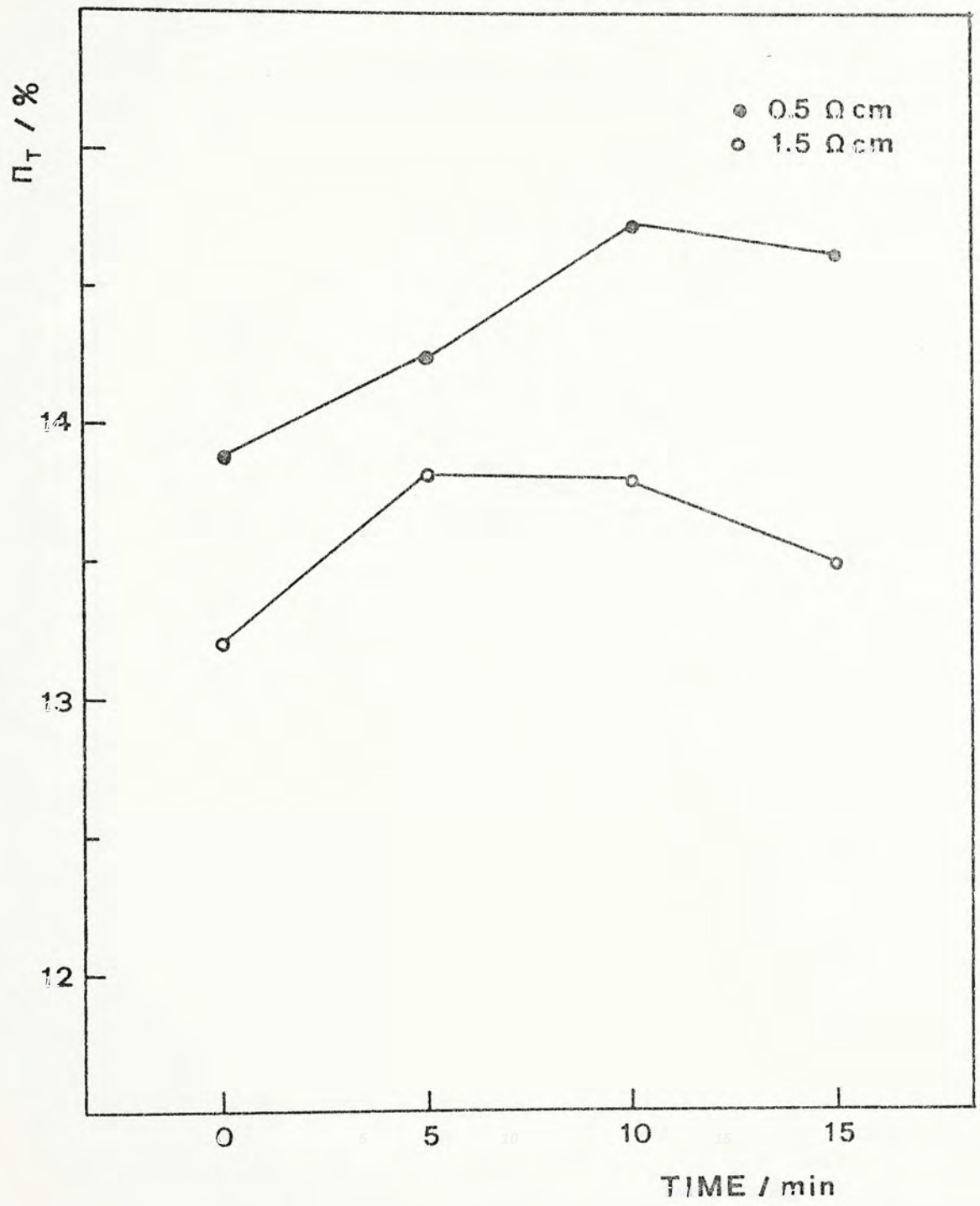

Fig. 5.10 Total area efficiency versus diffusion time for different substrate resisitivities. Diffusion temperature = 800 °C.

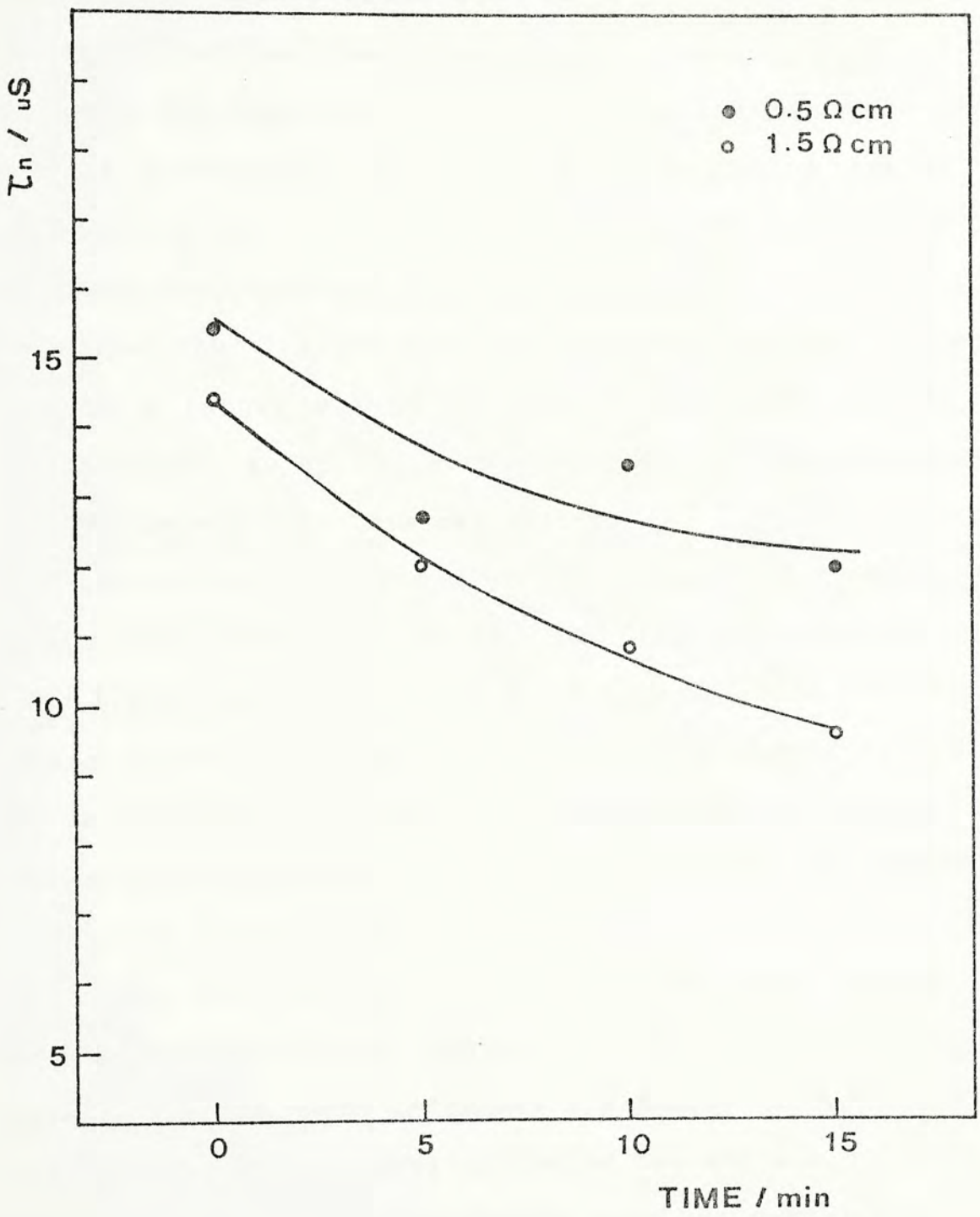

Fig. 5.11 Minority carrier lifetime versus diffusion time for different substrate resisitivities. Diffusion temperature = 800 °C.

crystals are known to have better lifetime than CZ crystals.

The magnitude of decrease in lifetime in the diffused MINP cells is approximately equal to that of the heat treated MIS cells. This implies that the lifetime degradation is not dominated by the doping level, but rather by the temperature of the heat treatment. The probable degradation due to the diffused dopants may be counter-balanced by the gettering effect of phosphorus that improves the lifetime.

Note also that the lifetime of the ion implanted MINP cells degrades to a larger extent due to unactivated dopants and residual damage. We conclude that diffusion process is better than ion implantation in this respect.

The saturation current and the ideality factor increase as the diffusion time in both the 0.5 and 1.5 ohm-cm cells (Fig. 5.12 and Fig. 5.13) but the 1.5 ohm-cm cells have higher saturation current and ideality factor. The higher saturation current is due to its higher resistivity while the larger ratio of n^+ layer concentration to the base concentration predicts a higher ideality factor as in Fig. 2.5.

Both the diffused and ion implanted MINP cells show increases in the saturation current and the ideality factor with dose level. However, such increases are smaller in the former.

The increase in the ideality factor for the 0.5 ohm-cm cells is considered to be in good agreement with the calculation shown in Fig. 2.5 with profile parameters taken from Table 5.1, within the error of the uncertainty in diffusion constants.

The excess current component as analyzed in chapter 4 by subtracting the diffusion current calculated from V_{oc}/J_{sc}

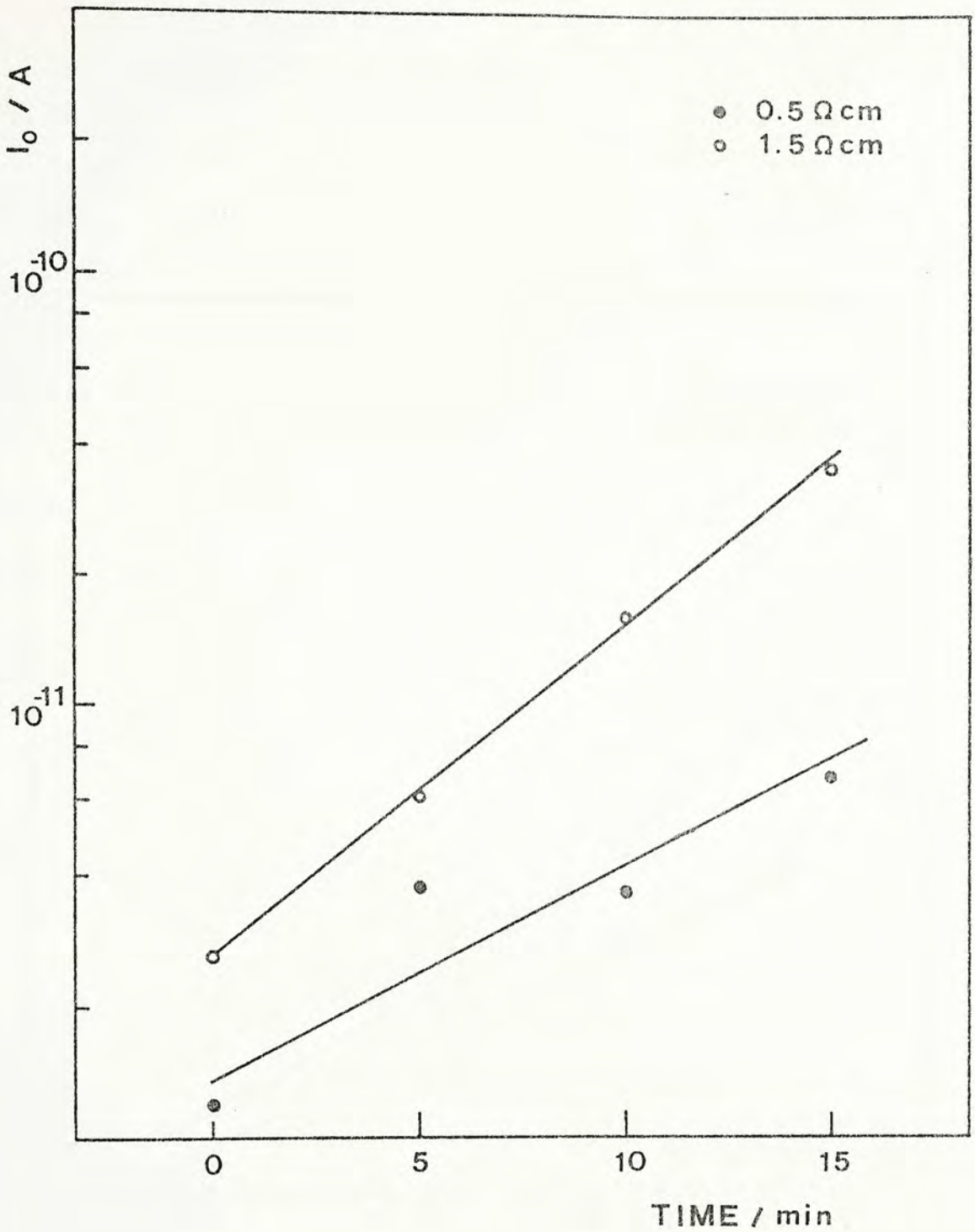

Fig. 5.12 Saturation current versus diffusion time for different substrate resistivities. Diffusion temperature = 800 °C.

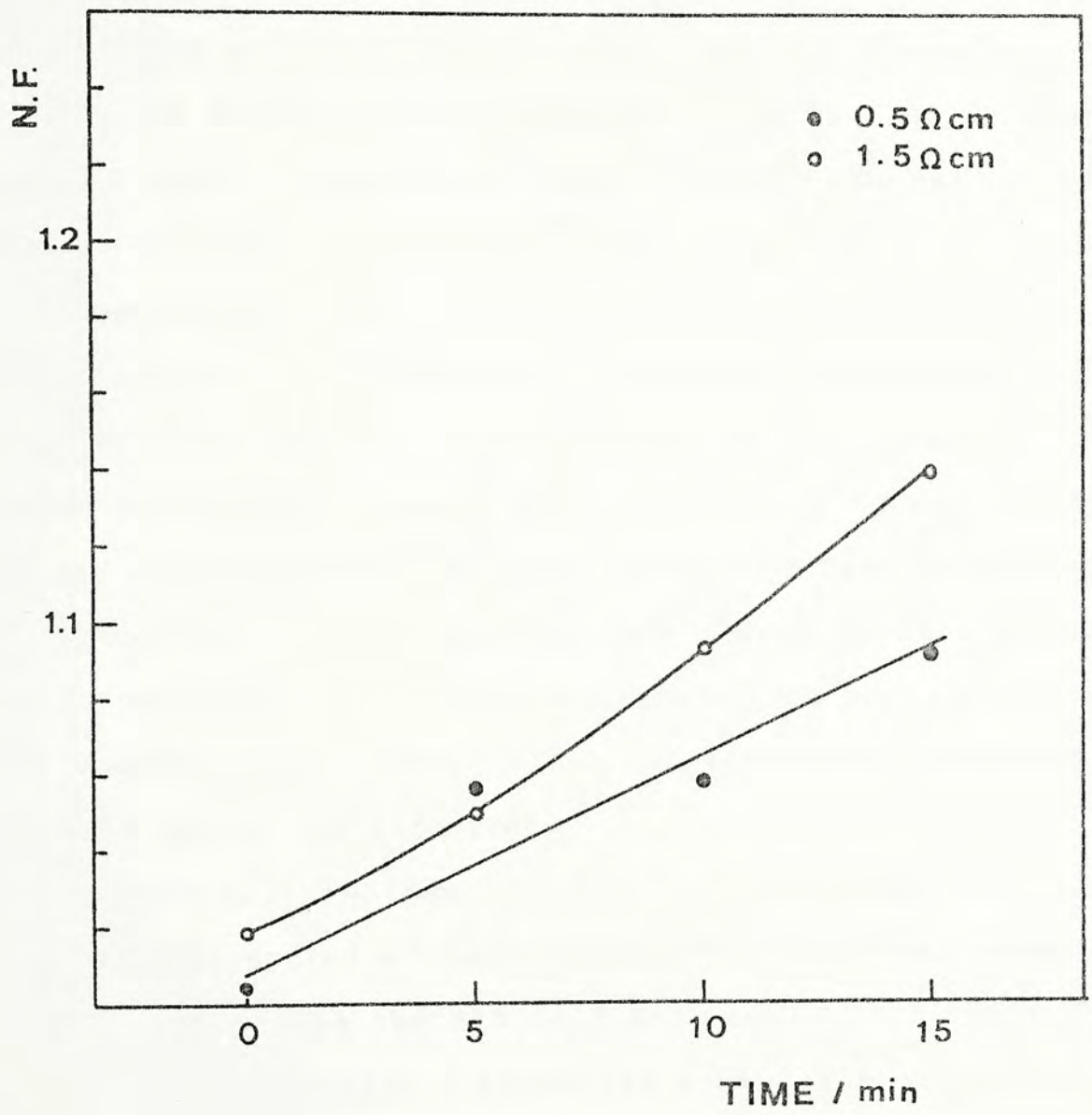

Fig. 5.13 Ideality factor versus diffusion time for different substrate resistivities.
Diffusion temperature = 800 °C.

measurement from the total current is also performed. The excess current and the corresponding ideality factor are $1.5\text{-}5\times10^{-7}$ cm^{-2} and 2.1-2.4 respectively. The value of the ideality factor suggests that the recombination current in the depletion region is dominating rather than the field emission current as suggested by Anderson et al. [13]. The magnitude of the excess current in the diffused MINP cells is roughly equal to that of the ion implanted cell at low dose. Such a magnitude can be easily explained by a τ_{no} about 4×10^{-9} sec in the depletion region as calculated in chapter 4.

A plot of V_{oc}/J_{sc} is shown in Fig. 5.14 indicating that the excess current due to recombination is much larger in the diffused MINP cells than the MIS cells. This is not unexpected since the crystal perfection in an undoped surface is much better than a doped surface. Note that such excess current component which is reflected in the ideality factor near the maximum power point, softens the current voltage characteristic resulting in a lower fill factor and efficiency.

The spectral response of the 0.5 ohm-cm cells are shown in Fig. 5.15. The optimized cell shows better spectral response in all wavelengths than the MIS cell and other MINP cells except for D (15 min diffusion) which has a higher short wavelength response. This is also shown up in a higher short circuit current. However, its efficiency is lower due to a lower open circuit voltage and fill factor.

Also shown in Fig. 5. 15 is the spectral response of a commercial p-n junction cell which is substantially poorer than

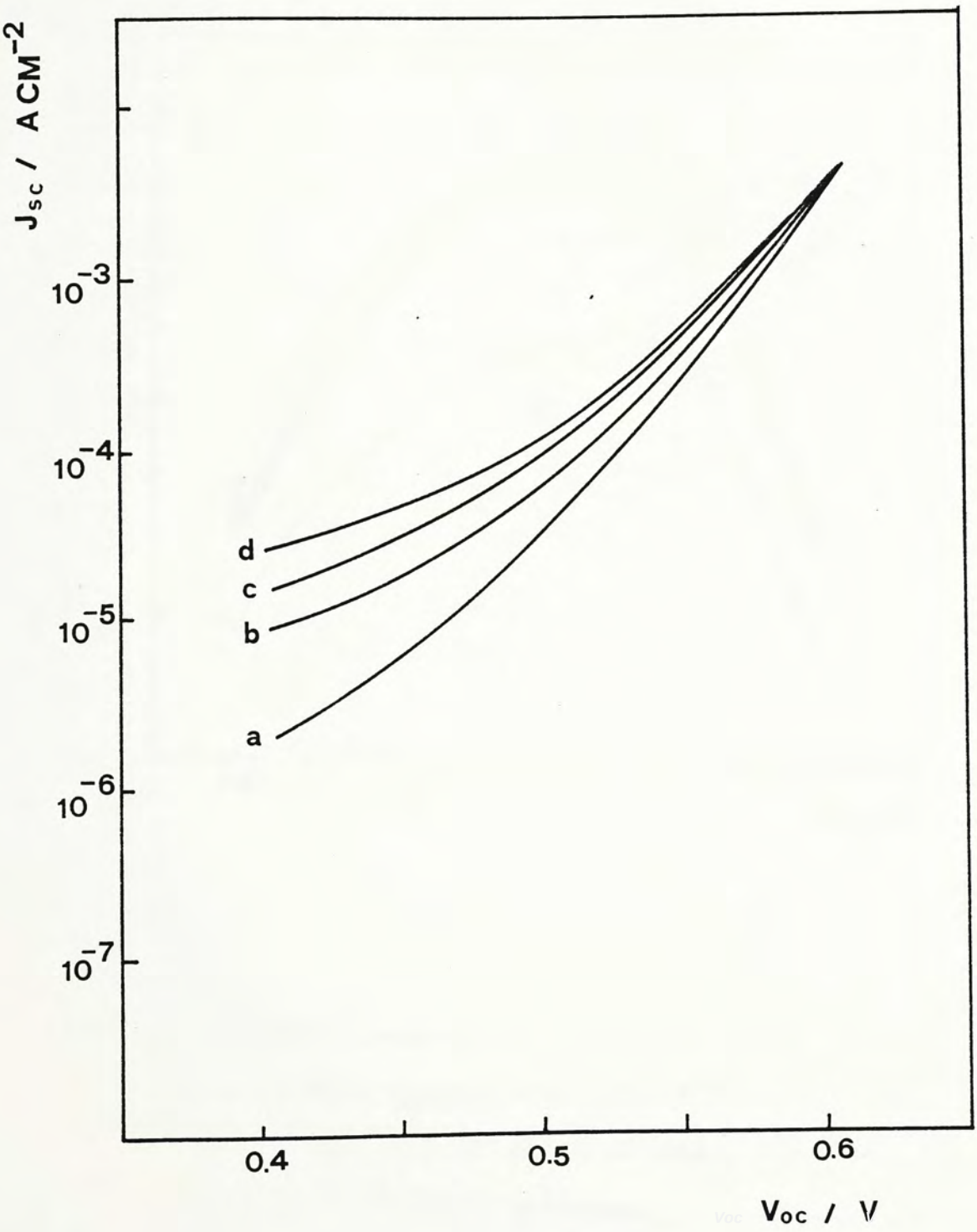

Fig. 5.14 V_{oc} versus J_{sc}. ρ = 1.5 ohm-cm. Diffusion temperature = 800°C.
a : MIS, b, c, d : MINP - 5, 10, 15 min diffusion.

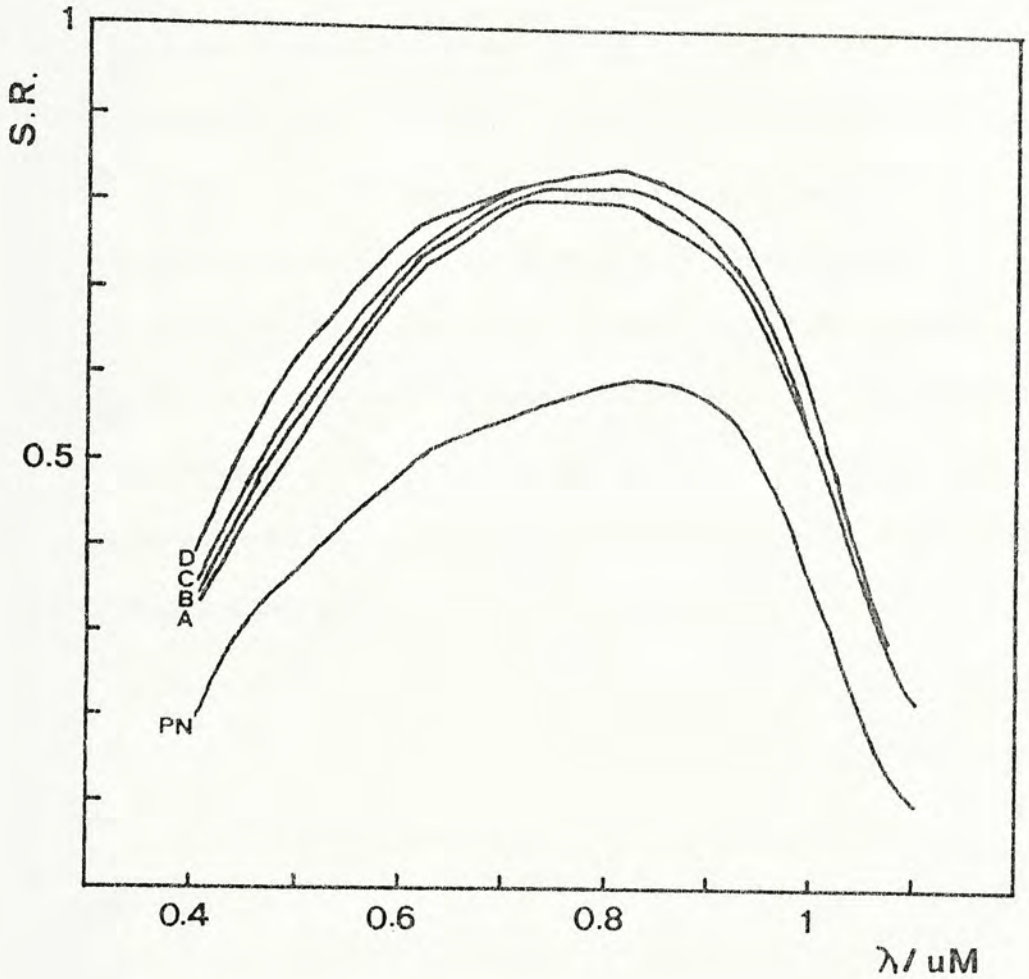

Fig. 5.15 Spectral responses (arbitrary unit) for various diffusion conditions. A - MIS , B - MINP 800 °C 5 min , C - MINP 800 °C 10 min , D - MINP 800 °C 15 min , PN - PN junction.

our cells.

The performance parameters of the best MINP cell fabricated on 0.5 ohm-cm substrate mesured under AM1.5 illumination are V_{oc} = 641 mV, I_{sc} = 31.5 mA, FF = 0.7863, n_T = 15.88 % and n_a = 17.9 % (metal coverage of 11.5 %).

Our cells compare favorably to cells fabricated with comparable technique (single layer antireflection coating MINP structure) which recorded efficiency of 16 % (AM1.5) on 0.1 ohm-cm substrate with back surface field [2].

Cells with higher efficiency have been reported as described in section 5.1. However, these cells were fabricated on a lower resistivity substrate (0.1 ohm-cm) with back surface field, surface passivation, thick metallization and double layer antireflection coating.

5.4 Conclusions

Diffused MINP cells are studied in detail. The optimum diffusion conditions are found to be 800°C for 10 min with the $POCl_3$ liquid source. This is a compromise between the optimum surface doping concentration and the heat treatment temperature.

Studies on the performance dependence on the grid spacing are made. The MINP structure is found to minimize the degradation in performance as the grid spacing widens found in the MIS structure. The reduced series resistance at the surface due to a surface doped layer maintains the vertical collection of photo-generated carriers resulting in a higher fill factor even when the grid spacing is widened.

Two different resistivity substrates are studied. Higher efficiency advantage is obtained in the MINP structure compared to the MIS structure in 0.5 ohm-cm substrate than 1.5 ohm-cm substrate. Detailed performance parameters are reported. The lifetime degradation in the diffused MINP cells is approximately equal to that of the heat treated MIS cells and is much less than that of the ion implanted MINP cells. This implies the lifetime degradation in the diffused MINP cells is determined by the temperature of the heat treatment but not by the doping level as in the ion implanted MINP cells. This is probably due to two counter-balanced effects between the lattice imperfection due to the diffused dopants (degradation) and the gettering effect of phosphorus (enhancement).

Both the saturation current and the ideality factor ofthe diffused MINP cells are found to be increased with dose level but

to a lesser extent than the ion implanted MINP cells. The increase in the ideality factor is considered to be in good agreement with the calculation shown in Fig. 2.5. The excess current component is shown to be dominated by recombination in the depletion region with a reasonable lifetime about 4×10^{-9} sec, but not by the field emission current. This is consistent with the finding in chapter 4 that the excess current due to field emission occurs only in high dose level. The excess current component observed in the ion implanted and diffused cells is higher than the MIS cells. The current voltage characteristic is softened by this current which is reflected by the ideality factor near the maximum power point resulting in a lower fill factor and decreased efficiency (potentially even higher).

The optimized cell possesses superior response in all wavelengths over the MIS cells and other MINP cells except one in short wavelength where its efficiency is, however, lowered by lower open circuit voltage and fill factor.

A high open circuit voltage and high efficiency solar cell has been fabricated which recorded V_{oc} = 641 mV, I_{sc} = 31.5 mA, FF = 0.7863 and n_T = 15.88 % at AM1.5 illumination. The cell out performs the best ion implanted MINP cell leading to a conclusion that diffusion is better than ion implantation in fabrication of the MINP cells.

References

[1] H.C. Card, E.S. Yang and P. Panayotatos, "Peaked Schottky barrier solar cells by Al-Si metallurgical reactions," Appl. Phys. Lett., Vol. 30, p.643, 1977.

[2] M.A. Green et al., "The MINP solar cell - a new high voltage, high efficiency silicon solar cell," 15th IEEE Photov. Spec. Conf., p.1405, 1981.

[3] A.W. Blakers and M.A. Green, "678 mV open circuit voltage silicon solar cells, " Appl. Phys. Lett., vol. 39, p.483, 1981.

[4] M.A. Green et al., "Towards a 700 mV silicon solar cell," 16th IEEE Photov. spec. Conf., p.1219, 1982.

[5] A.W. Blakers et al., "18 percent efficient terrestrial silicon solar cells," IEEE Ele. Dev. Lett., Vol. 5, p.12, 1984.

[6] M.A. Green et al., "High efficiency silicon solar cells," IEEE Trans. Ele. Dev., Vol. 31, p.679, 1984.

[7] M.A. Green et al., "19.1 % efficient solar cell," Appl. Phys. Lett., Vol. 44, p.1163, 1984.

[8] M.A. Green and A.W. Blakers, "Relationship between the blue response and open circuit voltage of high performance silicon solar cells," IEEE Trans. Ele. Dev., Vol. 30, p.1360, 1983.

[9] A.S. Grove, Physics and Technology of Semiconductor Devices, Wiley, 1967.

[10] S.M. Sze, VLSI Technology, McGraw Hill, 1983.

[11] C.S. Hoi, "Studies of the electrical characteristics of

MIS/MINP solar cells," M. Phil. thesis, CUHK, 1983.

[12] P.V. Visschere, "Two dimensional modeling of the MIS grating solar cell," IEEE Trans. Ele. Dev., Vol. 30, p.840, 1983.

6. CONCLUSIONS

MINP grating solar cells are studied in detail.

We have analysed in chapter 2 that in the metal-insulator-n-p region, depending on the free carrier concentration in the n^+ and p layers, four cases can be considered separately -

1. the surface n^+ and p layers are depleted,
2. the surface n^+ layer is depleted only,
3. the free carrier concentration is significant in both layers such that no approximation should be made, and
4. the surface n^+ layer is thick enough such that a neutral n region is formed. It can then be treated as a MIS barrier in cascade with a p-n junction.

Expressions for the barrier height enchancement and the ideality factorhave been derived except for case 3 since full analytical expressions are not feasible.

On a p type substrate, a high work function metal will deplete both layers such that case 1 applies. But in this study, a low work function metal is used such that the free carrier concentration is important in the p layer (case 2) or even in both layers (case 3). Case 4 corresponds to a heavily doped MINP structure.

We have calculated the barrier height enhancement and the ideality factor against the surface layer doping concentration with different surface layer thickness for the metal work function and the substrate resistivity used in the experimental study. There is a critical doping concentration such that barrier height enhancement exists only when this critical value

is exceeded. For any barrier height enhancement a thinner surface layer requires a higher doping concentration. The ideality factor, however, also increases first slowly and then sharply with the surface doping concentration.

The hole current density can be reduced to a low value by increasing the surface doping dosage. The total saturation current will finally be limited by the electron diffusion current in the bulk.

In the antireflection coating-insulator-n-p region, two major loss mechanisms - surface recombination loss and series resistance loss are considered. By minimizing the surface recombination current taking into account of the bandgap narrowing effect, optimum surface doping concentration is found for both nondegenerate and degenerate cases. Doping concentrations of 5.3×10^{18} cm^{-3} and 7.8×10^{19} cm^{-3} are required for the nondegenerate case and degenerate case respectively. These values are substantially lower than heavily doped emitter in conventional p-n junctions.

The sheet resistivity is lowered as a result of the surface doped layer which suggests that a wider grid spacing can be used to lower the shadow loss.

Process temperature is known to play an important role in high efficiency solar cells. But a high temperature step (either in the diffusion of the n layer or in the annealing of ion implanted cells) is unavoidable. The performance of the MINP cells thus depends on both the surface doping effect and the

temperature treatment effect. Also, previous studies on temperature effect employed p-n junction cells such that the temperature effect has not been isolated from the doping effect. We have performed isochronal and isothermal pre-processing heat treatment on MIS solar cells to study the peformance dependence solely due to the temperature effect for the first time.

We have found that the cell peformance degrades as the heat treatment temperature increases. The saturation current and the ideality factor also increase with heat treatment temperature. The performance degradation is partly explained by the carrier lifetime degradation. However, the saturation current calculated by using the degraded lifetime is substantially lower than the measured value. This suggests that the increases are not only due to the bulk lifetime degradation but also due to other effects such as recombination in the space charge region and surface states. Furthermore, such effects are temperature dependent. The short and long wavelength degradation in the spectral response measurement supports the above intepretation.

To achieve high efficiency, a lower temperature and shorter time should be used to obtain the desired doping concentration and annealing.

Experimental studies of the MINP structure by both ion implantaion and diffusion are conducted systematically. The performance dependence of the MINP cells on parameters such as implant dose, energy, annealing condition, diffusion temperature and time has not been reported in the literature. Cells are fabricated by a simple, align[illegible] free process with single layer

SiO antireflection coating but without back surface field.

In the case of ion implanted MINP cells, implant parameters (dose and energy) and annealing conditions have been investigated systematically. The implant dose ranges from 10^{12} cm^{-2} to 10^{15} cm^{-2} while ion energy of 20 KeV and 30KeV are used. Annealing temperature ranges from 600°C to 900°C. Four sets of implant and anneal conditions have been studied -

set A 20 KeV implant, single step anneal

set B 20 KeV implant, three step anneal

set C 30 KeV implant, three step anneal

set D 30 Kev through oxide implant, three step anneal

The performance dependence of the four sets isqualitaively the same. Low temperature annealing of the ion implanted layer results in insufficient anneal with unfully activated dopantsand residual damage. High temperature annealing, however, lowers the bulk lifetime without further activation of dopants and removal of residual damage. The optimum annealing temperature has been found to be 800°C.

Among the four sets of implant and anneal conditions, set C - 30 KeV implant, three step anneal yields the best result. 30 KeV implants (set C and set D) are superior to 20 KeV implants (set A and set B). There is no significant difference in performance for 20 KeV implants under single step or three step annealing.

The optimum dose is about 10^{13} cm^{-2} which is two orders of magnitude lower than that in conventional ion implanted p-n junction cells. This implies ion implantation using the MINP

structure may be cost competitive to diffusion.

The best ion implanted cell measured is fabricated under 30 KeV Phosphor us implant at dose level of 10^{13} cm^{-2} under three step annealing at 550°C 2 hours, 800°C 15 min, 550°C 2 hours. The performance parameters are V_{oc} = 624 mV, I_{sc} = 30.4 mA, FF = 0.791, and n_T = 15 % at AM1.5.

The peformance of the ion implanted MINP cells is substantially higher than the MIS cells due to the superior short circuit current. There is only marginal open circuit voltage advantage. The explanation to the performance dependence is also supported by the spectral response measured.

The decrease in the carrier lifetime and increase in the saturation current and the ideality factor of the ion implanted MINP cells are substantially larger than that of the heat treated MIS cells. We thus conclude that the dependence is dominated by the doping level even though there is still some temperature dependence.

The increase in ideality factor is in qualitative agreement with the calculation in chapter 2 assuming only the n^+ layer is depleted. Detailed analysis of the excess current shows that a recombination current through traps in the depletion region dominates at low dose level. While at high dose level, our result is consistent with Anderson et al. who have suggested that a field emission current dominates.

In the case of diffused MINP cells, the two independent parameters - temperature and time are studied in detail.

800°C 10 min single step diffusion has been found to be the

optimum diffusion condition as a compromise between the optimum surface doping concentration and the heat treatment temperature.

The effects of different grid spacings on the cell performance for the MINP cells are demonstrated for the first time. The efficiency of the MINP cells are higher than the MIS cells. The margin of the efficiency advantage increases with the grid spacing. The rapid drop in efficiency with the grid spacing of the MIS cells is due to the rapid fall off of the fill factor as a result of high sheet resistivity in the inversion layer. The fill factor of the MINP cells are better maintained due to a reduced sheet resistivity in the surface layer assuring the vertical collection of photo-generated carriers.

Cell performance of two substrate resistivities are studied. The cell performance indicates high efficiency is obtained by MINP structure while the 0.5 ohm-cm cells produce a larger increase than the 1.5 ohm-cm cells.

Performance parameters are reported. The lifetime degradation in the diffused MINP cells is approximately equal to that of the heat treated MIS cells but is much less than that of the ion implanted MINP cells. The lifetime degradation in the diffused MINP cells is thus determined by the temperature treatment rather than the doping concentration (as in the ion implanted MINP cells). This is probably due to two counter-balanced effects between lattice imperfection due to the diffused dopants (degradation) and the gettering effect of phosphorus (enhancement).

The saturation current and the ideality factor of the

diffused MINP cells increase with dose level but to a smaller extent than the ion implanted MINP cells. The increase in the ideality factor is in good agreement with the theoretical calculation.

The excess current component is shown to be dominated by recombination in the depletion region as in low dose ion implanted MINP cells.

The excess current in the diffused MINP cells is higher than that of the MIS cells. The current voltage charactersitic is softened by this excess current component which is reflected by the higher ideality factor near the maximum power point resulting in a lower fill factor and decreased (potentially higher) efficiency.

The performance of the best diffused MINP cell measured on 0.5 cm under AM1.5 illumination are V_{oc} = 641 mV, I_{sc} = 31.5 mA, FF = 0.7863, n_T = 15.88 %, and n_a = 17.9 % which is higher than the best ion implanted MINP cell. We conclude that diffusion is better than ion implantation in fabrication of MINP cells. Our cell compares favourably to the best cell reported made by comparable technique on a lower resistivity substrate.

We have reported studies of the MINP grating cells. To achieve even higher efficiency, methods such as incorporating a back surface field and improving surface passivation can be employed.

Surface passivation is in consistent with the present alignment free process. After the surface passivating oxide is

thermally grown, parallel strips are etched for metal contact. The grid fingers should then be evaporated through the silicon shadow mask in the direction perpendicular to the contact strips resulting in dot contacts. This, in fact, also reduces the metal contact area.

The field emission current component suggested by Anderson et al. is not intrinsic to the MINP cells but applies also to the MNP cells. We have shown in this study that the excess current is dominated by the recombination current in the depletion region at low dose. However, more rigorous proof can be obtained from the temperature dependence by performing current voltage measurement at various temperatures.

Investigation in other areas such as reliability and transient annealing in ion implanted cells should be of general interest.